

EXPERIMENT VS NATURE: USING AMPHIBOLES TO TEST
MODELS OF MAGMA STORAGE AND PRE-ERUPTIVE MAGMA
DYNAMICS PRECEDING THE 2006 ERUPTION OF AUGUSTINE
VOLCANO, ALASKA

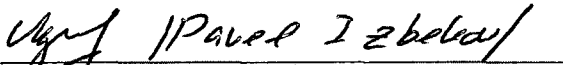
By

Sarah Massey Henton

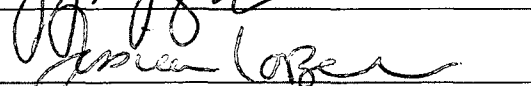
RECOMMENDED:











Advisory Committee Chair



Chair, Department of Geology and Geophysics

APPROVED:



Dean, College of Natural Science and Mathematics



Dean of the Graduate School



Date

EXPERIMENT VS NATURE: USING AMPHIBOLES TO TEST
MODELS OF MAGMA STORAGE AND PRE-ERUPTIVE MAGMA
DYNAMICS PRECEDING THE 2006 ERUPTION OF AUGUSTINE
VOLCANO, ALASKA

A
THESIS

Presented to the Faculty
of the University of Alaska Fairbanks

in Partial Fulfillment of the Requirements
for the Degree of

DOCTOR OF PHILOSOPHY

By

Sarah Massey Henton, B.A., B.S.

Fairbanks, Alaska

May 2013

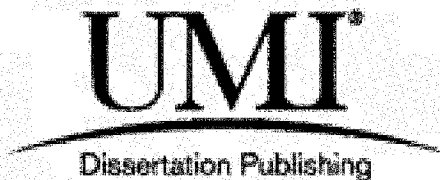
UMI Number: 3573018

All rights reserved

INFORMATION TO ALL USERS

The quality of this reproduction is dependent upon the quality of the copy submitted.

In the unlikely event that the author did not send a complete manuscript and there are missing pages, these will be noted. Also, if material had to be removed, a note will indicate the deletion.

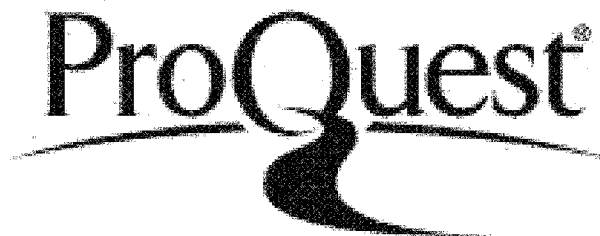


UMI 3573018

Published by ProQuest LLC 2013. Copyright in the Dissertation held by the Author.

Microform Edition © ProQuest LLC.

All rights reserved. This work is protected against unauthorized copying under Title 17, United States Code.



ProQuest LLC
789 East Eisenhower Parkway
P.O. Box 1346
Ann Arbor, MI 48106-1346

Abstract

This study investigates magmatic conditions preceding the 2006 eruption of Augustine Volcano through the use of amphibole compositions and textures. Due to their restricted stability region and common occurrence in calc-alkaline magmas, amphiboles are important for investigating pre-eruptive magmatic conditions at subduction zone volcanoes. Chapter 1 presents a study into geochemical and textural variations of natural amphibole phenocrysts in the erupted magmas. Magnesiohornblendes in the high- and low-silica andesites exhibit limited compositional variability. Intermediate-silica andesites and quenched mafic enclaves contain amphiboles that vary in composition and classification (magnesiohornblende-magnesiohastingsite-tschermakite). Compositional variations are controlled by temperature-dependent substitutions. Both high- and low-silica andesites represent magmas that were stored in the shallow crust at 4-8 km depth, remaining distinct due to a complex sub-surface plumbing system. Intermediate-silica andesites and quenched mafic inclusions represent newly formed hybrids of resident high- and low-silica andesite magmas and an intruding basalt. Chapter 2 presents the results of a phase equilibria study that refines the model for high-silica andesite storage. The natural phase assemblage was reproduced between 860–880°C and 120–200 MPa. Experimental plagioclase and groundmass glass compositions most closely replicate natural samples at ~130-140 MPa. Estimated storage conditions fall within the ranges suggested by natural petrological data and modeled storage depths from geodetic data. The high temperature stability of experimental quartz and biotite (not identified in natural samples) may reflect the high f_{O_2} of the Augustine system as well as the rapid kinetics associated with the crystal-poor sintered starting material of some experiments. Chapter 3 presents results of the first experimental study to target heating-induced amphibole reaction rim formation. Experiments show that reaction rims form on remarkably short timescales. They share mineralogical and textural features with natural reaction rims previously thought to represent decompression processes. Reaction rims cannot be simply classified on the basis of semi-quantitative observations. Rather, in-depth data collection (e.g. X-ray mapping), and the calculation of kinetic parameters (e.g. crystal nucleation rates), is necessary. Chapter 4 presents a new MATLAB® based program that performs mineral formula recalculations and the associated propagation of analytical uncertainty.

Table of Contents

	Page
Signature Page	i
Title Page	ii
Abstract.....	iii
Table of Contents	iv
List of Figures.....	x
List of Tables.....	xii
List of Other Materials	xiii
Acknowledgements	xiv
Quotations Page.....	xvi
Introduction	
i Project Rationale and Goals	1
ii Augustine Volcano: Geography, Geology, and the 2006 Eruption.....	2
iii Project Overview.....	3
Chapter 1: Pre-eruptive magmatic conditions at Augustine Volcano, Alaska, 2006: Evidence from amphibole geochemistry and textures	
1.1 Abstract.....	5
1.2 Keywords.....	6
1.3 Introduction	6
1.4 Background.....	7
1.4.1 Geographical and Geological Setting.....	7
1.4.2 Overview of the 2006 Eruption	8
1.5 Materials and Methods	9

	Page
1.5.1 Sample Selection	9
1.5.2 Electron Microprobe (EPMA).....	9
1.5.3 Amphibole Image Acquisition and Processing	10
1.6 Results	11
1.6.1 Amphibole Major Oxide Geochemistry	12
1.6.2 Reaction Rims	13
1.6.2.1 Reaction Rim Distribution and Widths	13
1.6.2.2 Reaction Rim Microlite Textures and Mineralogy.....	14
1.6.2.3 Reaction Rim Classification	14
1.7 Discussion.....	16
1.7.1 Geochemistry.....	16
1.7.1.1 Controls on Amphibole Composition.....	16
1.7.1.2 Quenched Mafic Inclusions Represent Replenishing Basalt?.....	17
1.7.1.3 High-Silica Andesite and Low-Silica Andesite Scoria: Resident Magmas?.....	18
1.7.1.4 Dense Low-Silica and Intermediate-Silica Andesites: Hybrid Magmas?	19
1.7.2 Reaction Rims: Textures, Mineralogy, and Processes	21
1.7.2.1 Previous Models for Reaction Rim Formation.....	21
1.7.2.2 Application to Augustine 2006.....	22
1.7.2.3 An Alternative Approach: Kinetic Model for Reaction Rim Formation.....	23
1.7.2.4 Mechanisms for Amphibole Breakdown.....	24
1.8 Concluding Statement	26
1.9 Acknowledgements	28
1.10 Figures	29
1.11 Tables	44
1.12 References	48

Chapter 2: Experimental constraints on magmatic storage conditions for the high-silica andesite of the 2006 eruption of Augustine Volcano, Alaska

2.1	Abstract.....	54
2.2	Keywords.....	55
2.3	Introduction	55
2.3.1	Prior Studies	56
2.4	Methodology.....	57
2.4.1	Experimental Methods.....	57
2.4.2	Analytical Methods	58
2.5	Results	59
2.5.1	Experimental Run Products.....	59
2.5.2	Experimental Mineral Compositions.....	60
2.5.3	Experimental Glass Compositions	62
2.6	Discussion.....	64
2.6.1	Attainment of Equilibrium	64
2.6.2	Phase Stability	67
2.6.3	Phase Compositions.....	68
2.6.4	Low Alkalis in Experimental Glasses	71
2.6.5	Biotite Crystallization from a Low-K Andesite	72
2.7	Conclusions: Model for Pre-Eruptive Magma Storage	73
2.8	Acknowledgements	74
2.9	Figures	75
2.10	Tables	85
2.11	References	90

	Page
Chapter 3: Experimental insights into the formation of heating- and decompression-induced amphibole reaction rims and implications for shallow-level magmatic processes at arc volcanoes	
3.1 Abstract.....	95
3.2 Introduction	96
3.3 Methodology.....	97
3.4 Results	98
3.4.1 Reaction Rim Mineralogy	98
3.4.2 Reaction Rim Textures.....	99
3.4.2.1 Thicknesses, Growth Rates, and Microlite Size	99
3.4.2.2 Reaction Rim Crystal Number Densities, Nucleation, and Growth Rates	100
3.5 Discussion.....	101
3.5.1 Initiation of Reaction Rim Formation	101
3.5.2 Separating Heating from Decompression-Induced Rim Formation.....	102
3.5.2.1 Mineralogy	102
3.5.2.2 Textures and Growth Rates	103
3.5.2.3 Discrimination by Rim Microlite Number Densities	104
3.5.3 Estimating Timescales of Disequilibrium	104
3.5.4 Observations of Reaction Rim Kinetics	105
3.5.5 Effects of Changing Oxygen Fugacity	106
3.5.6 Combined Disequilibrium Conditions: Simultaneous Heating and Decompression	107
3.5.7 Formation of Pseudomorphs.....	107
3.5.8 Implications for Natural Augustine Amphibole Reaction Rims	108
3.6 Conclusions	109
3.7 Acknowledgements	110

	Page
3.8 Figures	111
3.9 References	116

Chapter 4: MINERAL: A program for the propagation of analytical uncertainty through mineral formula recalculations

4.1 Abstract.....	119
4.2 Keywords.....	119
4.3 Introduction	120
4.4 Review of Past Work.....	122
4.5 MINERAL (MINeral ERror AnaLysis)	123
4.5.1 Mineral Specific Considerations	126
4.5.1.1 Feldspar	126
4.5.1.2 Olivine	126
4.5.1.3 Pyroxene.....	126
4.5.1.4 Spinel.....	127
4.5.1.5 Ilmenite.....	127
4.5.1.6 Amphibole	127
4.5.1.7 Garnet	128
4.5.1.8 Epidote.....	128
4.5.1.9 Mica.....	128
4.5.1.10 Generic	129
4.6 Testing MINERAL.....	129
4.6.1 Mineral Formula Recalculations	129
4.6.2 Formula Uncertainty Calculations.....	130
4.7 Conclusion.....	131

	Page
4.8 Acknowledgements	131
4.9 Figures	133
4.10 Tables	137
4.11 References	139
Conclusion	144
i References	146

List of Figures

	Page
Chapter 1: Pre-eruptive magmatic conditions at Augustine Volcano, Alaska, 2006: Evidence from amphibole geochemistry and textures	
Figure 1.1: Maps showing the location of Augustine Volcano	29
Figure 1.2: K ₂ O- (a) and Cr- (b) SiO ₂ variation diagrams	30
Figure 1.3: Histogram of lithological proportions from each eruptive phase	31
Figure 1.4: Transmitted light photomicrographs of representative amphiboles.....	32
Figure 1.5: Distribution of amphiboles with and without reaction rims	33
Figure 1.6: Amphibole classification	34
Figure 1.7: Compositions and modes of amphibole.....	35
Figure 1.8: Temperature and pressure sensitive coupled-substitutions.....	36
Figure 1.9: Distribution of amphibole rim thicknesses	37
Figure 1.10: Histogram of reaction rim microlite sizes.....	38
Figure 1.11: The distribution of mineral phases within reaction rim types.....	39
Figure 1.12: Variations in rim microlite sizes	40
Figure 1.13: Type 1 reaction rim BSE images and composite X-ray maps	41
Figure 1.14: Type 2 and 3 reaction rim BSE images and composite X-ray maps	42
Figure 1.15: Schematic depiction of the proposed model for the 2006 eruption	43
 Chapter 2: Experimental constraints on magmatic storage conditions at Augustine Volcano, Alaska	
Figure 2.1: Maps showing the location of Augustine Volcano	75
Figure 2.2: High-silica andesite oxygen fugacity and temperatures	76
Figure 2.3: Phase diagram	77
Figure 2.4: Modal abundance of minerals in natural HSA and selected experiments	78

	Page
Figure 2.5: BSE images of experimental groundmass	79
Figure 2.6: Experimental and natural plagioclase compositions.....	80
Figure 2.7: Experimental and natural pyroxene compositions.....	81
Figure 2.8: Experimental and natural amphibole compositions.....	82
Figure 2.9: Harker plots of experimental and natural glass compositions	83
Figure 2.10: Near isobaric variations in experimental glass major oxide compositions.....	84
Chapter 3: Experimental insights into the formation of heating- and decompression-induced amphibole reaction rims and implications for shallow-level magmatic processes at arc volcanoes	
Figure 3.1: Composite X-ray maps of experimental amphibole reaction rims	111
Figure 3.2: Natural and experimental amphibole reaction rim mineralogies.....	112
Figure 3.3: Average reaction rim thicknesses, growth rates, and microlite sizes	113
Figure 3.4: Kinetic features of experimental and natural reaction rims	115
Figure 3.5: Composite X-ray maps of notable textural features	115
Chapter 4: MINERAL: A program for the propagation of analytical uncertainty through mineral formula recalculations	
Figure 4.1: Recalculated amphibole cations with and without propagated errors	133
Figure 4.2: Screen shot of the MINERAL GUI	134
Figure 4.3: MINERAL vs. published recalculation programs	135
Figure 4.4: Total Fe, Fe ³⁺ and Fe ²⁺ in magnetite plotted against calculated error	136

List of Tables

	Page
Chapter 1: Pre-eruptive magmatic conditions at Augustine Volcano, Alaska, 2006: Evidence from amphibole geochemistry and textures	
Table 1.1: Augustine 2006 eruption phases and lithologies.....	44
Table 1.2: Sample inventory for Augustine 2006 amphiboles	45
Table 1.3: Representative amphibole compositions	46
Table 1.4: Representative amphibole rim analyses	47
Chapter 2: Experimental constraints on magmatic storage conditions at Augustine Volcano, Alaska	
Table 2.1: Representative starting material compositions.....	85
Table 2.2: Experiments and experimental products	86
Table 2.3: Representative experimental glass compositions.....	87
Table 2.4: Representative experimental plagioclase compositions.....	88
Table 2.5: Representative experimental pyroxene, amphibole, and biotite compositions	89
Chapter 4: MINERAL: A program for the propagation of analytical uncertainty through mineral formula recalculations	
Table 4.1: MINERAL uncertainty calculations.....	137
Table 4.2: Comparison to past studies.....	138

List of Other Materials

DVD 1: Appendices

Chapter 1: Pre-eruptive magmatic conditions at Augustine Volcano, Alaska, 2006: Evidence from amphibole geochemistry and textures

Appendix 1.1: Amphibole Phenocryst Compositions

Appendix 1.2: Amphibole Reaction Rim Occurrence and Thicknesses

Appendix 1.3: Reaction Rim Microlite Data

Chapter 2: Experimental constraints on magmatic storage conditions at Augustine Volcano, Alaska

Appendix 2.1: Natural HSA Phase Compositions

Appendix 2.2: Experimental Phase Modes

Appendix 2.3: Experimental Phase Compositions

Chapter 3: Experimental insights into the formation of heating- and decompression-induced amphibole reaction rims and implications for shallow-level magmatic processes at arc volcanoes

Appendix 3.1: Reaction Rim Microlite Data

Appendix 3.2: Reaction Rim Thickness Data

Appendix 3.3: Crystal Nucleation Theory Calculations

Appendix 3.4: Experimental Phenocryst Compositions

Chapter 4: MINERAL: A program for the propagation of analytical uncertainty through mineral formula recalculations

Appendix 4.1: Error Propagation Equations

Appendix 4.2: Error Propagation Equation Variables

Acknowledgements

First and foremost I would like to thank my family for their unwavering love and support: Mum and Dad, you always made me believe that I could be or do anything I chose. It is from you that I have drawn all my good qualities (although I must take responsibility for the bad) and I thank you for instilling in me a love of travel, a quest for learning and knowledge, and the need to question the world around me. Tom and George, without siblings such as you I would never have developed the requisite levels of competitiveness and tenacity so important for success in academia. Last, but by no means least, Silvio. From our first meeting on Woodlands Beach, Montserrat, I knew that I would never be alone again. You are a truly beautiful person who deserves a beautiful life. There is nobody I would rather spend the years with, exploring the volcanoes of the world, playing lightning-round Trivial Pursuit, cooking up a storm in the kitchen, chilling out in coffee shops, curling up on the sofa with Jeeves and Wooster or Hercule Poirot, and even undertaking endless bike rides through dog-infested neighborhoods. You are my friend, my family, and my love. Without you I would be lost.

I owe a debt of gratitude to my committee for their guidance and patience. I am grateful to my supervisor, rock star and all-round wonder-woman Jessica Larsen for taking me on and making my dream of being a volcanologist a reality. I could not have asked for a better teacher. Your tireless efforts have provided me with a first-class education and an abundance of incredible experiences. I hope in time you can forgive me for ruining so many of your MHC vessels with melted precious metals. Michelle Coombs, for letting me crash in your basement (twice), for letting me play with your beautiful new SEM, for your thoughtful (and lengthy) reviews of my terrible writing, and for many life changing field experiences. Pavel Izbekov, while I am grateful for our many interesting scientific (and not so scientific) discussions, I must primarily thank you for rescuing me from numerous snowfields. Without you I might still be a quivering, miserable, wreck, stuck on a glacier below Katmai Volcano. Jeff Freymueller, thank you for your insightful comments that have improved my work, and thank you for educating me (through the great medium of social media) on so many aspects of American politics and on area conversion calculations. Finally, Ken

Severin, committee member, professor, political commentator, therapist, boss, mentor, mechanic, landlord, and friend. I cannot express how much you have enriched my life.

I would also like to thank my exceptional friends and dedicated colleagues here at the University of Alaska Fairbanks and the Alaska Volcano Observatory for making my graduate school experience so rewarding, both professionally and personally. You are too numerous to be named in full, but a special mention goes to several particular partners in crime: Taryn Lopez, David McAlpin, Jill Shipman, Wenyu Gong, Anna Perttu, Andrew Dunn, Amanda Lindoo, and Owen Neill.

“There are, on the one hand, skeptical philosophers, who think there is nothing certain in nature, because there is misconception in the mind of man; on the other hand, there are many credulous amateurs, who go to nature to be entertained as we go to see a pantomime: But there are also superficial reasoning men, who think themselves qualified to write on subjects on which they may have read in books, subjects which they may have seen in cabinets, and which, perhaps, they have just learned to name; without truly knowing what they see, they think they know those regions of the earth which never can be seen; and they judge of the great operations of the mineral kingdom, from having kindled a fire, and looked into the bottom of a little crucible”

James Hutton

“The heights by great men reached and kept, were not obtained by sudden flight. But they, while their companions slept, were toiling upward in the night”

Henry Wadsworth Longfellow

“Anti-intellectualism has been a constant thread winding its way through our political and cultural life, nurtured by the false notion that democracy means that `my ignorance is just as good as your knowledge”

Isaac Asimov

INTRODUCTION

i PROJECT RATIONALE AND GOALS

This study presents the results of an investigation into pre-eruptive magma storage conditions and pre-eruptive magma dynamics prior to the 2006 eruption of Augustine Volcano, Alaska. The results, which incorporate investigations of natural petrological features, in addition to targeted phase equilibria, heating, and decompression experiments, significantly refine our understanding of the shallow plumbing system at Augustine Volcano.

Augustine presents a unique opportunity for an investigation of this type. Due to its high rate of activity, proximity to populations and infrastructure, and ease of access, Augustine Volcano is one of the most comprehensively monitored and studied volcanoes in the region (Power et al., 2010). Its products were well poised for a study that combines the petrologic analysis of natural and experimental materials. For example, Augustine lacks the specific phase assemblage required for the use of the Al-in-hornblende technique for estimating the pressure at which the amphibole crystals last equilibrated (e.g. Johnson & Rutherford, 1989). It is possible to use other available techniques such as volatiles-in-melt-inclusions to estimate storage pressures, but they are themselves subject to great uncertainty (Scaillet & Evans, 1999). Through experimental investigations, this study aims to provide an independent verification of pressures and temperatures of shallow magmatic storage at Augustine Volcano.

Augustine also provides an opportunity to study the effects of oxidation state on mineral stabilities and on magmatic responses to disequilibrium e.g. pre-eruptive heating and/ or decompression. At oxygen fugacity (fO_2) of 0 to 0.5 log units below Re-ReO (RRO~NNO+2), Augustine magmas are unusually highly oxidized for the Aleutian arc (Larsen et al., 2010). Highly oxidized magmas are not common, but they erupt at some of the world's most hazardous volcanoes (e.g. Mt Pinatubo, The Philippines and Shiveluch, Kamchatka, Russia). Therefore, it is important that we gain a better understanding of their geochemistry and petrology.

Much of this study focuses on the hydrous silicate mineral amphibole. Despite a low modal

abundance, amphiboles are an important phase in the Augustine deposits. Due to their sensitivity to changing magmatic conditions and to their restricted chemical-thermo-barometric stability, amphiboles provide an opportunity to investigate pre-eruptive magma conditions. Amphibole compositions can yield information regarding the storage conditions (e.g. temperatures, pressures, oxygen fugacity). Further, removing amphiboles from their stability field leads to their decomposition and to the subsequent formation of reaction rims of anhydrous minerals. These reaction rims allow the investigation of pre-eruptive magma dynamics, as this decomposition is generally caused by magma heating and/ or by ascent driven decompression and melt dehydration (e.g. Rutherford & Hill, 1993).

ii **AUGUSTINE VOLCANO: GEOGRAPHY, GEOLOGY, AND THE 2006 ERUPTION**

Augustine is a 1254-m-tall Pleistocene–Holocene stratovolcano located on a 10–12km diameter island near the eastern end of the Aleutian volcanic arc. It is the most active volcano in Alaska’s Cook Inlet region and presents a number of local and regional hazards, including volcanically induced tsunamis, ash fall, and ash plumes that threaten aviation (Waythomas & Waitt, 1998). The volcano came into existence in the late Pleistocene when magma erupted through Jurassic aged sedimentary deposits that formed a small island. There is limited evidence from these early eruptions. Exposed deposits from the late Holocene (2200 years B.P.) to the present day are well documented (Waitt & Begè, 2009).

Historical eruptions occurred in 1812, 1883, 1935, 1964, 1976, 1986, and 2006, producing crystal-rich andesites. The last 3 eruptions all progressed from early explosive to late effusive phases over a scale of weeks to months (Waitt & Begè, 2009). These eruptions produced similar ranges in whole-rock compositions. The injection of hot mafic magmas into cool residual magmas stored at shallow levels apparently triggered these episodes of unrest (Johnston, 1978; Roman et al., 2006; Larsen et al., 2010). Roman et al. (2006) propose a shallow storage region of interconnected dikes that prevent full homogenization of magmas. They infer that the short time interval between historical eruptions allows the maintenance of this complex storage structure as the frequent influx of new magma prevents the small dikes from freezing.

The 2006 eruption followed almost 20 years of quiescence. Activity began with a 6-month precursory phase, and progressed through a 2-week explosive phase and a 1-week continuous phase, before ending with a 2-month effusive phase. Four major lithologies comprise low- to medium-K crystal-rich andesites categorized on the basis of silica content and/or textural characteristics. Minor lithologies include fine-grained gabbroic inclusions and quenched mafic inclusions. Volatile concentrations in melt inclusions indicate a storage region no shallower than 4–6 km depth (Webster et al., 2010). Geodetic estimates suggest a cylindrical storage region with a top at 2.5–4.5 km and a base at 6.5–10.5 km (Cervelli et al., 2010).

iii PROJECT OVERVIEW

This study aims to answer several questions about the 2006 Augustine magmas raised by prior research: 1) Is the inferred 4–6 km storage depth of the high silica andesite magma accurate, based on the preliminary petrology and geophysical observations? 2) How important is decompression versus heating due to magma mixing in creating the amphibole textures? 3) How does oxidation state affect amphibole breakdown in comparison with more reduced volcanic systems? 4) Is it possible to refine magma mixing timescales and/or ascent rates by examining amphibole reaction rims?

Amphiboles in the 2006 lithologies are compositionally and texturally complex. In Chapter 1 an extensive study into amphibole compositions and textures is presented. The results of this study help to refine models of pre-eruptive magma storage and shed new light on pre-eruptive magma mixing and the genesis of hybrid magmas. In Chapter 2 experimental phase equilibria results investigating storage conditions for the high-silica andesites of the 2006 Augustine eruption are presented. The results of this study significantly refine previous estimates on the temperature and pressure constraints of shallow magma storage at Augustine Volcano. In Chapter 3 the results of the first experimental study to target the heating-induced formation of amphibole reaction rims are presented. Results show that amphibole reaction rims may not be simply classified on the basis of semi-quantitative textural and mineralogical observations and that past studies may have misclassified, and as such misinterpreted, reacted magmatic amphiboles. In Chapter 4 a MATLAB® based program, MINERAL, which provides mineral formula recalculations and

the associated propagation of analytical uncertainty through these calculations is presented. It is a common scientific principle that the quantification and reporting of error or uncertainty is an essential aspect of data presentation. However, published atoms per formula unit (a.p.f.u.) rarely include uncertainties. The MINERAL package provides a rapid and user-friendly tool for performing these calculations.

CHAPTER 1:

Pre-eruptive magmatic conditions at Augustine Volcano, Alaska, 2006: Evidence from amphibole geochemistry and textures¹

1.1 ABSTRACT

Variations in the geochemistry and texture of amphibole phenocrysts erupted from Augustine Volcano in 2006 provide new insights into pre- and syn-eruptive magma storage and mixing. Amphiboles are rare but present in all magma compositions (low- through high-silica andesites) from the 3-month-long eruption. Unzoned magnesiohornblende amphibole in the high- and low-silica andesites exhibit limited compositional variability, relatively high SiO₂ (up to 49.7 wt%), and relatively low Al₂O₃ (< 11.1 wt%). Intermediate-silica andesites and quenched mafic enclaves contain amphiboles that vary in composition (e.g. SiO₂: 40.8–48.9 wt% & Al₂O₃: 6.52–15.2 wt %) and classification (magnesiohornblende-magnesiohastingsite-tschermakite). Compositional variation in amphibole is primarily controlled by temperature-dependent substitutions. Both high- and low-silica andesites represent remnant magmas that were stored in the shallow crust at 4–8 km depth, remaining distinct due to a complex sub-surface plumbing system. Intermediate-silica andesites and quenched mafic inclusions represent pre-eruptive hybrids of resident high- and low-silica andesite magmas and an intruding basalt. Amphiboles in explosive phase high-silica andesites are largely euhedral and unreacted, consistent with the high magma flux rates from depth during this phase (up to 13,800 m³/s). Phenocrysts from the other lithologies have reaction rims that range from 1 to >1000 μm in thickness. Reaction rim microlite sizes correlate with reaction rim thicknesses. Reaction rims <50 μm thick contain microlites 1–10 μm in length and reaction rims >80 μm thick contain microlites 10–100 μm in size. Differentiating between heating and decompression induced amphibole reaction rim formation is problematic because of a lack of experimental constraints available in

¹ Henton De Angelis, S., Larsen, J. & Coombs, M. Pre-eruptive magmatic conditions at Augustine Volcano, Alaska, 2006: Evidence from amphibole geochemistry and textures. Accepted for publication, *Journal of Petrology*

the literature. This study attempts a new approach to assessing reaction rim formation, based on kinetic theory of crystal nucleation and growth, in which the differences in reaction rim textures represent different degrees of amphibole disequilibrium. Large crystal and low number densities suggest relatively lower levels of disequilibrium resulting in growth-dominated crystallisation. Smaller crystals and larger number densities are indicative of higher nucleation rates and a high driving force.

1.2 KEYWORDS: Amphibole; Andesite; Magma mixing; Magma storage; Reaction rims

1.3 INTRODUCTION

Numerous studies have used amphibole compositions and textures to investigate magma storage and ascent processes (e.g. Bachmann & Dungan, 2002; Browne & Gardner, 2006; Devine et al., 1998; Johnson & Rutherford, 1989; Rutherford & Devine, 2003; Rutherford & Hill, 1993). Magma ascent rates and eruption styles primarily depend on the pressure in the storage region and on the physical and chemical properties of the magma: volatile content, temperature, density, viscosity, and crystallinity (Rutherford, 2008 and references therein). These parameters are largely determined by crustal storage conditions. Improving our understanding of magma storage conditions and ascent dynamics through focused studies of magmatic minerals leads to improved prediction of eruptive style and is thus essential for hazard mitigation.

Although exact stability boundaries vary between magmas, OH bearing amphibole is only stable at pressures greater than ~100 MPa (4 km) and in melts containing at least 4 wt% H₂O (Rutherford & Hill, 1993). The somewhat restricted stability region and common occurrence in intermediate calc-alkaline magmas make amphiboles important for investigating magma storage and ascent conditions at subduction zone volcanoes. When forced out of stability amphiboles decompose to form aggregate reaction rims of anhydrous minerals (referred to hereafter as 'microlites'). Based on experimentally calibrated decompression models, reaction rim thicknesses have been used to estimate magma ascent rates (Rutherford and Hill, 1993; Browne & Gardner, 2006). Other investigations have discussed heating-induced reaction rim formation (Garcia & Jacobson, 1979; Murphy et al., 2000; Buckley et al., 2006;

Plechov et al., 2008), although only four heating experiments exist and thus heating-induced rim formation is almost completely uncalibrated experimentally (Browne, 2005).

This study uses the geochemical and textural characteristics of phenocrystic amphiboles, in conjunction with bulk rock compositions, to deduce pre-eruptive magmatic processes and conditions for the well-described 2006 eruption sequence from Augustine Volcano, Alaska. Despite low overall abundances in most Augustine 2006 samples (Larsen et al., 2010), the compositional and textural variations in the amphibole population suggest a complex story of pre- and syn-eruptive magma mixing. Amphibole scarcity, as compared to analogous volcanoes (e.g. Redoubt, Alaska; Coombs et al., 2012, and Soufrière Hills, Montserrat; e.g. Murphy et al., 2000), and their uneven distribution among samples may be indicative of a storage region that straddles the mineral's thermal and/or pressure stability boundaries. The evidence presented herein supports the hypothesis that the eruption was triggered by an influx of mafic magma from depth. Older magmas stored below the volcano since at least 1986 were remobilised by heating and by variable amounts of mixing with the fresh mafic magma. This study also presents a quantitative method for analysing the textures and mineralogy of reaction rim microlites. The resulting model for reaction rim formation, based on accepted crystallisation kinetics theory, proposes a new approach to classifying amphibole reaction rims, a common feature in magmas from around the world.

1.4 BACKGROUND

1.4.1 Geographical and Geological Setting

Augustine is a 1254-m-tall Pleistocene–Holocene stratovolcano located on a 10–12km diameter island near the eastern end of the Aleutian volcanic arc (Figure 1.1). It is the most active volcano in Alaska's Cook Inlet region and presents a number of local and regional hazards, including volcanically induced tsunamis, ash fall, and ash plumes that threaten aviation (Waythomas & Waitt, 1998). Due to its high rate of activity, proximity to populations and infrastructure, and ease of access, Augustine is one of the most comprehensively monitored and studied volcanoes in the region (Power et al., 2010).

Historical eruptions occurred in 1812, 1883, 1935, 1964, 1976, 1986, and 2006, producing

compositionally similar, crystal-rich andesites and low-silica dacites. The last 3 eruptions all progressed from early explosive to late effusive phases over a scale of weeks to months (Waitt & Begè, 2009), produced similar ranges in whole-rock compositions, and were each apparently triggered by the injection of hot mafic magmas into cool, residual magmas stored at shallow levels (Johnston, 1978; Roman et al., 2006; Larsen et al., 2010). Roman et al. (2006) propose a shallow storage region of interconnected dikes that prevent full homogenisation of magmas. They infer that the short time interval between historical eruptions allows this complex storage structure to be maintained as the frequent influx of new magma prevents the small dikes from freezing.

1.4.2 Overview of the 2006 Eruption

A full description of the 2006 eruption appears in Power et al. (2010) and is briefly summarised here. Activity began with a 6-month precursory phase (Table 1.1), and progressed through a 2-week explosive phase and a 1-week continuous phase, before ending with an effusive phase that lasted for almost 2 months. The total erupted volume was $\sim 0.1 \text{ km}^3$ (Coombs et al., 2010).

Four major lithologies comprise low- to medium-K andesites (Figure 1.2a; Table 1.1), categorised on the basis of silica content and/or textural characteristics: high-silica andesites (HSA; 62.2–63.3 wt% SiO_2); low-silica andesite scoria (LSAS; 56.5–58.7 wt% SiO_2); dense low-silica andesites (DLSA; 56.4–59.3 wt% SiO_2); and intermediate-silica andesites (ISA; 58.3–61.1 wt% SiO_2). Although all major lithologies were present throughout the eruption, their proportions varied with time (Figure 1.3; Vallance et al., 2010). The andesites contain 36–55 volume % phenocrysts of plagioclase (An_{48} – An_{90}), augite, orthopyroxene, Fe-Ti oxides (magnetite and ilmenite), olivine, and amphibole (Larsen et al., 2010).

Crystal rich (> 70 volume %) minor lithologies include fine-grained gabbroic inclusions (FGGI: 54.5–58.2 wt% SiO_2 ; Larsen et al., 2010; Coombs and Vazquez, 2012) and quenched mafic inclusions (QMI: 49.7–60.6 wt% SiO_2 ; Steiner et al., 2012; Browne & Vitale, 2011; this study). Quenched mafic inclusions are primarily found in high-silica andesite deposits. They exhibit chilled margins and rounded morphology suggestive of quenching in cooler host magma (Steiner et al., 2012).

Iron-titanium (Fe-Ti) oxide thermometry methods yield temperatures of 810–970°C for the major lithologies (Larsen et al., 2010) and 840–940°C for the quenched mafic inclusions (Browne & Vitale, 2011). Magmas are highly oxidised with fO_2 values of approximately nickel-nickel oxide (NNO) +1.5 log units, slightly below the rhenium-rhenium oxide (RRO) buffer.

Larsen et al. (2010) conclude that two-stage mixing preceded the eruption. The first stage involved mixing between the high-silica andesite and an intruding mafic magma, forming a low-silica hybrid (erupted as the LSAS). The second stage involved mixing between the high-silica andesite and the newly generated low-silica andesite to produce the intermediate-silica andesite. Volatile concentrations in melt inclusions indicate a storage region no shallower than 4–6 km depth (Webster et al., 2010). Similarly, geodetic estimates suggest a cylindrical storage region with the top at 2.5–4.5 km and the base at 6.5–10.5 km (Cervelli et al., 2010).

1.5 MATERIALS AND METHODS

1.5.1 Sample Selection

This study uses multiple samples from all eruptive phases and major lithologies (Table 1.2). A total of 123 amphiboles in 28 major lithology thin sections (each representing a different hand-specimen) were identified, although amphibole distribution is not uniform. Some thin sections contain multiple amphibole phenocrysts, whereas others from the same deposits contain none. Given the relative scarcity of amphiboles, all identified phenocrysts from the major lithologies were used in this study. An additional 22 amphibole phenocrysts from 3 quenched mafic inclusions were also analysed.

1.5.2 Electron Microprobe (EPMA)

Amphibole major-element compositional data were collected on a Cameca SX50 electron microprobe at the University of Alaska Fairbanks. This instrument is equipped with one EDAX energy-dispersive spectrometer (EDS) and four wavelength-dispersive spectrometers. Analyses were conducted with a

focused (1–5 μm) 15kV accelerating voltage, 10nA beam. Data were collected at 10 to 30 μm intervals along rim-to-rim or core-to-rim transects. Amphibole mineral formulae were recalculated based on normalisation to 13 cations and assuming 23 oxygen ions (Leake et al., 1997). This method includes Si+Ti+Al+Fe+Mn+Mg in the T- and C-sites (M1, M2, M3). Ca is excluded from the C-site and Fe^{2+} , Mn and Mg are excluded from the B-site (M4). The $\text{Fe}^{2+}/\text{Fe}^{3+}$ ratio was calculated stoichiometrically. For calcic amphibole, normalisation to 13 cations is thought to produce more accurate stoichiometric $\text{Fe}^{2+}/\text{Fe}^{3+}$ estimation than normalisation to 15 cations (e.g. Al'meev et al., 2002). Uncertainties on recalculated data reflect the 1-sigma standard deviation of 'n' oxide analyses for each phenocryst propagated through the mineral recalculation using full error propagation methods (Giaramita & Day, 1990; De Angelis & Neill, 2012). Amphiboles were classified according to Leake et al. (1997), based on the occupancy of the A- (Na + K), B- (Ca, Na), C- (Mg, Fe^{2+} , Fe^{3+} , Ti, Mn, Al_{vi}), and T- (Si, Al_{iv}) sites.

1.5.3 Amphibole Image Acquisition and Processing

Photomicrographs of amphibole phenocrysts were acquired using a Diagnostic Spot InSight Color digital camera mounted on a petrographic microscope, at magnifications between $2.5\times$ (1 μm represented by 0.3 pixels) and $20\times$ (1 μm represented by 2.7 pixels). Backscattered electron (BSE) images and X-ray maps of reaction rims were collected using a JEOL JSM-6510 Scanning Electron Microscope, equipped with an IXRF Iridium Ultra EDS, at the U.S. Geological Survey, Anchorage, at magnifications between $30\times$ and $6000\times$ and at resolutions of 640×480 to 1280×960 pixels. Images were acquired with a 20kV accelerating voltage, large spot size (85), and a 10 mm working distance.

Reaction rim images were measured using the National Institute of Health (NIH) ImageJ software package. Phenocryst lengths were measured along the longest axis, and when crystal orientation permitted, along the C axis (inferred from crystal habit and cleavage). Mean reaction rim thickness values were calculated from 20 measurements taken at regular spatial intervals around each reaction rim. The mineral phase, size, aspect ratio, and distances from the unreacted amphibole core and from the surrounding glass were recorded for 24–244 microlites per reaction rim. Microlite size was defined as the Feret's Diameter

(FD), the longest distance between any two points around the boundary of the crystal, as measured by ImageJ. The number of microlites measured depended on the size of the amphibole and on the thickness of the reaction rim. Where possible (small amphibole or those with very thin reaction rims), 100% of reaction rim microlites were analysed. Where reaction rims contained large numbers of microlites, regions of interest (ROIs) were established at multiple (5–10) locations around the reaction rim. Wherever feasible, ROIs extended from the amphibole core to the reaction rim-glass boundary. All microlites within each ROI were analysed. For each rim, average two-dimensional crystal number densities (CND) were calculated from grain counts within square ROIs. The size of these ROIs depended on the magnification of the image and on the total reaction rim thickness. Repeat CND calculations were conducted on selected reaction rims to calculate representative standard deviations.

1.6 RESULTS

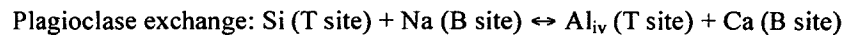
With just one exception (high-silica andesite sample 06AUMC004c; Table 1.2), thin sections from the major lithologies contain <1 modal % amphibole (Larsen et al., 2010). These amphiboles are phenocrysts and range in length from 50 to 1000 μm , with a mean of 350 μm . Quenched mafic inclusions contain both phenocrysts and microphenocrysts of amphibole. Microphenocrysts likely represent recent crystallisation following the mixing-induced quenching of the mafic inclusions (e.g. Bacon, 1986; Coombs et al., 2002; Foley et al., 2012), occurring not longer than 1 month prior to eruption (Vitale, 2012). In this study, the use of amphibole from the quenched mafic inclusions was restricted to phenocrysts > ~150 μm in length. Quenched mafic inclusions contain 5 to 18 modal % amphibole phenocrysts that range in length from 60 to 750 μm , with a mean of 220 μm . Of the major lithologies, the high-silica andesite is the only one in which the majority of amphibole phenocrysts are euhedral (Figure 1.4a) and do not exhibit reaction rims (Figure 1.5). The other major lithologies contain amphibole with a range of textures, including rimmed, unrimmed, euhedral, resorbed, and fragmented (Figure 1.4b–d). Amphiboles in the quenched mafic inclusions never have reaction rims but are often resorbed (Figure 1.4e–f).

1.6.1 Amphibole Major Oxide Geochemistry

Augustine 2006 amphiboles are calcic (Table 1.3) and have compositions that vary between magnesiohornblende, tschermakite, and magnesiohastingsite (Figure 1.6). The spread in compositions is consistent with other andesitic arc volcanoes, such as Redoubt, Alaska (Coombs et al., 2012) and Soufrière Hills Volcano, Montserrat (Murphy et al., 2000). Compositions vary both within and between lithologies, although individual phenocrysts are unzoned.

With the exception of 3 phenocrysts, high- and low-silica andesite amphiboles are all magnesiohornblende (Figure 1.6). These amphiboles exhibit the least compositional variation between phenocrysts (Figure 1.7a, b) and contain relatively high SiO_2 (44.3–49.7 wt%) and low Al_2O_3 (7.15–11.1 wt%). Dense low-silica andesite, intermediate-silica andesite, and quenched mafic inclusion amphiboles contain bimodal populations of high- and low-Al amphiboles, varying between the tschermakite, magnesiohastingsite, and magnesiohornblende fields (Figure 1.6 & 1.7). These amphibole phenocrysts show relatively wide ranges in their oxide compositions ($\text{SiO}_2 = 40.8\text{--}48.9$, $\text{Al}_2\text{O}_3 = 6.52\text{--}15.2$ wt %).

Key substitutions that control the composition of calcic amphiboles from calc-alkaline volcanic sequences are the Al-Tschermak, Ti-Tschermak, Plagioclase, and Edenite exchanges (Bachmann & Dungan, 2002):



Plotting Al_{iv} (tetrahedral Al) against the cations involved in each substitution highlights the relative importance of each substitution (Bachmann & Dungan, 2002; Shane & Smith, 2013). Al_{iv} varies by approximately 1.4 atoms per formula unit (a.p.f.u.) across all samples: from <0.8 to almost 2.2 (Figure 1.8).

Al_{iv} , representative of the Al-Tschermak exchange, varies by approximately 0.35 a.p.f.u. (excluding outliers). C-site Ti, representative of the Ti-Tschermak exchange, varies by approximately 0.15 a.p.f.u. B-site Ca, indicative of the plagioclase exchange, varies by approximately 0.3 a.p.f.u. A-site alkalis (Na + K), a proxy for the Edenite exchange, vary by approximately 0.6 a.p.f.u. With the exception of Ti, each of the proxy elements changes in a 1:1 ratio with Al_{iv} during substitution. A.p.f.u changes in Ti are accompanied by twice the change in Al_{iv} . Reported uncertainties are significant, and the slope of the data clearly exceeds the uncertainties only in the Edenite exchange.

1.6.2 Reaction Rims

1.6.2.1 Reaction Rim Distribution and Widths

Most amphiboles in the major lithologies exhibit reaction rims (Figure 1.5). Rim-width distribution can be described in terms of both eruptive phase and lithology (Figure 1.9). Most early explosive phase amphiboles have reaction rims. These rims are predominantly <40 μm in width, although a few are 70–80 μm in width (Figure 1.9a). In contrast, while only a small number of late explosive phase phenocrysts have reaction rims, they are generally thicker, ranging from 61–200 μm . Continuous phase phenocrysts have either thin (1–20 μm) or thick (201–300 μm) reaction rims. The effusive phase contains the highest proportion of amphiboles with reaction rims, which range from 11 to >1000 μm .

The high-silica andesite (HSA) is the only major lithology in which unreacted amphiboles are dominant (>80%; Figure 1.5). However, the few reacted amphiboles have thick rims (up to 300 μm). More than 90% of low-silica andesite (LSA) amphiboles are reacted. Reaction rim thicknesses are predominantly 1–40 μm (Figure 1.9b), although single outliers reside in the 51–60 μm , 71–80 μm , and > 1000 μm bins. Most dense low-silica andesite (DLSA) amphiboles have reaction rims (75%) with thicknesses of 1–200 μm . Almost 90% of intermediate-silica amphiboles (ISA) have reaction rims and over 50% appear in transmitted light to be opacitised around phenocrysts edges and along cleavage lines. Rims range from 1–10 μm in width, with a single exception of 200–300 μm .

1.6.2.2 Reaction Rim Microlite Textures and Mineralogy

The microlites contained within the amphibole reaction rims vary in size. Microlite sizes (Feret's Diameter or FD) correlate with reaction rim thickness (Figure 1.10a). Where the total reaction rim thickness is <50 μm , all microlites are <10 μm . Within this range, the majority of microlites are 1–6 μm (Figure 1.10b). Where total reaction rim thickness is 50–80 μm , reaction rim microlites are 2–20 μm . Where total reaction rim thickness is >80 μm , microlites are always >10 μm . There is no correlation between microlite size and lithology, amphibole composition, or eruptive phase. Reaction rim microlites include orthopyroxene, clinopyroxene, plagioclase, and Fe-Ti oxides (Figure 1.11, Figure 1.12, Table 1.4). However, in the thinnest reactions rims (<10 μm), some 'microlites' are actually fragments of amphibole, mechanically separated from the parent phenocryst.

1.6.2.3 Reaction Rim Classification

Reaction rims in this study are primarily classified on the basis of reaction rim thickness. Subdivisions are based on microlite mineralogy.

1) Type 1 reaction rims are <50 μm thick and contain the smallest (1–10 μm) microlites (Figure 1.10). Type 1a reaction rims contain amphibole fragments and Fe-Ti oxide microlites (Figure 1.11a, Figure 1.13a). Type 1b reaction rims contain amphibole fragments and orthopyroxene, clinopyroxene, Fe-Ti oxides and plagioclase microlites (Figure 1.11a, Figure 1.13b). Type 1c reaction rims have a similar mineralogy to Type 1b, however amphibole is not present (Figure 1.11a, Figure 1.13c). While some individual microlites in Type 1 reaction rims are up to 10 μm across, on average they are < 5 μm in size (Figure 1.12). Fe-Ti Oxides represent the smallest microlites (<2.5 μm), while there is little difference in size between pyroxene and feldspar microlites (2.5 to 5 μm ; Figure 1.12a). There is no systematic variation in microlite size across the Type 1 rims (Figure 1.12b).

2) Type 2 reaction rims are 50–80 μm thick. They contain microlites of 3–30 μm in size (Figure 1.10). In order of decreasing abundance, Type 2 reaction rims contain orthopyroxene, clinopyroxene,

plagioclase, and Fe-Ti oxides (Figure 1.11b). Type 2a reaction rims contain a single population of plagioclase crystals of uniform composition (Figure 1.14a). Type 2b reaction rims contain relatively calcic plagioclase near the amphibole phenocryst and relatively sodic plagioclase near the reaction rim-glass boundary (Figure 1.14b). In both Type 2a and Type 2b reaction rims, Fe-Ti oxides represent the smallest microlites, whilst plagioclase microlites are the largest (Figure 1.12a). For each given microlite phase, the mean size is greater in Type 2a reaction rims than in Type 2b reaction rims (Figure 1.12a).

3) Type 3 reaction rims are $>80 \mu\text{m}$ thick, and contain the largest ($10\text{--}100 \mu\text{m}$) microlites (Figure 1.12). In order of decreasing abundance, Type 3 reaction rims contain orthopyroxene, plagioclase, clinopyroxene, and Fe-Ti oxides. Type 3a reaction rims contain a single population of plagioclase crystals of uniform composition (Figure 1.11c, Figure 1.14c). Type 3b reaction rims contain more calcic plagioclase near amphibole and more sodic plagioclase near the boundary with the glass (Figure 1.11c, Figure 1.14d). Microlite sizes are strongly dependent on microlite phase. In both Type 3a and Type 3b reaction rims, Fe-Ti oxides represent the smallest microlites, whilst plagioclase microlites represent the largest microlites (Figure 1.12a). For Fe-Ti oxides, clinopyroxene and plagioclase, the mean microlite size is greater in Type 3a reaction rims than in Type 3b reaction rims (Figure 1.12a). Orthopyroxene microlites are larger in Type 3b reaction rims. In Type 3 reaction rims, mean microlite size clearly increases from amphibole-rim boundary outwards to the rim-glass boundary (Figure 1.12b). Microlites closest to the host amphibole are on average $<20 \mu\text{m}$ in size. Microlites on the outer edges of the rim, in contact with the surrounding glass, have mean sizes of $25\text{--}40 \mu\text{m}$.

It is important to note that proportions of each mineral within reaction rims (Figure 1.11) represent mineral modes. In some cases, these values may differ from the total area accounted for by a particular mineral. For example, oxides tend to be numerous, but individual oxide microlites are very small (Figure 1.12a). Multiple oxide microlites may be required to account for the same surface area as taken up by a single microlite of orthopyroxene or plagioclase.

1.7 DISCUSSION

1.7.1 Geochemistry

1.7.1.1 Controls on Amphibole Composition

The sensitivity of amphiboles to changing melt composition, temperature, pressure, and volatile content has made them a target for use in modelling magmatic conditions. At the same time, this sensitivity to multiple parameters makes attributing changes to any one variable problematic. Popular models for interpreting magmatic conditions relate amphibole compositions directly to pressure and/or temperature (e.g. Hammarstrom & Zen, 1986; Johnson & Rutherford, 1989; Ridolfi et al., 2010). There are a number of reasons why the application of these models to Augustine amphiboles is inappropriate. Firstly, none account for the influence of bulk composition and the compositions of coexisting melts and other mineral phases on amphibole compositions. Some models (e.g. Johnson & Rutherford, 1989), developed for near solidus plutonic systems, circumvent this issue by requiring a specific mineral assemblage (e.g. quartz, sanidine, biotite, sphene) to buffer melt composition. These phases are not found in Augustine 2006 magmas. For this reason, pressure and temperature calculations for Augustine using such models are subject to high degrees of uncertainty. Amphibole pressure-temperature stability curves at Augustine will be determined through the use of forthcoming experimental phase equilibria. However, for the purposes of this study, the relative contributions from the four primary coupled substitutions controlling magmatic amphibole chemistry are used to infer *relative* differences in magmatic conditions for different amphibole populations.

The Al-Tschermak exchange is generally held to be primarily pressure sensitive, whereas the Plagioclase and Edenite exchanges are temperature dependent (e.g., Bachmann & Dungan, 2002). Some studies suggest that the amphibole-melt partitioning of Ti is affected by both pressure and water activity (Adam et al., 2007), although most show that Ti variation and the Ti-Tschermak substitution are also controlled by temperature (e.g. Bachmann & Dungan, 2002; Ernst & Liu, 1998). On this basis, the Ti-Tschermak exchange is the least useful because it may reflect changes in pressure, water activity, and

temperature, or any combination of these.

In Augustine amphiboles, positive correlations for each of the 4 exchange relationships indicate that all substitutions are active and account for almost 100% of the variation in amphibole compositions (Figure 1.8). The Al-Tschermak exchange accounts for approximately 21% of the variation, whereas the Ti-Tschermak, Plagioclase, and Edenite exchanges account for 21%, 18%, and 39%, respectively. The statistically most significant correlation is for the temperature-controlled Edenite exchange. These results suggest that melt temperature is the primary control on amphibole compositions. Statistically indistinguishable amphibole compositions (at the 95% confidence interval) between high- and low-silica andesites (Figure 1.7) indicate that for the primary lithologies, melt composition plays a lesser role to physical conditions in controlling amphibole composition at Augustine. The high-Al amphibole in the dense low-silica andesites, intermediate-silica andesites, and in the quenched mafic inclusions (Figure 1.8) formed from a higher temperature, and most likely higher pressure, melt than the low-Al amphibole. Low-Al amphiboles are found in all lithologies, but in the high-silica andesite and low-silica andesite scoria they represent the entire population (Figure 1.7).

1.7.1.2 Quenched Mafic Inclusions Represent Replenishing Basalt?

Larsen et al. (2010) suggest that the 2006 eruption was triggered by an influx of new basalt from depth into the shallow storage region. However, at the time of publication no direct samples of this mafic end member had been observed. Since then, quenched mafic inclusions have been identified in the Augustine 2006 deposits (Steiner et al., 2012). The quenched mafic inclusions anchor the mafic end of the linear mixing array in bulk-rock major oxide chemistry (Figure 1.2a). However, their wide range in composition (50–60 wt% SiO₂; Steiner et al., 2012) indicates that even if some of the inclusions represent an influx of new basalt, others are hybrids. This is consistent with the results of Browne & Vitale (2011), who conclude that the inclusions did not erupt in a pristine compositional state and underwent varying degrees of pre- and syn-eruptive hybridisation.

Of the three mafic inclusions investigated in this study, two contain single populations of high-Al

amphibole phenocrysts (>11 wt% Al₂O₃) and one contains a bimodal population of high- and low-Al (<10 wt% Al₂O₃) amphibole phenocrysts (Figure 1.7b). At the 95% confidence level, low-Al amphiboles in the quenched mafic inclusions are statistically indistinguishable from those in the high-silica andesite. High-Al amphiboles in the quenched mafic inclusions are statistically indistinguishable from high-Al phenocrysts in the intermediate-silica andesite (at the 95% confidence level), consistent with pre-eruptive hybridisation. However, the enclave containing the bimodal population has one of the lowest bulk-rock SiO₂ contents reported (50.9 wt% SiO₂). In contrast, enclaves with higher SiO₂ contain single populations of high-Al amphiboles.

1.7.1.3 High-Silica Andesite and Low-Silica Andesite Scoria: Resident Magmas?

Larsen et al. (2010) infer the formation of low-silica andesite scoria from the mixing of remnant high-silica andesite with an influx of basalt, likely represented by the quenched mafic inclusions. However, the amphibole distribution sheds doubt on this hypothesis. Low-silica andesite scoria and high-silica andesites both contain predominantly magnesiohornblende, with a small number of tschermakite outliers (Figure 1.6). In contrast, quenched mafic inclusions contain predominantly tschermakitic amphiboles, with a few that are magnesiohastingsite. If the low-silica andesite scoria were a hybrid formed from high-silica andesite and basalt magma end members, it should contain two phenocryst populations, one inherited from each parent. On the basis of major oxide geochemistry, approximately 50% each of those end member lithologies (e.g., quenched mafic inclusions and high-silica andesite) would be required to create a hybrid of low-silica andesite scoria composition. The high-silica andesite contains on average <1 modal % amphibole phenocrysts. The quenched mafic inclusions contain 5–18 modal % amphibole phenocrysts. Thus, the majority of inherited phenocrysts should be similar to those from the quenched mafic inclusions (Figure 1.7). Instead, the low-silica andesite amphibole population is similar to those in the high-silica andesite.

The evidence suggests that the low-silica andesite does not represent a recent hybrid magma and that both low-silica andesite scoria and high-silica andesite magmas resided in the shallow plumbing

system beneath Augustine prior to 2006 and erupted with little or no pre- or syn-eruptive hybridisation. Amphibole compositional data suggests that those magmas formed, or at least were stored for an extended period, at similar temperatures. In contrast, whereas Fe-Ti oxide based temperature estimates show a cluster of low-T values for the high-silica andesite ($838^{\circ}\text{C} \pm 14^{\circ}\text{C}$), they indicate a much larger range in temperatures for the low-silica andesites ($904^{\circ}\text{C} \pm 47^{\circ}\text{C}$; Larsen et al., 2010). Fe-Ti oxides re-equilibrate on a scale of hours to days, while it takes significantly longer for amphibole compositions to reflect changes in magmatic conditions. The low-silica andesite underwent a greater degree of heating than the high-silica andesite prior to eruption, as reflected in the higher (and greater range) of apparent temperatures. Amphibole compositions likely do not reflect this heating as it occurred immediately prior to eruption on a timescale too short for the re-equilibration of amphibole compositions. Employing the Roman et al. (2006) storage model, both low and high-silica andesite magmas could have been stored in the plexus of dikes without interacting. This hypothesis is supported by recent results from uranium series isotope analyses on samples from the 2006 eruption (Thompson, 2011). Deficits in the $^{210}\text{Pb}/^{226}\text{Ra}$ ratio of explosive and effusive phase low-silica andesite samples indicate that the lithology likely represents a remnant magma, possibly a crystal fractionate of an older basalt, stored below the volcano, and not a recent hybrid between resident high-silica andesite and a new basalt or basaltic andesite magma.

1.7.1.4 Dense Low-Silica and Intermediate-Silica Andesites: Hybrid Magmas?

Of all lithologies, only the dense low-silica andesite and intermediate-silica andesite have magnesiohastingsite phenocrysts in common with the quenched mafic inclusions. Larsen et al. (2010) concluded that the dense low-silica andesite probably represents a degassed version of the low-silica andesite scoria. However, dense low-silica andesite amphiboles exhibit a greater spread of compositions (Figure 1.6). Although their whole rock major oxide compositions are indistinguishable, differences between the low-silica andesite scoria and dense low-silica andesite are seen in the trace element whole rock data (Larsen et al., 2010). Over 90% of the low-silica andesite scoria and about half of the dense low-silica andesite whole-rock samples have Cr values that fall 10–20 ppm below the main mixing trend

(Figure 1.2b). Larsen et al. (2010) attributed these differences to olivine settling in the interim between the main eruptions of the low-silica andesite scoria (early explosive phase) and the dense low-silica andesite (effusive phase). However, these differences are probably because low-silica andesite scoria magma is not a 2006 hybrid. The dense low-silica andesite with the lower Cr values (circa 50–65 ppm) may be a degassed version of the low-silica andesite scoria magma while those with the elevated Cr (circa 60–85 ppm), in alignment with the main mixing trend, represent recent mixing between the high silica-andesite and quenched mafic inclusion magmas. While amphibole data is too limited to be conclusive, it does lend support to this theory. The lowest-Al amphiboles from the dense low-silica andesite, those most similar to those in low-silica andesite scoria (Figure 1.7b), are from samples with depleted whole-rock Cr. In contrast, the highest-Al amphiboles in the dense low-silica andesite come from samples with elevated whole-rock Cr, consistent with recent hybridisation.

Intermediate-silica andesite samples contain high- (>11.5 wt% Al_2O_3) and low-Al (<9.5 wt% Al_2O_3) amphibole populations, consistent with two-component mixing between high-silica andesite and a basaltic end member. Similar to the dense low-silica andesite, intermediate-silica andesite amphiboles have a wide range of compositions (Figures 1.6 and 1.7), including tschermakite and magnesiohastingsite phenocrysts. Given the presence of high-Al amphiboles in intermediate-silica andesite magma, it is unlikely that the low-silica end member in this mixing process was represented by low-silica andesite scoria, as suggested by Larsen et al. (2010). More probable is the formation of the intermediate-silica andesite from the mixing of high-silica andesite with replenishing basalt, represented by the quenched mafic inclusions. The occurrence of statistically indistinguishable magnesiohornblende crystals in the high-, intermediate-, and dense low-silica samples, and indistinguishable high-Al amphibole in the intermediate- and dense low-silica and quenched mafic inclusion samples provide support for the hypothesis that the intermediate-silica andesites and most of the dense low-silica andesites represent recent hybrid magmas.

1.7.2 Reaction Rims: Textures, Mineralogy, and Processes

1.7.2.1 Previous Models for Reaction Rim Formation

Volcanic amphibole reaction rim formation is commonly attributed to dehydration during ascent, thermal decomposition caused by an influx of a higher temperature magma, fluxing of the magma with a CO₂ rich melt, or shallow level oxidation (Rutherford & Hill, 1993). From semi-quantitative studies of natural magmatic amphiboles (Garcia & Jacobson, 1979; Devine et al., 1998; Murphy et al., 2000; Rutherford & Devine, 2003) reaction rims in past studies have been classified as follows:

Type A: Very thin (<10 μm), fine-grained (microlite sizes of 1–10 μm) intergrowths of Fe-Ti oxides and pyroxene that are often referred to as ‘Black Type’ (Garcia & Jacobson, 1979) or ‘Opaque’ (due to their opaque appearance in transmitted light microscopy; Devine et al., 1998; Murphy et al., 2000). These are attributed to oxidation and dehydrogenation within a lava dome or flow.

Type B: Thin (<40 μm), medium-grained (microlite sizes of 1–30 μm) intergrowths of pyroxene, plagioclase, and Fe-Ti oxides, classified as ‘Gabbroic’ (Garcia & Jacobson, 1979), ‘Fine Grained’ (Devine et al., 1998; Murphy et al., 2000), or ‘Type 1’ (Rutherford & Devine, 2003). These are attributed to melt dehydration during ascent driven decompression.

Type C: Thick (generally >200 μm), coarse grained (microlite sizes of 30–300 μm) intergrowths of pyroxene, plagioclase, and Fe-Ti oxides. These reaction rims are generally attributed to thermal decomposition or to prolonged re-crystallisation in magmas that stall at shallow depths (Devine et al., 1998; Murphy et al., 2000; Rutherford & Devine, 2003).

The generation of amphibole reaction rims via decompression has also been explored experimentally (Rutherford & Hill, 1993; Browne & Gardner, 2006). Rutherford & Hill (1993) investigated reaction rim formation at 860°C and 900°C using dacite magmas from Mount St. Helens, while Browne & Gardner (2006) investigated reaction rim formation at 840°C using andesite magmas from Redoubt Volcano, Alaska as starting material. Both studies aimed to use experimental reaction rim growth rates to provide a calibration for assessing magmatic ascent rates from natural amphiboles. However, use of their calibrations on Augustine amphiboles is inappropriate for several reasons. First, the large differences in

experimental rim growth rates between the two studies highlights the uniqueness of each calibration to the volcanic system. These studies were performed on samples with different melt compositions, more reduced oxygen fugacity, and different inferred magma temperatures than those observed at Augustine Volcano. In addition, experimentally grown reaction rims rarely exceed 40 μm (Browne & Gardner, 2006). Thus, the results of experimental studies have to be extrapolated to infer ascent rates from thicker natural reaction rims. Finally, the amphibole breakdown reaction induced by decompression experiments is non-linear (Browne & Gardner, 2006). This means that syn-eruptive variations in ascent rate and path may explain a broad range of reaction rim widths and textures.

However, a general observation of note is that decompression-induced reaction rims are characterised by the presence of orthopyroxene. In contrast, heating reaction rims are characterised by clinopyroxene (Browne, 2005).

1.7.2.2 Application to Augustine 2006

The 3 reaction rim types identified in the Augustine 2006 samples (Figure 1.11, Figure 1.12) are generally not consistent with the 3 reaction rim types identified in the literature. For example, while a number of Augustine 2006 amphibole reaction rims are both $<10 \mu\text{m}$ in thickness and opaque in transmitted light, X-ray maps indicate that reaction rim mineralogy is inconsistent with the Type A classification. This highlights the inadequacy of transmitted light microscopy for the classification and analysis of amphibole reaction rims. In another example, while Augustine Type 2 reaction rims are mineralogically and texturally consistent with the traditional Type 2 classification they tend to be significantly thicker (50 to 80 μm on Augustine amphiboles, as compared to $<40 \mu\text{m}$ in past classification systems). Finally, while the very thick Type C reaction rims of past studies ($> 200 \mu\text{m}$ thickness) are not identified in the Augustine samples, many Augustine reaction rims do contain coarse microlites that are consistent with the coarse-grained texture of the Type C reaction rims.

The lack of correlation between Augustine amphibole reaction rims and past classifications means that past studies of natural magmatic systems cannot be used to infer the type of disequilibrium (e.g.

heating vs. decompression) that is inducing amphibole reaction rim formation at Augustine.

1.7.2.3 An Alternative Approach: Kinetic Model for Reaction Rim Formation

Kinetic studies of plagioclase crystallisation, employing both cooling and decompression experiments, have investigated nucleation and growth rates by measuring crystal number densities (CND), shapes, and grain size as a function of experimental timescale (e.g., Muncill and Lasaga, 1988; Hammer and Rutherford, 2002). Nucleation and growth rates, plotted as a function of the thermodynamic driving force, typically show separate but overlapping curves. Nucleation rates are highest when the degree of undercooling is high, and growth rates are highest at lower undercoolings (e.g. Hammer and Rutherford, 2002; Brugger & Hammer, 2010; Hammer, 2008 and references therein). The most acicular grains are observed at high degrees of undercooling, consistent with the system reacting to a large degree of forcing away from equilibrium (e.g., high DG; Hammer & Rutherford, 2002). Thus, high CND's, acicular shapes, and small crystal sizes are indicative of nucleation-dominated crystallisation during reactions in which the system is forced far from equilibrium over short timescales. In contrast, smaller CND's and larger, more equant grains indicate lower degrees of undercooling and a growth-dominated crystallisation regime in a system reacting to a smaller degree of forcing away from equilibrium (e.g. low DG).

Amphibole reaction rims are multi-component, and their formation not only depends upon the degree of decompression or heating but is also a function of melt composition (Coombs et al., 2012) and probably on magma oxidation state. However, to first order, if we view the crystallisation of each phase with an amphibole reaction rim as following similar kinetic principles, we can follow a kinetic approach that may help further refine what the different reaction rim textures mean in terms of the conditions of their formation. The caveat is that additional experimental calibrations of amphibole reaction rates under different conditions of heating and decompression are required before such a model can be widely applied across different volcanic systems.

Microlites in Augustine amphibole reaction rims vary by size, shape, and number density (Table 1.4). Given the dependency of crystal shape on crystal orientation within the thin section, for the purposes

of this study only crystal size and number densities are considered. Type 1 reaction rim microlites are small ($<10\ \mu\text{m}$; Figure 1.12) and have high CND's (50,000 to $\sim 400,000$ crystals per mm^2). Type 1a represents the initiation of breakdown, with the mechanical separation of amphibole fragments from the main phenocryst. This separation could be due to decomposition occurring preferentially along planes of weakness. Type 1b and 1c represent the dissolution of amphibole fragments and the initial crystallisation of anhydrous phases. These reaction rims are primarily nucleation-dominated and are the initial response to changes in the amphibole's environment.

In contrast, Type 3 reaction rims contain large microlites (mean sizes of 10 to 40 μm depending on microlite phase and position within the reaction rim; Figure 1.12) and much lower CND's (300 to 6000 crystals per mm^2). Type 3 reaction rims represent growth-dominated crystallisation. Type 3 reaction rims show increasing microlite size in the outer rim (Figure 1.12), supporting the hypothesis that outer rim microlites, which formed early in reaction rim formation, have been growing for the longest.

Type 2 reaction rim microlites have CND's and microlite sizes intermediate between Types 1 and 3 reaction rims. They most likely represent a transitional zone between nucleation- and growth-dominated regimes, and thus intermediate reaction timescales.

1.7.2.4 Mechanisms for Amphibole Breakdown

This model provides a reaction-kinetics basis for determining the relative degree of disequilibrium in the system and the point to which the amphibole breakdown reaction has progressed in a qualitative way. However, it currently cannot effectively discriminate between forcing mechanisms, e.g. heating, decompression, or changes in melt composition, nor can it predict reaction timescales in a quantitative way.

Given the small total thickness of Type 1 reaction rims, it is likely that disequilibrium was experienced for a relatively short period of time. While the formation of Type 1 rims by heating in the hours prior to eruption cannot be discounted, it is unlikely that this was the case at Augustine. The duration of the precursory phase and the high degree of hybridisation in the erupted magmas indicate that pre-eruptive heating at Augustine took place over a timescale of weeks to months. It is simplest to explain

Type 1 reaction rims by moderately-paced ascent (and decompression) followed by quenching.

Type 2 and 3 reaction rims could signify either slower decompression rates, stalling at shallow levels in the conduit, heating, or some combination of all. Evidence for heating in Augustine 2006 samples, seen in all major lithologies with the exception of the high-silica andesite, includes an abundance of disequilibrium textures (e.g. skeletal plagioclase, banded textures at both the micro- and macroscopic scales), large ranges in Fe-Ti oxide temperature estimates, and the presence of mafic enclaves with quench textures (Steiner et al., 2012). Amphibole reaction rim formation has been produced in just 4 heating experiments (Rutherford & Devine, 2003; Browne, 2005). Each of these produced heavily clinopyroxene-dominated reaction rims. In contrast, while Augustine reaction rims contain both ortho- and clinopyroxene, orthopyroxene is always dominant (Figure 1.11). Thus, two scenarios are possible: 1) The final temperature of heated magmas was within the thermal stability of Augustine amphibole and all reaction rims are decompression induced; or 2) in Augustine Volcano magmas, heating-induced reaction rims form without clinopyroxene as the dominant pyroxene phase. The first scenario is unlikely to be the case as Fe-Ti oxide pairs in the low-silica andesite suggest that Augustine magmas were heated to at least 970°C prior to eruption. While the thermal stability of amphibole in the Augustine system has not been confirmed experimentally, studies on similar volcanic systems such as Soufrière Hills Volcano, Montserrat (Rutherford & Devine, 2003) and Redoubt Volcano, Alaska (Browne and Gardner, 2006) show the limits of amphibole stability at <900°C. In contrast, scenario 2 is entirely plausible and reflects the individuality of magmatic systems. Phase crystallisation within the reaction rim is most likely a reflection of the initial amphibole composition and melt composition and not reflective of the disequilibrium forcing mechanism.

An interesting feature of some Type 2 and 3 reaction rims is the changes in the relative An content of plagioclase microlites. Type 2a and 3a reaction rims contain single populations of plagioclase with uniform An contents. In contrast, the small plagioclase microlites of Types 2b and 3b are more sodic in outer rims and more calcic in inner rims (Figure 1.11, Figure 1.12). This indicates that microlite compositions evolve as the reaction rim develops.

Wide variations in reaction rim thickness are often seen in single Augustine thin sections. This could indicate non-uniform ascent or storage conditions. Magma batches stored in different dikes may have

been subjected to different degrees of heating and/or may have ascended at different rates through different dikes, before combining in the shallow conduit prior to eruption.

In the case of Augustine, the only amphibole populations for which the forcing mechanism (or lack thereof) can be inferred with any confidence are the unreacted amphibole of the late explosive phase high-silica andesite and those with the thinnest, finest-grained reaction rims (Type 1). The lack of reaction rims on high-silica andesite amphiboles is due to a number of reasons: 1) amphiboles underwent little or no pre-ascent disequilibrium in the storage region. High-silica andesite magmas show no evidence for pre-eruptive heating, magma mixing, or changes in magma geochemistry; 2) the relatively low temperature and high viscosity of the high-silica melts retarded amphibole breakdown, in turn stalling the supply of nutrients to the surrounding melt (Coombs et al., 2012); 3) timescales of ascent and eruption were short enough to inhibit amphibole breakdown. There is strong independent evidence to suggest that late explosive phase high-silica andesite magmas did undergo rapid ascent. This phase was characterised by high flux rates (13,800 m³/s; Coombs et al., 2010) and the emplacement of the Rocky Point pyroclastic flow, coincident with major deflation indicative of rapid magma withdrawal at depth (Cervelli et al., 2010). The few outlying late explosive phase high-silica andesite amphiboles that do display reaction rims (including all classification types: Figure 1.15a), likely represent antecrysts from pockets of magma that were stuck along the conduit walls and were swept to the surface during the high-flux Rocky Point event.

1.8 CONCLUDING STATEMENT

On the basis of amphibole geochemistry and textures a revised model of magma storage and movement during the 2006 eruption of Augustine Volcano is presented (Figure 1.15). The high- and low-silica andesites (including the low-silica andesite scoria and most of the dense low-silica andesite) probably represent magmas stored in the shallow crust at depths of 4–8 km, since at least 1986, and perhaps longer (Figure 1.15a). These magmas remained chemically distinct as a result of the segregated dike structure of the storage system (e.g., Roman et al., 2006). The amphibole stability boundary for the Augustine system likely intersects the storage region, accounting for the scarcity of amphiboles and their uneven distribution

within samples. The eruption was triggered by the intrusion of a fresh mafic magma (likely represented by the quenched mafic inclusions) from the deep crust into the shallow storage system, similar to the model of Larsen et al. (2010). However, the amphibole compositional data indicates that the low-silica andesite scoria is not a hybrid, and the replenishing magma may have only heated and remobilised this magma, which rose to the surface relatively unmixed (Figure 1.15b). At the end of the explosive phase, the pressure differential in the now open pathway pulled more viscous high-silica andesite from the storage region into the conduit for eruption. Mixing and mingling between the high-silica andesite and the mafic magma formed intermediate-silica andesite and the remainder of the dense low-silica andesite (Figure 1.15c). Finally, the remaining degassed low-silica andesites erupted effusively, forming two lava flows and a final lava dome. One of these degassed low-silica magmas represented the final remnants of the original low-silica andesite and the other a high-silica andesite-quenched mafic inclusion hybrid.

The majority of Augustine amphiboles exhibit reaction rims. This study proposes a new approach to assessing reaction rim textures based on established models of crystallisation kinetics. This approach focuses on the relative magnitude of disequilibrium imposed on a phenocryst but does not currently allow for differentiation between heating- and decompression-induced reaction rims. The interpretation of reaction rim textures must be accompanied by additional evidence for origination by heating or decompression (Rutherford & Hill, 1993; Plechov et al., 2008).

Complex minerals such as amphibole are often misused in petrological studies. For example, the inappropriate use of geothermobarometry models on amphibole in magmas that fall outside of the limits of the calibration is common. This study has shown that even without the use of these models, basic amphibole compositional and textural data can be a powerful tool in helping to understand the sub-surface plumbing of arc volcanoes. Further, this study marks an attempt to encourage a more quantitative approach to the analysis of amphibole textures. However, further experimental work on the heating and decompression of magmas, both at Augustine and for other volcanoes, is needed to test this method and to calibrate a more rigorous thermodynamic model for the formation of amphibole reaction rims.

1.9 ACKNOWLEDGEMENTS

The authors are indebted to Ken Severin and to the Alaska Volcano Observatory. Critical and constructive comments by Carrie Brugger, John Adam, Jenni Barclay, Wendy Bohrson, and Jorge Vazquez greatly improved the manuscript. This work was supported by a grant from the National Science Foundation (NSF EAR 0911694).

1.10 FIGURES

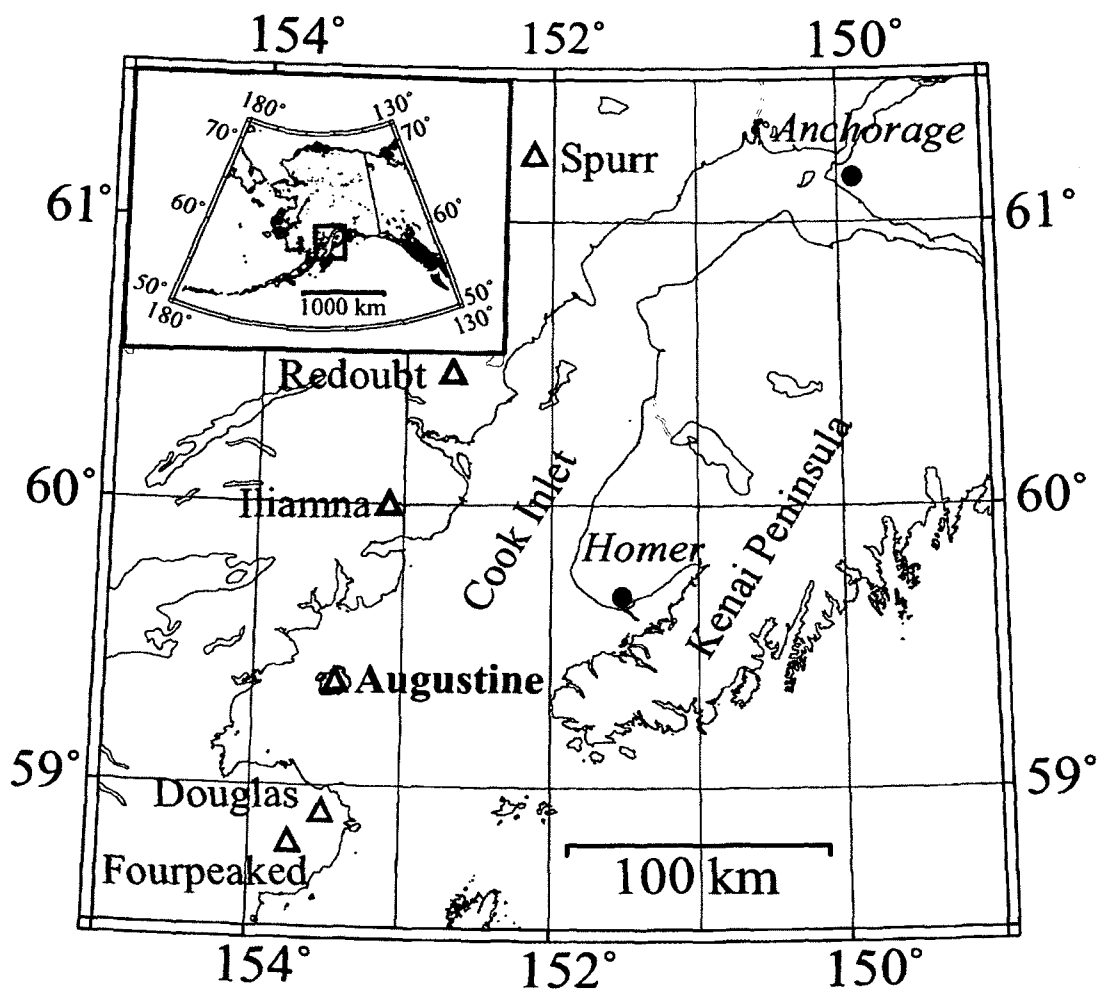


Figure 1.1 Maps showing the location of Augustine Volcano. Inset map shows Alaska with the Cook Inlet region highlighted. Triangles denote volcanoes and circles denote major settlements.

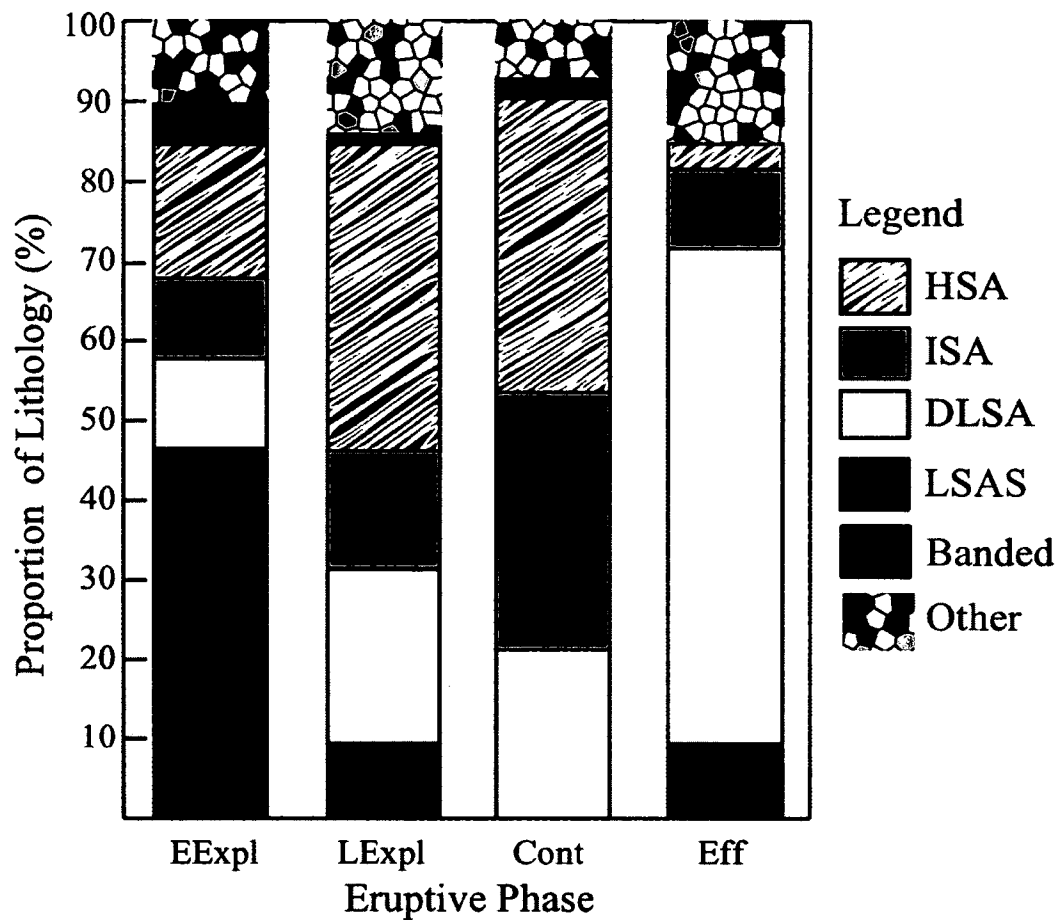


Figure 1.3 Histogram of lithological proportions from each eruptive phase. Figure after Vallance et al., 2010. The 'other' category contains oxidised clasts and crystal clots not included in this study. EExpl = early explosive phase; LExpl = late explosive phase; Cont = continuous phase; Eff = effusive phase. DLSA = Dense low-silica andesite; LSAS = low-silica andesite scoria; HSA = high-silica andesite; ISA = intermediate-silica andesite.

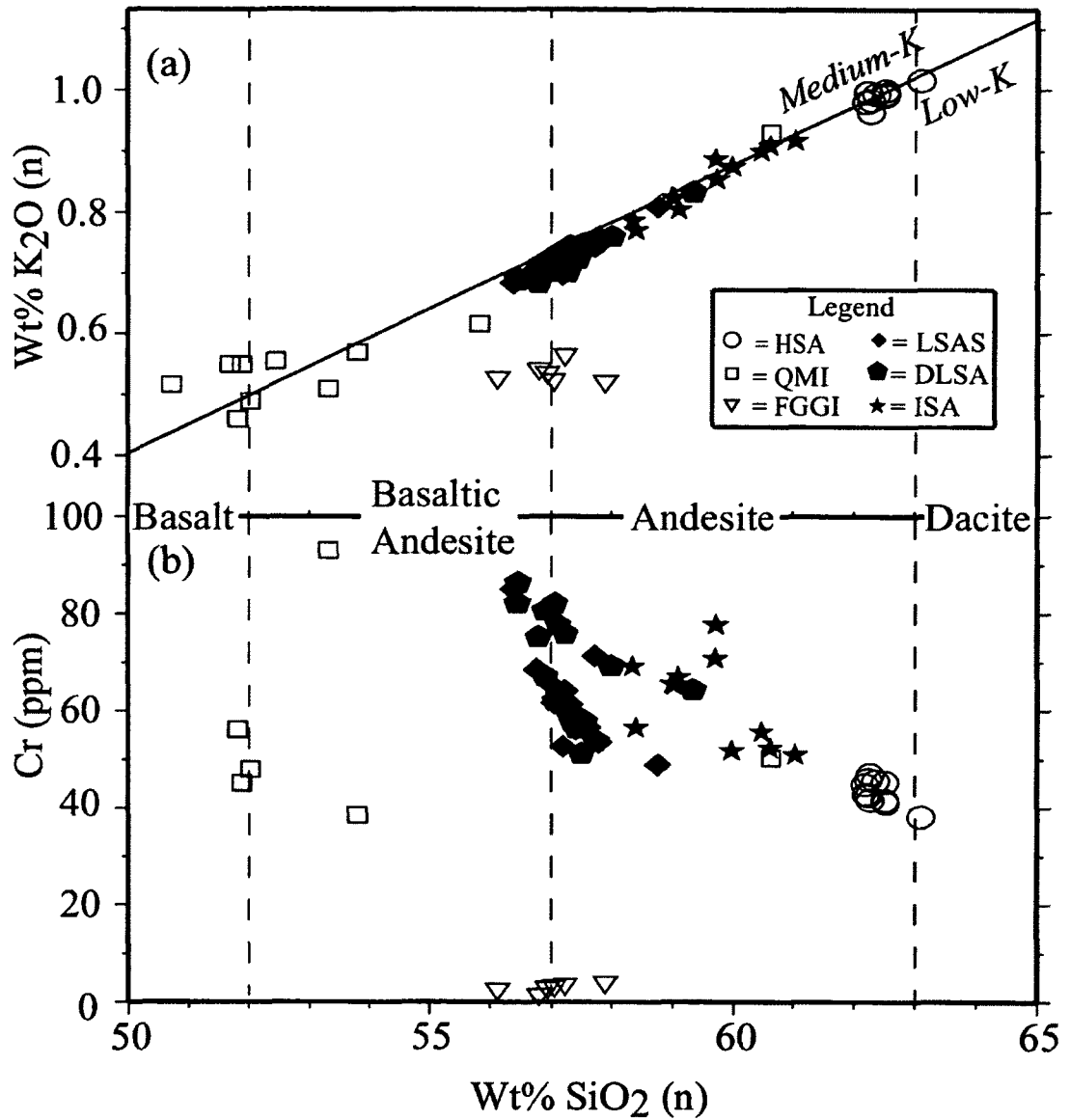


Figure 1.2 K₂O- (a) and Cr- (b) SiO₂ variation diagrams. Figure adapted from Larsen et al. 2010 (with additional data from Steiner et al., 2012). The solid line in plot (a) denotes the Low-K/ Medium-K boundary for the classification of andesite magmas (Gill, 1981). All data are derived by XRF. Major oxide data are based on normalisation to 100%. Data points are categorised by lithology: DLSA = Dense low-silica andesite; LSAS = low-silica andesite scoria; HSA = high-silica andesite; ISA = intermediate-silica andesite; QMI = quenched mafic inclusion; FGGI = fine-grained gabbroic inclusions.

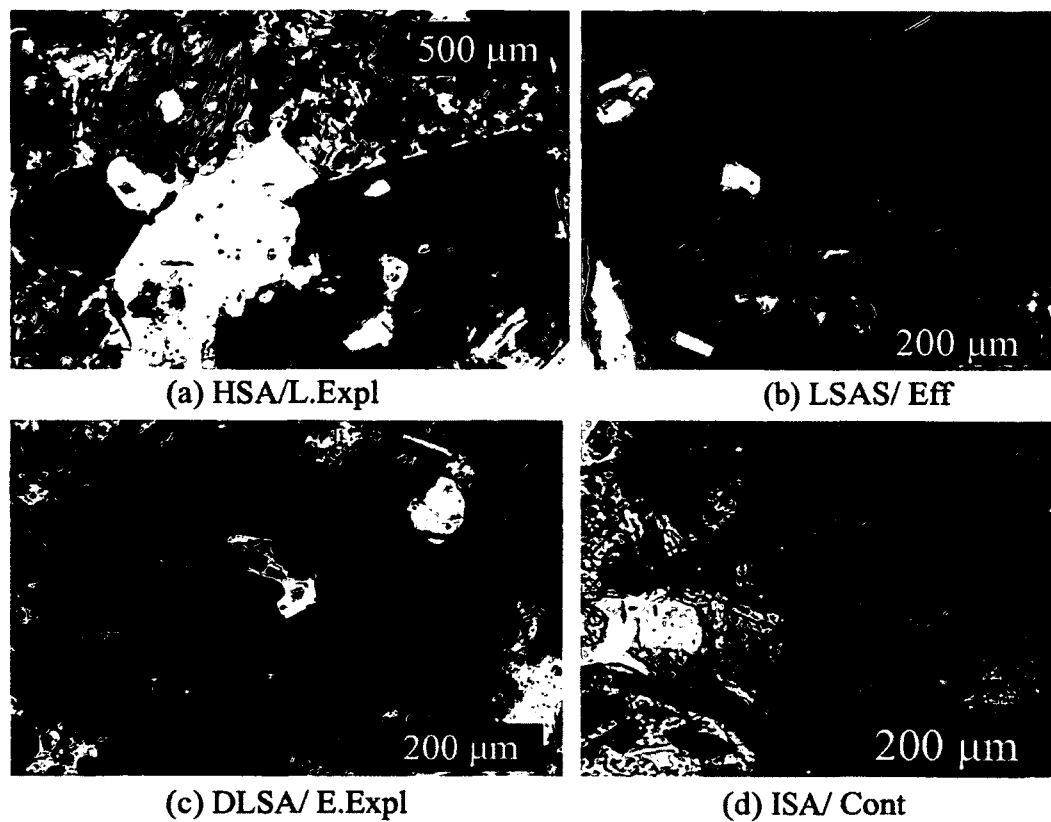


Figure 1.4 Transmitted light photomicrographs of representative amphiboles. (a) high-silica andesite\ late explosive phase; (b) low-silica andesite scoria\ effusive phase; (c) dense low-silica andesite\ early explosive phase; (d) intermediate silica-andesite\ continuous phase.

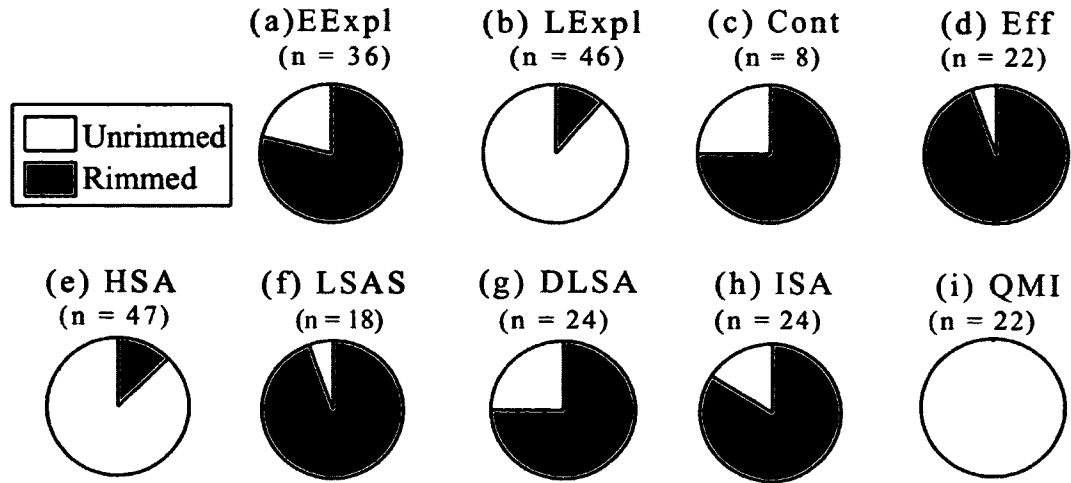


Figure 1.5 Distribution of amphiboles with and without reaction rims. Results are sorted by lithology (a–d) and by eruptive phase (e–j). The number of phenocrysts in each tally is denoted by ‘n’. Figures a–d exclude data for the quenched mafic inclusions, in which all amphiboles are unreacted. EExpl = early explosive phase; LExpl = late explosive phase; Cont = continuous phase; Eff = effusive phase. DLSA = Dense low-silica andesite; LSAS = low-silica andesite scoria; HSA = high-silica andesite; ISA = intermediate-silica andesite; QMI = quenched mafic inclusion.

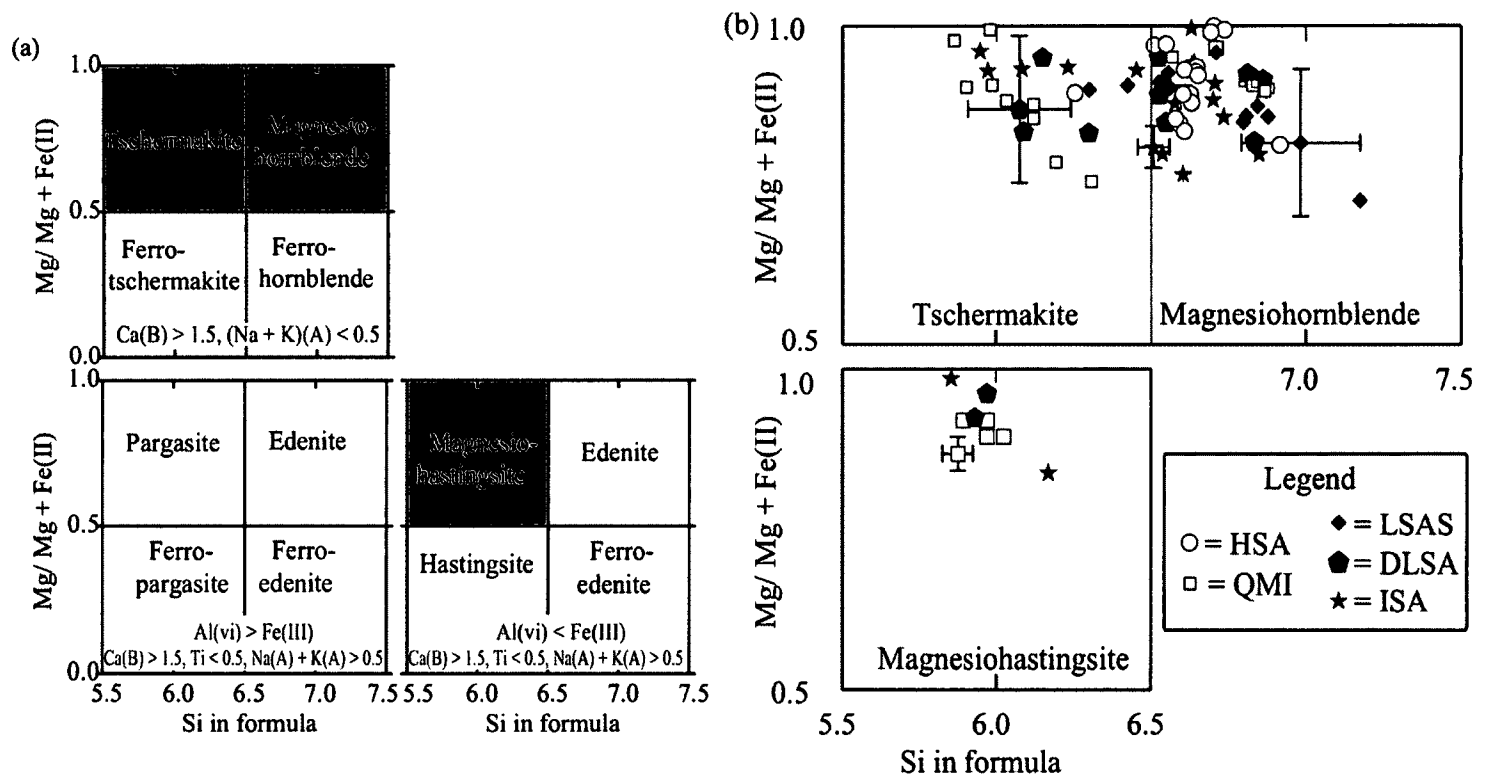


Figure 1.6 Amphibole classification. Plot (a) shows the full Leake et al. (1997) classification scheme for calcic amphiboles. Grey shading in (a) indicates the fields in which Augustine amphiboles are found. These fields are expanded in (b). Amphiboles are categorised by lithology. Representative uncertainties are provided on four data points. DLSA = Dense low-silica andesite; LSAS = low-silica andesite scoria; HSA = high-silica andesite; ISA = intermediate-silica andesite; QMI = quenched mafic inclusion

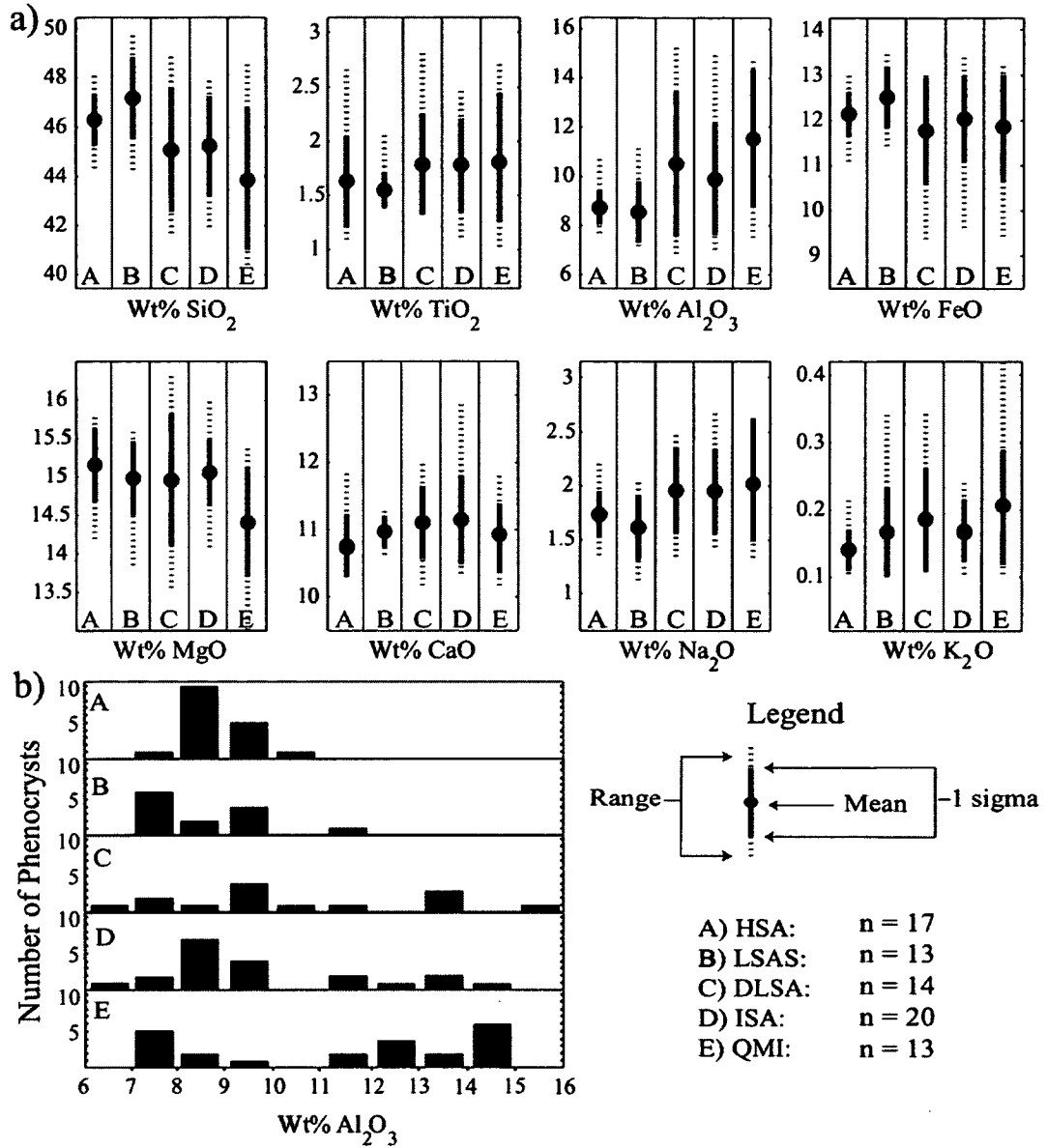


Figure 1.7 Compositions and modes of amphibole. The plots in (a) show the mean, range, and 1 sigma standard deviation of major oxide composition of amphibole phenocrysts in each lithology. Individual plots denote different major oxides, while columns within denote lithologies. The number of amphiboles represented in each lithology is denoted by 'n', as listed in the legend. Plot (b) histograms show how different compositions of phenocrysts are distributed within each lithology (on the basis of Al₂O₃).

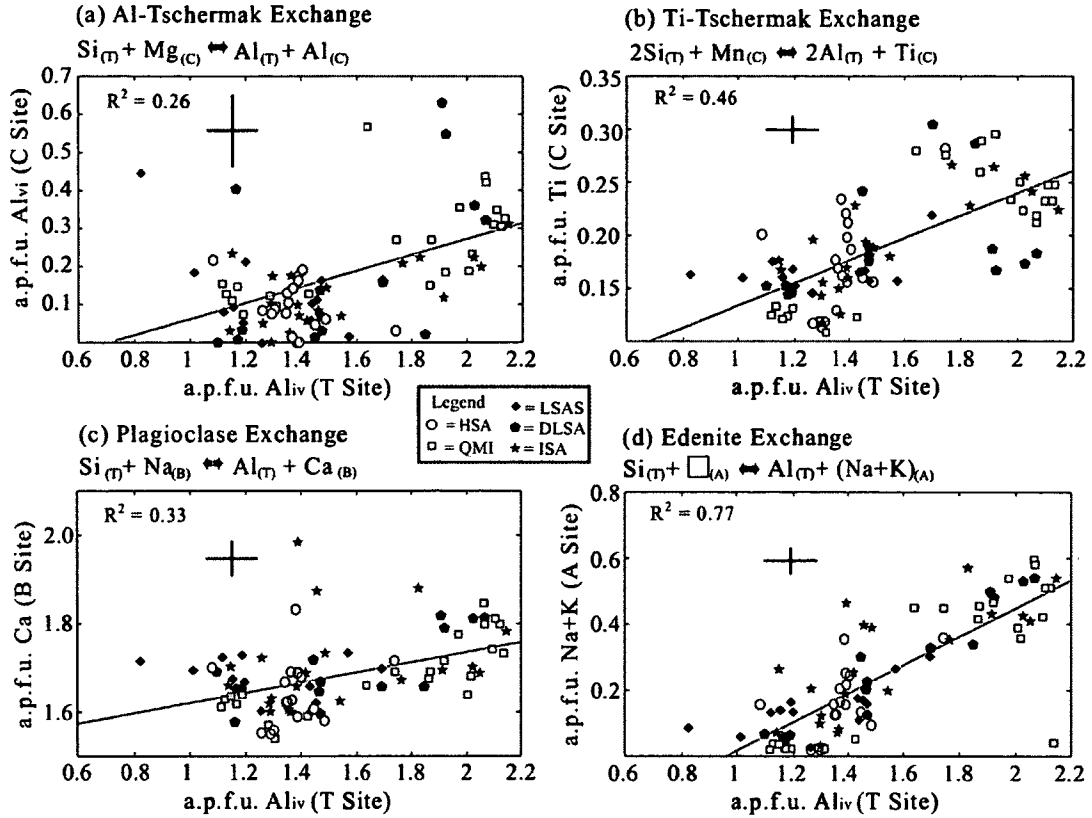


Figure 1.8 Temperature- and pressure-sensitive coupled-substitutions. (a) represents the pressure-sensitive Al-Tschermak substitutions; (b) represents the temperature-sensitive Ti-Tschermak exchange; (c) represents the temperature-sensitive plagioclase exchange; (d) represents the temperature-sensitive edenite exchange. Best-fit lines are indicated on each panel. Crosshairs on each plot indicate the mean standard deviation around cation data. Cation uncertainties were calculated by propagating the standard deviation on major oxide data through the mineral recalculation and site assignment procedures (Giaramita & Day, 1990; De Angelis & Neill, 2012). Data points are categorised by lithology: DLSA = Dense low-silica andesite; LSAS = low-silica andesite scoria; HSA = high-silica andesite; ISA = intermediate-silica andesite; QMI = quenched mafic inclusion. A.p.f.u. = atoms per formula unit.

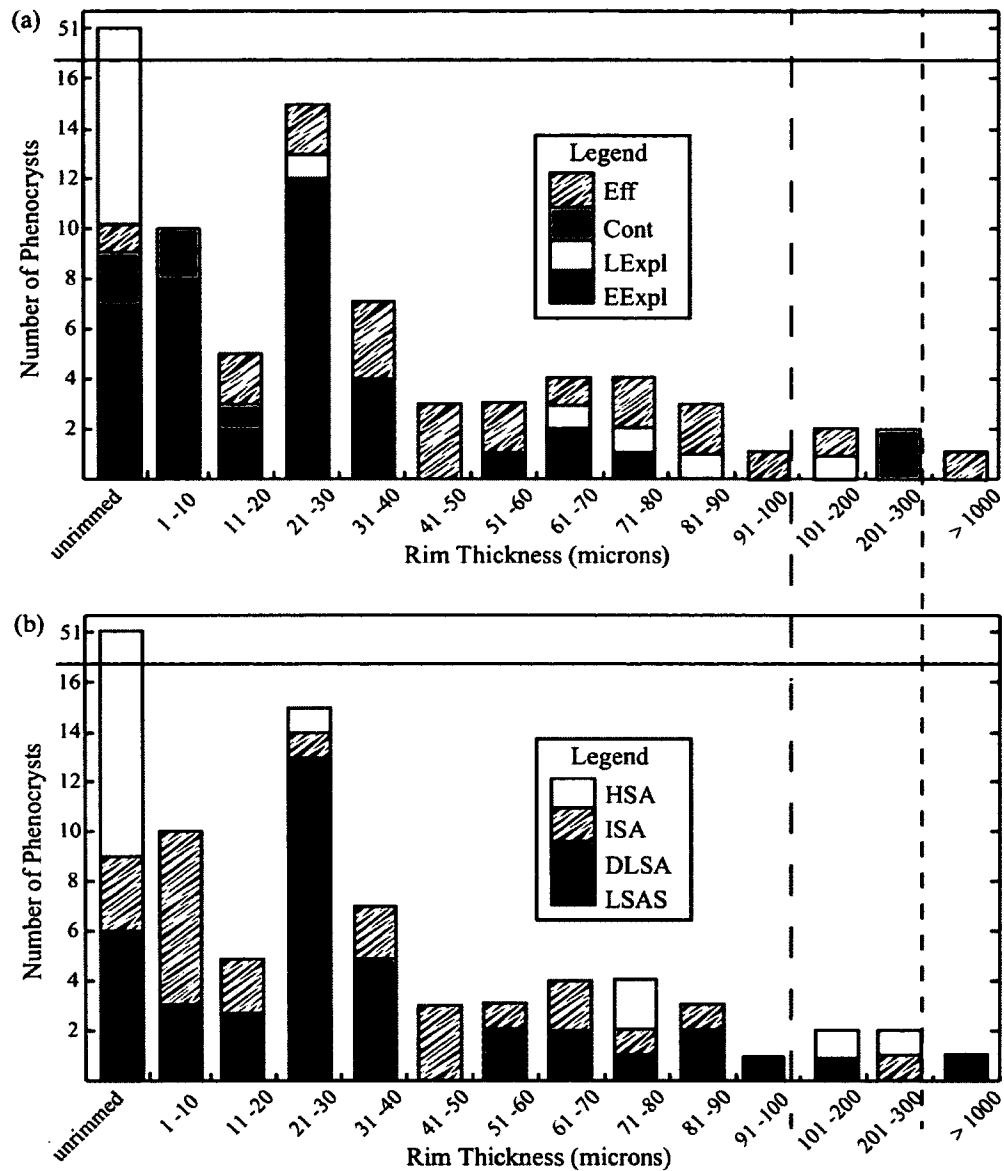


Figure 1.9 Distribution of amphibole rim thicknesses. The histogram in plot (a) shows variations in reaction rim thickness through the eruption progression. The solid horizontal line (at frequency = 16) represents a discontinuous Y-axis. The order in which phases are plotted in the unrimmed bin is different from the other bins. This allows the late explosive phase to be plotted at the top of the bin, corresponding with the change in axis. The first vertical dashed line on the histogram indicates a change in bin size. The second vertical dashed line indicates both a discontinuous x-axis and a change in bin size. Plot (b) shows the same data set, classified by lithology.

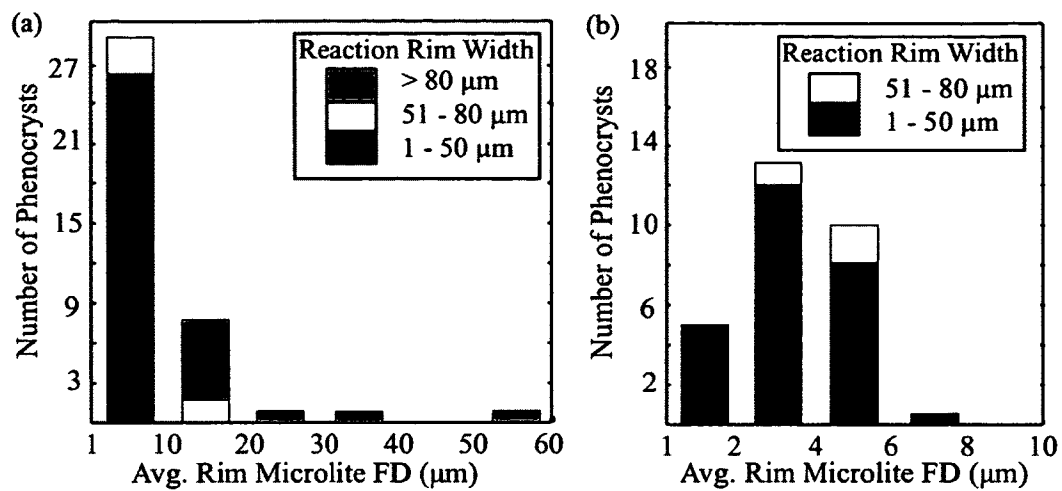


Figure 1.10 Histogram of reaction rim microlite sizes. Plot (a) shows the entire data set. In plot (b), data from the 1-10 μm bin is further subdivided. Feret's Diameter (FD) is the longest distance between any two points around the boundary of the crystal, as defined by ImageJ.

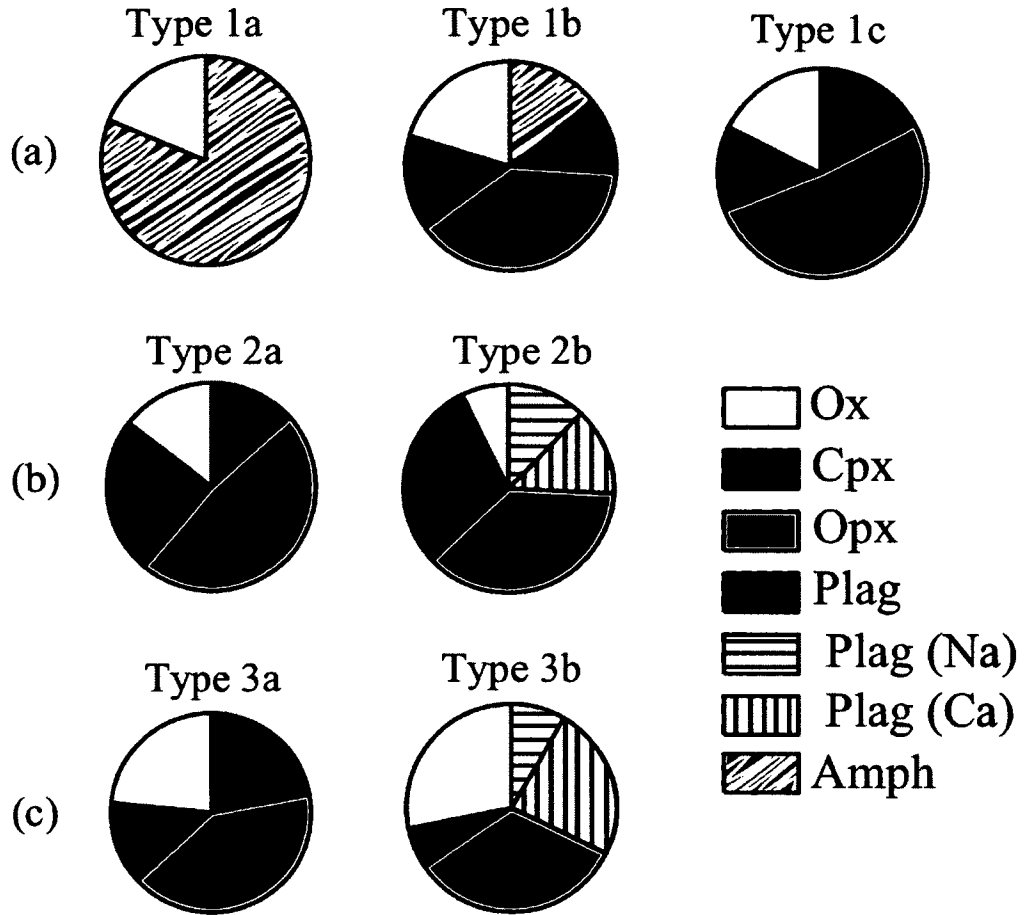


Figure 1.11 The distribution of mineral phases within reaction rim types. Row (a) shows Type 1 reaction rim data, row (b) shows Type 2 reaction rim data, and row (c) shows Type 3 reaction rim data. Ox = oxides; Cpx = clinopyroxene; Opx = orthopyroxene; Plag = plagioclase; Amph = amphibole. Type 1, 2a, and 2b contain single population of plagioclase crystals of uniform composition (dark grey). Type 2b and 3b contain two plagioclase populations, one more sodic (horizontal lines) and one more calcic (vertical lines).

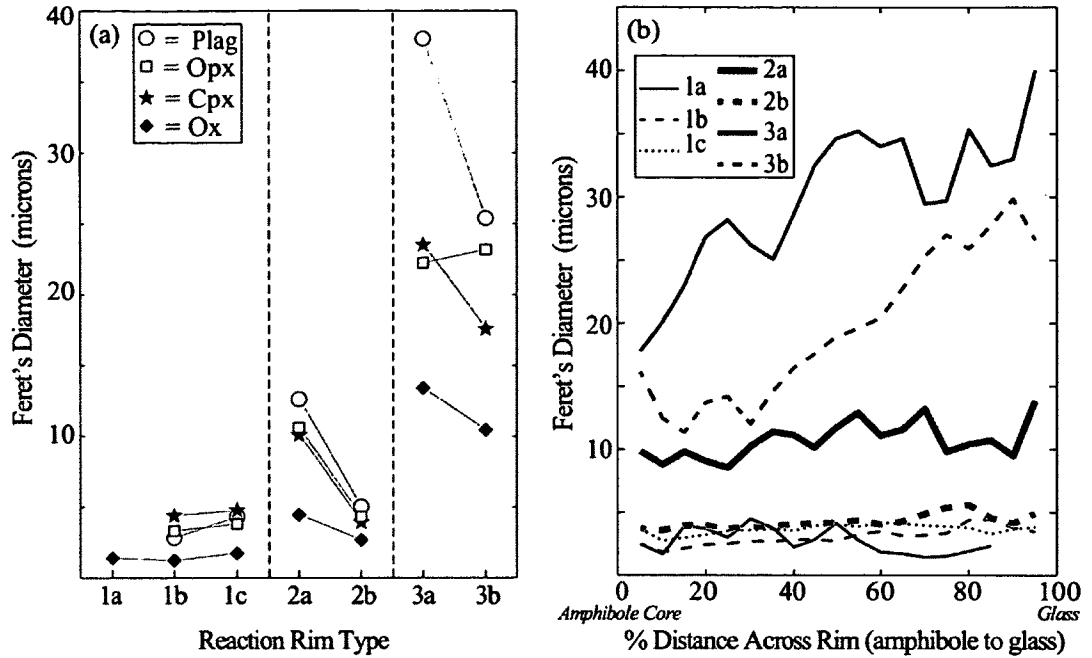


Figure 1.12 Variations in rim microlite sizes. Plot (a) shows the mean sizes of reaction rim microlites from each identified phase within the rim. The sizes of amphibole fragments found in Type 1 rims are not shown. Ox = oxides; Cpx = clinopyroxene; Opx = orthopyroxene; Plag = plagioclase. Plot (b) shows changes in the mean reaction rim microlite size (all phases included) across amphibole reaction rims, for each rim Type. The x-axis represents the distance from the amphibole-reaction rim boundary (0% distance across rim) to the reaction rim-glass boundary (100% distance across rim). Data are presented as overlapping simple moving averages and represent mean microlite sizes within the previous and subsequent 5% distance across the rim.

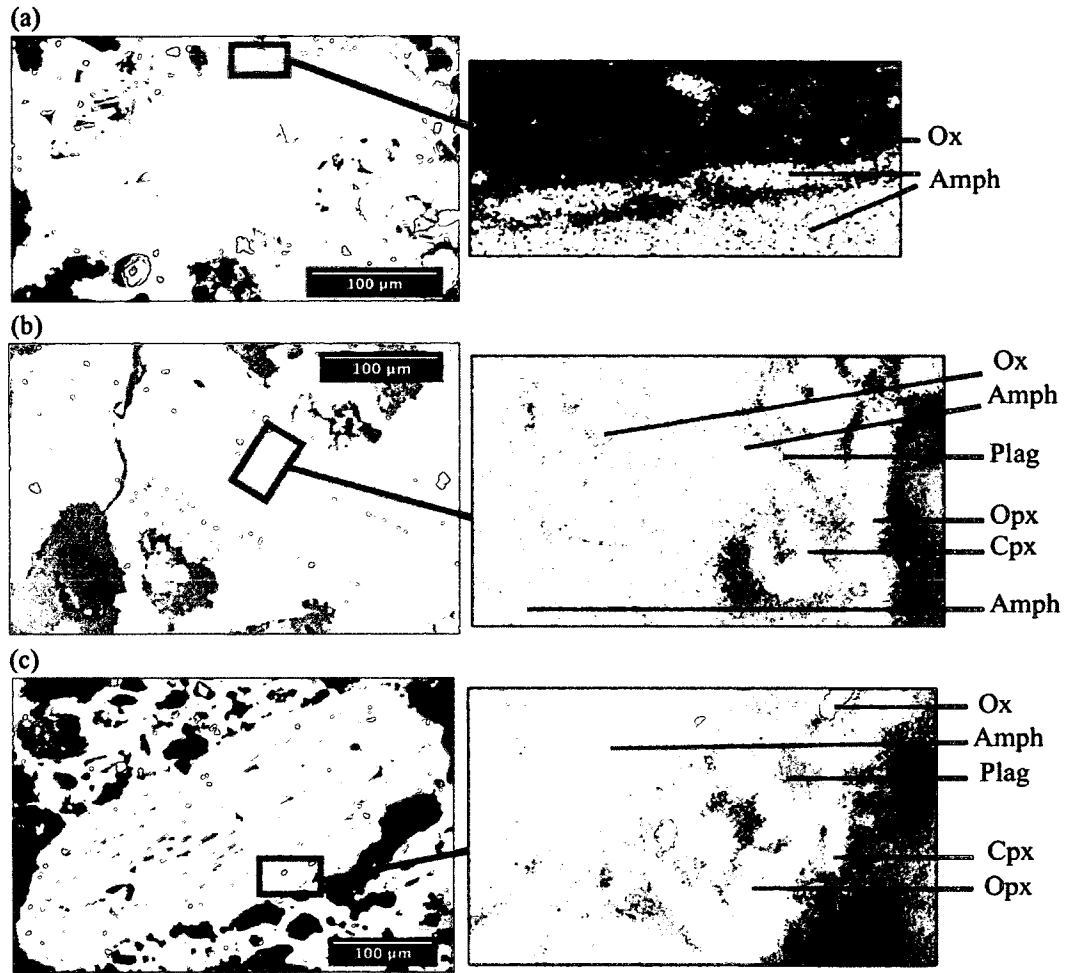


Figure 1.13 Type 1 reaction rim BSE images and composite X-ray maps. (a) Type 1a; (b) Type 1b; (c) Type 1c. X-ray map areas are denoted on BSE images by black boxes. Different colours on X-ray maps denote different mineral phases (note that exact hue varies between X-ray maps). Light green = amphibole, bright green = orthopyroxene, bright yellow/ red = Fe-Ti oxides, orange = clinopyroxene, blue/purple = plagioclase.

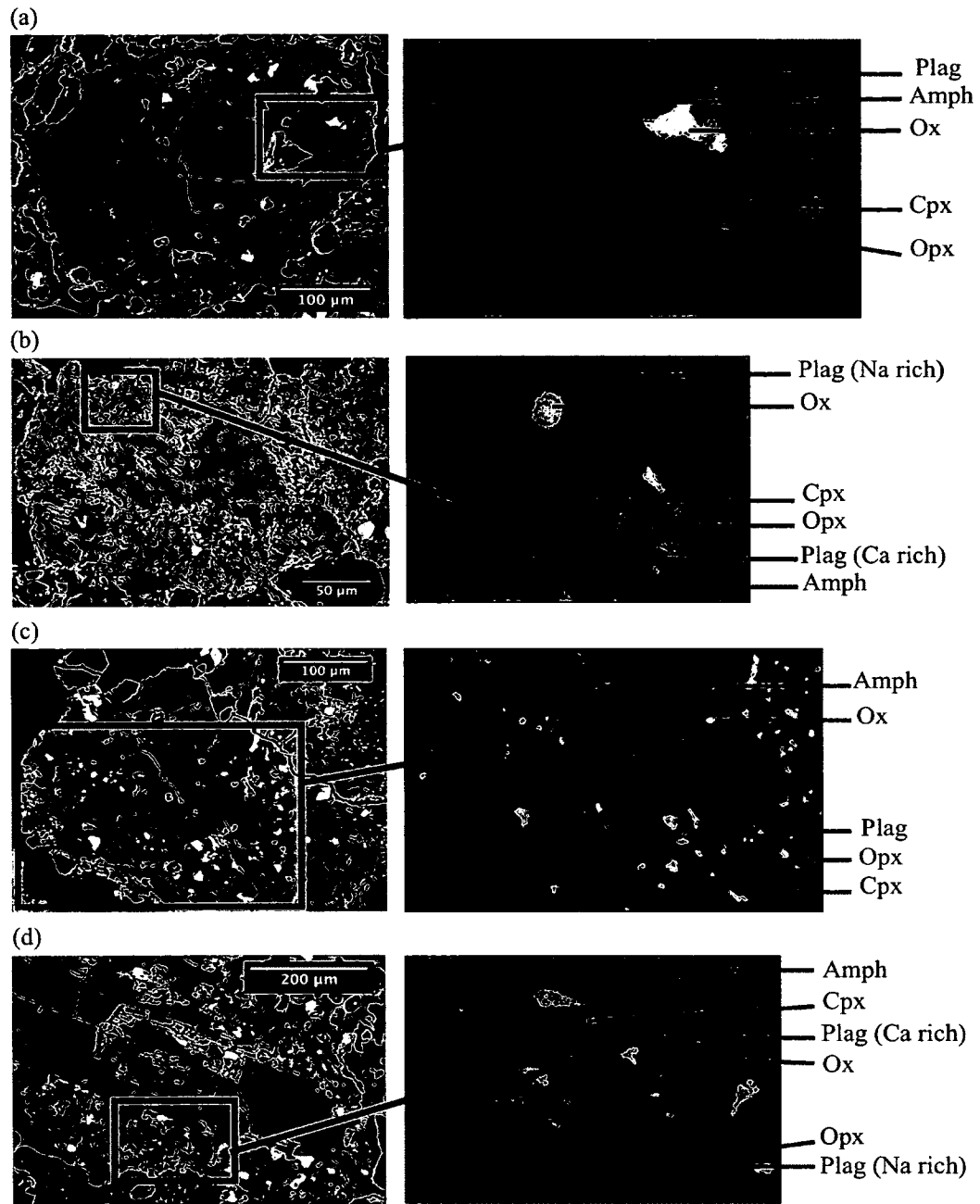
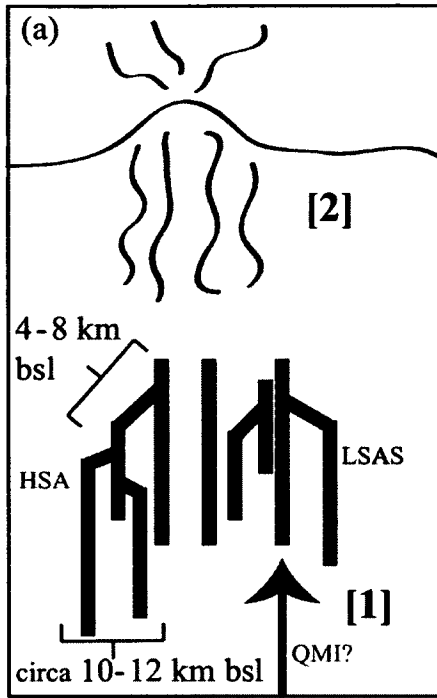
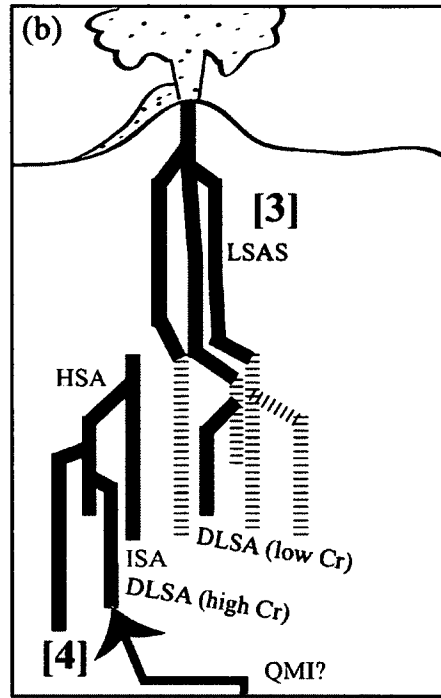


Figure 1.14 Type 2 and 3 reaction rim BSE images and composite X-ray maps. (a) Type 2a; (b) Type 2b; (c) Type 3a; (d) Type 3b. X-ray map areas are denoted on BSE images by black boxes. Different colours on X-ray maps denote different mineral phases (exact hue varies between X-ray maps). Light green = amphibole, bright green = orthopyroxene, bright white = magnetite, bright yellow = ilmenite, orange = clinopyroxene, blue/purple = plagioclase.

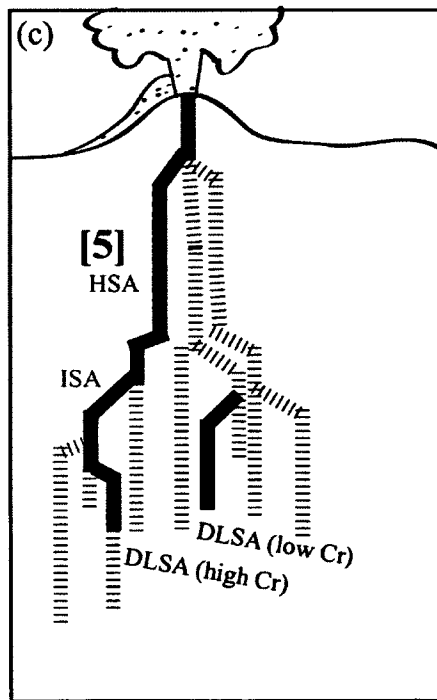
Figure 1.15 Schematic depiction of the proposed model for the 2006 eruption. (a) During the precursory phase (May 2005–January 2006) fresh magma underplates the shallow storage system [1]. The shallow storage region was comprised of interconnecting dikes containing remnant magmas, including high- (grey) and low-silica andesites (black). The top of this shallow storage region was between 4-8 km bsl. The intruded magma heated the low-silica andesite leading to the release of volatiles [2]; (b) Heated low-silica andesite rose buoyantly to the surface and was erupted as low-silica andesite scoria during the early explosive phase [3]. The intruding magma mingled with some of the resident high-silica andesite to form hybrid andesites [4], intermediate-silica andesite (green) and a dense low-silica andesite (black); (c) The near exhaustion of heated low-silica andesite caused the draw up of high- and intermediate-silica andesites into the now open conduit [5], during the late explosive and continuous phases; (d) During the effusive phase two compositionally similar degassed low-silica magmas erupted together [6]. One of these degassed low-silica magmas represented the final remnants of the low-silica andesite and the other a high-silica andesite-quenched mafic inclusion hybrid. On eruption they formed two lava flows and a final lava dome.



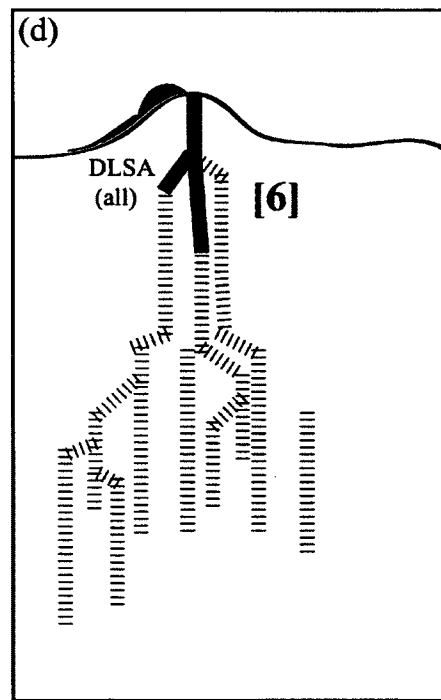
Precursory Phase
May 2005 - Jan 2006



Early Explosive Phase
Jan 13 - Jan 17



Late Explosive/ Continuous Phase
Jan 17 - Feb 4



Effusive Phase
Feb 4 - late Mar 2006

1.11 TABLES

Table 1.1: Augustine 2006 eruptive phases and lithologies

Eruptive Phase^a	Acronym	Description
Precursory	N/A	April 2005 – January 2006: increased Seismicity, deformation, and phreatic activity
Explosive (early/late)	Expl (EExpl/LExpl)	13-27 January 2006 (13-17/ 18-27): Discrete vulcanian explosions, pyroclastic flows, and lahars
Continuous	Cont	28 January - 4 February 2006: Growth and destruction of ephemeral summit lava domes, pyroclastic and block-and-ash flows
Effusive	Eff	4 February - late March 2006: Emplacement of two lava flows and a summit dome (which remains in place)
Lithology^b		
High-silica andesite	HSA	SiO ₂ wt%:62.2–63.3
Low-silica andesite scoria	LSAS	SiO ₂ wt%:56.5–58.7
Dense low-silica andesite	DLSA	SiO ₂ wt%:56.4–59.3
Intermediate-silica andesite	ISA	SiO ₂ wt%:58.3-62.2
Quenched mafic inclusions	QMI	SiO ₂ wt%:49.7–60.6

^aCoombs et al., 2010

^bLarsen et al., 2010

Table 1.2: Sample inventory for Augustine 2006 amphiboles

Sample ^a	Lithology ^b	Phase ^c	Deposit Date (2006)	Amphibole Count ^d
06AUMRT037a	DLSA	EExpl	Jan 13-14	16
06AUMRT037c	LSAS	EExpl	Jan 13-14	3
06AUMRT037e	ISA	EExpl	Jan 13-14	8
06AUMC005cp2	HSA	EExpl	Jan 13-14	1
06AUMC008bp1	LSAS	EExpl	Jan 13-14	4
06AUMC008bp1-2	LSAS	EExpl	Jan 13-14	1
06AUMC008bp1a	LSAS	EExpl	Jan 13-14	5
06AUMC007c	LSAS	EExpl	Jan 17	3
06AUMRT006A	ISA	EExpl	Jan 17	1
06AUMLC259e	DLSA	LExpl	Jan 27	2
06AUMC004a	HSA	LExpl	Jan 27	2
06AUMC004cp1	HSA	LExpl	Jan 27	1
06AUMC004C.c2	HSA	LExpl	Jan 27	1
06AUMC004c	HSA	LExpl	Jan 27	39 ^e
06AUMC004c1	HSA	LExpl	Jan 27	2
06AUSH002	QMI	LExpl	Jan 27	4
06AUSH001	QMI	Cont	Jan 28-Feb 4	13
06AUSH014a	QMI	Cont	Jan 28-Feb 4	5
06AUMC009.LI	ISA	Cont	Jan 28-Feb 4	4
06AUMC009p1	HSA	Cont	Jan 28-Feb 4	1
06AUMC010.p1	HSA	Cont	Jan 28-Feb 4	1
06AUMRT017a	ISA	Cont	Jan 28-Feb 4	2
06AUMLC057	DLSA	Eff	Mar 3-16	3
06AUJFL001b	ISA	Eff	Mar 3	2
06AUKB002a	ISA	Eff	Mar 3	2
06AUKB002B	ISA	Eff	Mar 3	1
06AUKB002c	ISA	Eff	Mar 3	6
06AUKB003	DLSA	Eff	Mar 3	3
06AUMC012	DLSA	Eff	Mar 3	2
06AUMRT032B	ISA	Eff	Mar 3	3
06AUMRT032c	LSAS	Eff	Mar 3	4

^aSample names from Coombs et al. (2010), except QMI samples (collected by author)

^bDLSA = Dense low-silica andesite; LSAS = low-silica andesite scoria; HSA = high-silica andesite; ISA = intermediate-silica andesite; QMI = quenched mafic inclusion

^cEExpl = early explosive; LExpl = late explosive; Cont = continuous; Eff = effusive

^dNumber of amphibole per samples. In some cases samples were represented by more than one thin section

^eApproximately 30 additional MC004c grains were not assigned grain IDs

Table 1.3: Representative amphibole compositions*

Sample^a	MRT017a	MLC057	MC004c	MRT037c	SH001
	Grain 1	Grain 3	Grain 1	Grain 1	Grain 1
Lithology	ISA	DLSA	HSA	LSAS	QMI
Phase	Cont	Eff	LExpl	EExpl	LExpl
Class^b	Tsch	Mghast	Mghbl	Mghbl	Tsch
SiO₂	42.43(0.58 ^e)	42.07(0.78)	46.65(0.52)	46.23(1.27)	42.07(0.53)
TiO₂	2.30(0.06)	1.63(0.07)	1.57(0.27)	1.53(0.07)	2.09(0.14)
Al₂O₃	13.63(0.35)	14.29(0.36)	8.71(0.36)	8.96(0.27)	13.45(0.42)
FeO(t)	11.94(0.39)	9.38(0.35)	11.93(0.42)	13.16(0.28)	11.12(0.48)
MnO	0.17(0.06)	0.10(0.04)	0.48(0.09)	0.34(0.04)	0.10(0.02)
MgO	15.02(0.23)	15.79(0.86)	15.31(0.33)	14.99(0.27)	15.15(0.13)
CaO	11.24(0.33)	11.92(0.21)	10.64(0.18)	10.90(0.10)	11.04(0.18)
Na₂O	2.50(0.05)	2.46(0.14)	1.74(0.10)	1.80(0.03)	2.32(0.05)
K₂O	0.23(0.23)	0.22(0.01)	0.13(0.03)	0.13(0.03)	0.21(0.02)
Total	99.47	97.85	97.16	98.05	97.55
n	3	4	9	4	3
Si (T^d)	5.95(0.08 ^e)	5.97(0.15)	6.64(0.06)	6.56(0.08)	5.98(0.03)
Al(iv) (T)	2.05(0.08)	2.03(0.15)	1.36(0.06)	1.44(0.08)	2.02(0.03)
Al(vi) (C)	0.20(0.03)	0.36(0.21)	0.10(0.08)	0.06(0.11)	0.23(0.08)
Fe³⁺ (C)	1.27(0.09)	0.98(0.41)	1.17(0.12)	1.22(0.14)	1.30(0.11)
Ti (C)	0.24(0.01)	0.17(0.01)	0.17(0.03)	0.16(0.01)	0.22(0.02)
Mg (C)	3.14(0.05)	3.34(0.17)	3.25(0.07)	3.17(0.10)	3.21(0.03)
Fe²⁺ (C)	0.13(0.05)	0.13(0.42)	0.25(0.12)	0.34(0.14)	0.02(0.07)
Mn (C)	0.02(0.01)	0.01(0.00)	0.06(0.01)	0.04(0.00)	0.01(0.00)
Ca (B)	1.69(0.05)	1.81(0.02)	1.62(0.03)	1.66(0.03)	1.68(0.01)
Na (B)	0.31(0.05)	0.19(0.02)	0.38 (0.03)	0.34(0.03)	0.32(0.01)
Na (A)	0.37(0.04)	0.49(0.05)	0.10(0.05)	0.15(0.04)	0.32(0.02)
K (A)	0.04(0.01)	0.04(0.00)	0.02(0.00)	0.02(0.00)	0.04(0.00)

* Full data available in the Appendix 1.1.

^a"06AU" removed from sample names for the sake of brevity

^bAmphibole classification abbreviations: Tsch = tschermakite, Mghbl = magnesio-hornblende, Mghast = magnesio-hasting

^c1 sigma uncertainty on 'n' analyses

^dLetters denote site in amphibole structure

^e1 sigma uncertainty on 'n' analyses propagated through mineral recalculation using the method of Giaramita & Day (1990)

Table 1.4: Representative amphibole rim analyses*

Sample ^b	Lith.	Phase	Type	Rim Width (mm)	FD (mm) ^c	CND (mm ⁻²) ^d	Mineralogy ^e
JFL001b Grain 1	ISA	Eff	1a	20 (12) ^a	4.73 (3.27)	94.5k (58k)	amph (66.7), ox (33.3)
MRT037e Grain 5	ISA	EExpl	1b	8 (3)	2.51 (1.04)	206k (14k)	amph (8.5), opx (62.0), cpx (7.0), ox (7.0), plag (15.5)
MRT037a Grain 1	DLSA	EExpl	1c	30 (7)	3.45 (1.26)	93.0k (15k)	Px (70.5), ox (13.1), plag (16.4)
MRT037e Grain 4	ISA	EExpl	1c	7 (2)	2.14 (0.87)	343k (24k)	Opx (77.4), cpx (8.1), plag (14.5)
MRT037e Grain 1	ISA	EExpl	2a	63 (10)	16.2 (13.7)	10.7k (4.7k)	Opx (60.4), cpx (27.1), ox (7.3), plag (5.2)
004C Grain 2	HSA	LExpl	3a	179 (38)	31.6 (21.7)	2.5k (0.8k)	Opx (50.7), cpx (28.5), ox (11.8), plag (9.0)

* Full data available in the Appendices 1.2 and 1.3.

^aNumbers in brackets represent standard deviation

^b"06AU" removed from sample names for the sake of brevity

^cAverage Feret's Diameter (FD) of all analyzed rim microlites.

^dAverage crystal number density (per mm²) in thousands (e.g. 94.5k = 94,500). Derived from 5 individual calculations of CND per rim.

^eAmph = amphibole; opx = orthopyroxene; cpx = clinopyroxene; ox = Fe-Ti oxides; plag = plagioclase; px = pyroxene (undifferentiated). Values in brackets indicate % out all identified microlites.

1.12 REFERENCES

- Adam, J., Oberti, R., Camara, F. & Green, T. H. (2007). An electron microprobe, LAM-ICP-MS and single crystal X-ray structure refinement study of the effects of pressure, melt- H₂O concentrations and fO₂ on experimentally produced amphiboles, *European Journal of Mineralogy* **19**, 641-655.
- Al'meev, R. R., Ariskin, A. A., Ozerov, A. Y. & Kononkova, N. N. (2002). Problems of the stoichiometry and thermobarometry of magmatic amphiboles: An example of hornblende from the andesites of Bezymyanni Volcano, Eastern Kamchatka, *Geochemistry International* **40**(8), 723-738.
- Bachmann, O. & Dungan, M. A. (2002). Temperature-induced Al-zoning in hornblendes of the Fish Canyon magma, Colorado. *American Mineralogist* **87**, 1062–1076.
- Bacon, C. R. (1986). Magmatic inclusions in silicic and intermediate volcanic rocks. *Journal of Geophysical Research* **91**, 6091–6112
- Browne, B. L. (2005). Petrologic and experimental constraints on magma mingling and ascent; examples from Japan and Alaska. PhD. Thesis, University of Alaska Fairbanks.
- Browne, B. L. & Gardner, J. E. (2006). The influence of magma ascent path on the texture, mineralogy, and formation of hornblende reaction rims. *Earth and Planetary Science Letters* **246** (3–4), 161–176.
- Browne, B. L. & Vitale, M. (2011). Formation and significance of magmatic enclaves from the 2006 eruption of Augustine Volcano, Alaska, *AGU Fall Meeting Abstract* **V41F-05**.

Brugger, C. R. & Hammer, J. E. (2010). Crystallization kinetics in continuous decompression experiments: Implications for interpreting natural magma ascent processes. *Journal of Petrology* **51**(9), 1941–1965.

Buckley, V. J. E., Sparks, R. S. J., & Wood, B. J. (2006). Hornblende dehydration reactions during magma ascent at Soufrière Hills Volcano, Montserrat. *Contributions to Mineralogy and Petrology* **151**(2), 121–140.

Cervelli, P., Fournier, T., Freymueller, J., and Power, J., Lisowski, M. & Pauk, B. A. (2010). Geodetic Constraints on Magma Movement and Withdrawal during the 2006 Eruption of Augustine Volcano. In: Power, J. A., Coombs, M. L. & Freymueller, J. T. (eds) The 2006 eruption of Augustine Volcano, Alaska. *USGS Professional Paper 1769*, 427–452.

Coombs, M., Bull, K., Vallance, J., Schneider, D., Thoms, E., Wessels, R. & McGimsey, R. (2010). Timing, distribution, and volume of proximal products of the 2006 eruption of Augustine Volcano, Alaska, in Power, J. A., Coombs, M. L. & Freymueller, J. T. eds, The 2006 eruption of Augustine Volcano, Alaska. *USGS Professional Paper 1769*, 145–185.

Coombs, M., Sisson, T., Bleick, H., Henton S., Nye, C., Payne, A., Cameron, C., Larsen, J., Wallace, K., & Bull, K. (2012). Andesites of the 2009 eruption of Redoubt Volcano, Alaska, *Journal of Volcanology and Geothermal Research*, Special Issue on the 2009 Redoubt Eruption, In Press.

Coombs, M.L. & Vazquez, J. (2012). Augustine Volcano's Pleistocene rhyolite and its modern-day residuum, *AGU Fall Meeting Abstract* V43D-2890.

De Angelis, S. H. & Neill, O. K. (2012). MINERAL: A program for the propagation of analytical uncertainty through mineral formula recalculations. *Computers and Geosciences*, doi:10.1016/j.cageo.2012.05.023

Devine, J. D., Rutherford, M. J. & Gardner, J. E. (1998). Petrologic determination of ascent rates for the 1995–1997 Soufrière Hills Volcano andesite magma. *Geophysical Research Letters* **25**(19), 3673–3676.

Ernst, W. G. & Liu, J. (1998). Experimental phase-equilibrium study of Al- and Ti- contents of calcic amphibole in MORB- A semiquantitative thermobarometer, *American Mineralogist* **83**, 952-969

Foley, F. V., Pearson, N. J., Rushmer, T., Turner, S., & Adam, J. (2012). Magmatic Evolution and Magma Mixing of Quaternary Adakites at Solander and Little Solander Island, New Zealand. *Journal of Petrology*, doi: 10.1093/petrology/egs082.

Garcia, M. O. & Jacobson, S. S. (1979). Crystal clots, amphibole fractionation and the evolution of calc-alkaline magmas, *Contributions to Mineralogy and Petrology* **69**, 319–327.

Giaramita, M. & Day, H. (1990). Error propagation in calculations of structural formulas. *American Mineralogist* **75**, 170–182.

Gill, J. B. (1981) *Orogenic andesites and plate tectonics*. Springer-Verlag, Berlin, 370 p.

Hammarstrom, J. M. & Zen, E. (1986). Aluminum in hornblende: An empirical igneous geobarometer. *American Mineralogist* **71**, 1297-1313.

Hammer, J. E. (2008). Experimental Studies of the Kinetics and Energetics of Magma Crystallization. *Reviews in Mineralogy & Geochemistry* **69**, 9–59.

Hammer, J. E. & Rutherford, M. J. (2002). An experimental study of the kinetics of decompression-induced crystallization in silicic melt. *Journal of Geophysical Research* **107**(B1, 2021), 10.1029/2001JB000281.

Johnson, M. & Rutherford, M. (1989). Experimental calibration of the aluminum-in-hornblende geobarometer with application to Long Valley Caldera (California) volcanic rocks. *Geology* **17**, 837–841.

Johnston, D. (1978). Volatiles, magma mixing, and the mechanism of eruptions at Augustine Volcano, Alaska. Ph.D. Thesis, University of Washington.

Larsen, J., Nye, C., Coombs, M., Tilman, M., Izbekov, P. & Cameron, C. (2010). Petrology and geochemistry of the 2006 eruption of Augustine Volcano. In: Power, J. A., Coombs, M. L. & Freymueller, J. T. (eds) *The 2006 eruption of Augustine Volcano, Alaska. USGS Professional Paper 1769*, 335–382.

Leake, B., Woolley, A., Arps, C., Birch, W., Gilbert, C., Grice, J., Hawthorne, F., Kisch, H., Kato, A., Krivovichev, V., Laird, J., Linthout, K., Mandarino, J., Maresch, W., Nickel, E., Rock, N., Schumacher, J., Smith, D., Stephenson, N., Ungaretti, L., Whittaker, E. & Youzhi, G. (1997). Nomenclature of amphiboles: Report of the Subcommittee on Amphiboles of the International Mineralogical Association's Commission on New Minerals and Mineral Names. *Canadian Mineralogist* **35**, 219–246.

Muncill, G. E., & Lasaga, A. C. (1988). Crystal-growth kinetics of plagioclase in igneous systems: Isothermal H₂O-saturated experiments and extension of a growth model to complex silicate melts, *American Mineralogist* **73**, 982-992.

Murphy, M. D., Sparks R. S. J., Barclay, J., Carroll, M. R. & Brewer, T. S. (2000). Remobilization of andesite by intrusion of mafic magma at the Soufrière Hills Volcano, Montserrat, West Indies, *Journal of Petrology* **41**(1), 22–42.

Plechov, P., Tsai, A., Shcherbakov, V. & Dirksen, O. (2008). Opacitization conditions of hornblende in Bezymyanni volcano andesites (March 30, 1956 eruption). *Petrology* **16**(1), 19–35.

Power, J. A., Coombs, M. L. & Freymueller, J. T. (eds) (2010). *The 2006 eruption of Augustine Volcano, Alaska. USGS Professional Paper 1769.*

Ridolfi, F., Renzulli, A. & Puerini, M. (2010). Stability and chemical equilibrium of amphibole in calc-alkaline magmas: an overview, new thermobarometric formulations and application to subduction-related volcanoes. *Contributions to Mineralogy and Petrology* **160**(1), 45–66.

Roman, D. C., Cashman, K. V., Gardner, C. A., Wallace, P. J. & Donovan, J. J. (2006). Storage and interaction of compositionally heterogeneous magmas from the 1986 eruption of Augustine Volcano, Alaska. *Bulletin of Volcanology* **68**(3), 240–254.

Rutherford, M. (2008). Magma ascent rates. *Reviews in Mineralogy & Geochemistry* **69**, 241–271.

Rutherford, M. & Devine, J. (2003). Magmatic conditions and magma ascent as indicated by hornblende phase equilibria and reactions in the 1995–2002 Soufrière Hills magma. *Journal of Petrology* **44**(8), 1433–1454.

Rutherford, M. & Hill, P. (1993). Magma ascent rates from amphibole breakdown: An experimental study applied to the 1980–1986 Mount St. Helens Eruptions. *Journal of Geophysical Research* **98**(B11), 19,667–19,685.

Shane, P. & Smith, V. C. (2013). Using amphibole crystals to reconstruct magma storage temperatures and pressures for the post-caldera collapse volcanism at Okataina volcano. *Lithos*, <http://dx.doi.org/10.1016/j.lithos.2012.11.008>

Steiner, A.K., Browne, B.L. & Nye, C. (2012). Quenched mafic inclusions in ≤ 2200 years B.P. deposits at Augustine Volcano, Alaska. *International Geology Review* **54**(11), 1241–1270.

Thompson, J. A. (2011). Uranium series analysis of 2006 Augustine volcanics: An investigation into the timescales of magmatic processes. M.S. Thesis, The University of Iowa.

Vallance, J. W., Bull, K. F., & Coombs, M. L. (2010). Pyroclastic flows, lahars, and mixed avalanches generated during the 2006 eruption of Augustine Volcano. In: Power, J. A., Coombs, M. L. & Freymueller, J. T. (eds) *The 2006 eruption of Augustine Volcano, Alaska. USGS Professional Paper 1769*, 219–268.

Vitale, M. (2012). Petrology and mineral inventory of basalt inclusions from the 2006 eruption of Augustine Volcano, Alaska. M.S. Thesis, California State University, Fullerton.

Waitt, R. & Begét, J. (2009). Volcanic Processes and Geology of Augustine Volcano, Alaska. *USGS Professional Paper 1762*, 78 p.

Waythomas, C. F., & Waitt, R. B. (1998). Preliminary volcano-hazard assessment for Augustine Volcano, Alaska. *U.S.G.S Open-File Report 98-0106*, 39 p., 1 plate.

Webster, J., Mandeville, C., Goldoff, B., Coombs, M., & Tappen, C. (2010). Augustine Volcano— The influence of volatile components in magmas erupted A.D. 2006 to 2,100 years before present. In: Power, J. A., Coombs, M. L. & Freymueller, J. T. (eds) *The 2006 eruption of Augustine Volcano, Alaska. USGS Professional Paper 1769*, 385–423.

CHAPTER 2:

Experimental constraints on magmatic storage conditions for the high-silica andesite of the 2006 eruption of Augustine Volcano, Alaska²

2.1 ABSTRACT

New data from phase equilibria experiments refine the model for crystal-rich high-silica andesite ($\text{SiO}_2 = 62.5$) storage prior to the 2006 eruption of Augustine Volcano, Alaska. Experiments were conducted under H_2O saturated conditions, $f_{\text{O}_2} = \text{Re-ReO}_2$ ($\sim\text{Ni-NiO}+2$), with pressures 50–200 MPa ($P_{\text{Total}} = P_{\text{H}_2\text{O}}$) and temperatures 800–1060°C. Run durations varied from 23 to 539 hours depending on the experimental conditions. Starting powders were prepared as follows: 1) finely ground natural powders; 2) twice-sintered and ground glass; or 3) twice sintered, ground glass seeded with plagioclase and amphibole. The natural phase assemblage (plagioclase, 2 pyroxenes, Fe-Ti oxides, and amphibole) was reproduced between 860–880°C and 120–200 MPa. Maximum storage temperature is restricted by amphibole instability above 880°C. Minimum storage temperature is constrained by quartz stability at temperatures up to 850°C (at ~ 140 MPa). Minimum storage pressures are confined by amphibole instability below 120 MPa. Experimental plagioclase An contents ($\sim\text{An } 55\text{--}60$) and groundmass glass compositions ($\text{SiO}_2 = 79.86 \pm 0.64$) most closely replicate natural samples in experiments conducted at $\sim 130\text{--}150$ MPa, equivalent to depths of 5–6 km assuming a crustal density of 2650 kg/m³. Estimated storage pressures and temperatures fall within the ranges suggested by natural petrological data (e.g. melt inclusions, Fe-Ti oxide touching pairs) and agree with modeled storage depths from geodetic data. The high temperature stability of quartz and biotite (not identified in natural Augustine high-silica andesites) could be explained by the relatively high f_{O_2} of the Augustine system as well as the rapid kinetics associated with the crystal-poor

² Henton De Angelis, S., Larsen, J. & Coombs, M. & Dunn, A. Experimental constraints on magmatic storage conditions at Augustine Volcano, Alaska. Prepared for submission to *Contributions to Mineralogy and Petrology*

sintered starting material of some experiments.

2.2 KEYWORDS: Augustine Volcano, Magma Storage, Phase Equilibria, Andesite

2.3 INTRODUCTION

The 2006 eruption of Augustine Volcano, a Pleistocene-Holocene stratovolcano located in Cook Inlet, Alaska (Figure 2.1), continued a trend for renewed unrest on a 10–30 year cycle. With documented eruptions in 1812, 1883, 1935, 1964, 1976, 1986, and 2006, Augustine is the most active volcano in Cook Inlet and as such is one of the most comprehensively monitored and studied volcanoes in Alaska (Power et al. 2010). However, until now it has not been the focus of a phase equilibria investigation.

Pre-eruptive magma storage conditions play a significant role in defining the physico-chemical properties of magmas and by extension, the style of associated volcanic activity. Experimentally recreating natural phase assemblages and phase compositions through the varying of key conditions (e.g. P-T- $X_{\text{H}_2\text{O}}$ - f_{O_2}) is an important tool for modeling the sub-surface of arc volcanoes. However, such an approach requires the assumption that samples were erupted in a state of equilibrium representing a unique set of P-T- $X_{\text{H}_2\text{O}}$ - f_{O_2} conditions (Blundy and Cashman 2008). Augustine eruptions are marked by pervasive pre- and syn-eruptive magma mixing and mingling (Roman et al. 2006; Larsen et al. 2010), and many erupted products exhibit numerous disequilibrium features rendering them unsuitable targets for a phase equilibria study. The high-silica andesite (HSA) erupted in 2006, however, appears to represent a relatively unmodified end member: it exhibits little whole-rock compositional variation (62.2–63.3 wt% SiO_2), few disequilibrium textures (Larsen et al. 2010), a homogenous low-Al amphibole population, and the lowest and most uniform apparent temperatures ($880^\circ\text{C} \pm 13^\circ\text{C}$; Tilman 2008; Larsen et al. 2010; DeAngelis et al. in revision). The HSA is inferred to represent unhybridized magma or remobilized crystal mush that resided in the shallow crust since at least the last episode of activity. Presented herein are the results of an experimental study that examines the P-T stability of magmatic phases within the HSA in order to examine

pre-eruptive storage conditions. At $X_{\text{H}_2\text{O}} = 1$ and $f_{\text{O}_2} = \text{Re-ReO}$, the natural HSA is best reproduced between 850–870 °C and ~130–150 MPa (5–6 km depth). Given the nearly identical composition of HSA magmas produced in the three most recent eruptions, the results of this study can be extrapolated to historical magma storage conditions as well.

2.3.1 Prior Studies

Eruptions of Augustine in 2006, 1986, and 1976 were similar in both products (crystal-rich andesites) and temporal progression (from initial explosive activity to effusion over a scale of weeks to months), and were all triggered by the injection of mafic magma into a cooler, shallowly stored andesite (Johnston 1978; Roman et al. 2006; Larsen et al. 2010; Steiner et al. 2012). The lack of full homogenization and the wide range of magma compositions produced during each eruption suggests an immature shallow storage region comprising interconnected dikes and sills (Roman et al. 2006; Chapter 1).

High-silica andesite samples from 2006 are uniform in whole-rock composition and mineralogy. They contain microlite-poor rhyolitic glass (45–60 modal %), plagioclase (32 modal %), augite (6 modal %), orthopyroxene (4 modal %), Fe-Ti oxides (2 modal %), and minor amphibole, olivine, and apatite (< 0.5 modal %; Larsen et al. 2010). Data from the composition of euhedral touching Fe-Ti oxide pairs indicate HSA storage at f_{O_2} conditions of NNO+1.5 (0.5 log units below RRO) and temperatures of 880°C ± 13°C (Ghiorso and Evans 2008; Figure 2.2). Webster et al. (2010) report FTIR results for plagioclase melt inclusions for two HSA samples. All inclusions (n=36) have CO₂ contents below the limit of detection (<0.003 wt%) and H₂O contents for the two are 3.08±1.3 and 3.16±0.14 wt%. These averages result in saturation pressures of ~80 MPa using the model of Newman and Lowenstern (2002); using the upper end of the analyzed range yields a saturation pressure of 130 MPa (equal to a depth of ~5 km). Average melt inclusion water contents are below that typically needed to stabilize amphibole in the melt and may have experienced leakage and/or grown during decompression crystallization. Deflation during the 2006 eruption yields a preferred storage model of a cylindrical pipe with a top at 2.5–4.5 km bsl and a base

at 6.5–10.5 km bsl (Cervelli et al. 2010). Seismic data from the 2006 eruption suggest a storage region 3.5–5 km bsl (Power and Lalla 2010).

2.4 METHODOLOGY

2.4.1 Experimental Methods

Experiments were conducted using HSA pumice sample 06AUMC004c ($\text{SiO}_2 = 62.52$ wt%; Table 2.1), emplaced during the Rocky Point pyroclastic flow on January 27, 2006 (Vallance et al. 2010). Starting material powders were prepared in 3 different ways to allow comparison of the kinetic effects imposed on experiments by their starting texture: 1) crushed natural powders (CH); 2) sintered (SNS); and 3) sintered and seeded (SS).

The HSA starting material was hand crushed using an agate mortar and pestle. The sintered starting material was produced by twice fusing 15g of crushed HSA powder in a platinum crucible, in air at 1400°C , for 30 minutes apiece, and re-grinding the fused glass to a fine powder after the heating steps. Electron microprobe analyses of the twice-fused sintered glass verified that the composition remained close to the whole-rock composition of the HSA and there was no appreciable Fe loss to the platinum crucible. For seeded experiments, this sintered powder was combined with 20 wt% plagioclase and 5 wt% amphibole. The plagioclase seeds were extracted from 06AUMC004c using heavy liquid separation. The relative scarcity of amphiboles in Augustine samples renders the extraction of seed grains inefficient. Thus seeds were taken from samples erupted from Soufrière Hills Volcano, Montserrat, in 2008. The compositions of the amphiboles in 06AUMC004c and of those in the Montserrat samples are very similar (Table 2.1). Amphiboles were separated from their host using heavy liquids and then picked by hand.

Melt inclusion data indicates that 2006 magmas were H_2O saturated but contained only trace CO_2 (Webster et al. 2010). On this basis, experiments were conducted under H_2O saturated conditions. Experiments covered a $P_{\text{H}_2\text{O}}\text{-T}$ range spanning 50–200 MPa and $800\text{--}1060^\circ\text{C}$ (Table 2.2), relevant to the Augustine system. Augustine magmas are relatively oxidized and experiments were buffered at $f_{\text{O}_2} = \text{Re-}$

ReO₂ (approximately Ni-NiO (NNO) + 2 log units). The 3mm Ag₇₀ Pd₃₀ f_{0_2} buffer capsules were loaded with Re and ReO powder in a 1:1 molar ratio. To verify the effectiveness of the buffer assemblage, 7-14 day test experiments were conducted. The compositions of seeded Fe-Ti oxide pairs from these experiments show re-equilibration verifying accurate experimental temperatures and f_{0_2} (based on the algorithm of Ghiorso and Evans 2008).

Powdered starting material (0.1g), ~ 10 wt% de-ionized H₂O, and the f_{0_2} buffer capsules were loaded into 4mm Au tubes. Experiments below 880 °C were conducted in externally heated, Rene-style, Waspaloy cold-seal pressure vessels placed in horizontal furnaces and quenched with compressed air, followed by immersion in water. Temperatures were monitored using K-type thermocouples, with accuracy verified to within 5°C by direct measurement of the melting point of gold. The thermal gradient along experimental capsules was measured and did not exceed a total of 10°C. However, because experimental charges are loaded into the base of the capsules and positioned closest to the thermocouples, experimental temperatures were likely within 5°C of reported temperatures. Experiments at temperatures above 880°C were conducted using TZM alloy pressure vessels and DelTech furnaces. In addition to the internal buffer capsules, TZM runs were buffered against loss of hydrogen by adding ~2.5 bars CH₄ to the Ar pressurizing gas. TZM runs were rapidly quenched following Sisson and Grove (1993). Experimental durations ranged from 23 to 539 hours (Table 2.2).

2.4.2 Analytical Methods

Phase identification and analysis of major oxide compositional data for experimental glasses and mineral phases were conducted using a Cameca SX50 electron microprobe at the University of Alaska Fairbanks Advanced Instrumentation Laboratory. This instrument is equipped with one EDAX energy-dispersive spectrometer and four wavelength-dispersive spectrometers. Mineral phase analyses were conducted with a 1–5 μm, 15kV, 10nA beam. Amphibole compositions were re-calculated to the mineral formula and classified according to Leake et al. (1997), based on the occupancy of the A (Na + K), B (Ca, Na), C (Mg,

Fe^{2+} , Fe^{3+} , Ti, Mn, Al_{vi} , and T (Si , Al_{iv}) sites. Recalculation to the mineral formula was based on 23 oxygens with $\text{Fe}^{2+}/\text{Fe}^{3+}$ estimation assuming 13 cations. Areas of matrix glass in experimental charges are often marginal in size compared with a defocused, ~ 10 micron diameter beam as is routinely used when analyzing hydrous glasses. Instead, a semi-focused beam (2–4 μm) with a low current of 3 nA and a voltage of 15 KeV to help reduce Na migration was utilized. Na migration was also corrected by applying linear time-dependent corrections to Na counts using the Time Dependent Intensity (TDI) function in the Probe for EPMA (PFE) software. Working standards for the experimental glass analyses included the dry and hydrous glass samples KN-18, VNM50-15, 508, and 510, as described by Devine et al. (1995) and originally utilized for calibrating EPMA analyses on hydrous glasses against FTIR data. The natural HSA glass EPMA analytical methods were similar to those described above, and full details can be found in Larsen et al. (2010).

2.5 RESULTS

The reconstruction of the Augustine 2006 high-silica andesites phase diagram (Figure 2.3) is constructed from data on experimental phase assemblages and on the compositions of experimental glasses and minerals.

2.5.1 Experimental Run Products

The modal abundances of minerals vary according to run conditions (Table 2.2 and Figure 2.4). At $P_{\text{H}_2\text{O}}=140$ MPa the liquidus is located between 1000 and 1060 °C. On the basis of both mass balance calculations and on visual observation of experimental charges, experimental glasses fall in abundance from 90 modal % in the hottest sub-liquidus experiments (at 1000 °C, $P_{\text{H}_2\text{O}}$ of 150 MPa), to 20 modal % at 820 °C and 120 MPa (Figure 2.4). Low $P_{\text{H}_2\text{O}}$ -T experiments often contain a microlite-rich groundmass (Figure 2.5a) and as a result, in a number of experimental charges, the observed glass areas were too small to analyze.

All experiments, except for those run at 1060 °C, contain orthopyroxene and ilmenite. Magnetite is identified in all experiments equilibrated at <1000°C. Mass balance calculations (Figure 2.4) suggest that oxides typically comprise <5 modal % of experimental charges. Orthopyroxene ranges from 2 to 15 modal %. Clinopyroxene is identified in several experiments run at 860°C and below. Where identified it represents up to 7 modal %. However, as it is not present in experimental charges in a systematic manner, the exact location of the clinopyroxene-in curve is not well constrained. Plagioclase is the dominant mineral phase in the majority of experiments. The maximum temperature at which stable, euhedral plagioclase is identified is at 925°C and 150 MPa, although some phenocrysts in this experiment show significant disequilibrium. The proportion of plagioclase increases from 20 modal % at 925°C up to 51 % in cooler ($\leq 860^\circ\text{C}$) experiments. Amphiboles were identified in experiments run at ≥ 120 MPa and $\leq 880^\circ\text{C}$. In all experiments amphiboles make up ≤ 5 modal %. Most experimental amphibole are euhedral and range in size from just several μm up to 30 μm . Euhedral quartz is easily identified in numerous experiments. At 160 MPa it is stable at 840°C, while at 100 MPa it is stable up to 860°C. Mass balance indicates that in some experiments it represents up to 15 modal %. In experiments using the sintered and sintered-and-seeded starting materials, biotite phenocrysts are present (at up to 15 modal %) at temperatures below 860°C. Accessory apatite is apparent in experiments of $\leq 880^\circ\text{C}$.

2.5.2 Experimental Mineral Compositions

Experimental An (anorthite) contents show a negative correlation with estimated undercooling (Figure 2.6a) for sintered and sintered-and-seeded experiments. In these experiments, plagioclase anorthite contents ranges from An70 at estimated undercoolings between 2 and 25 °C (close to the plagioclase-in curve) to \sim An55 or less at undercoolings >90 C. This relationship is less pronounced for plagioclase in crushed HSA experiments. The An numbers in crushed HSA experiments still fall from \sim An60 at undercoolings of ~ 75 °C to An50–55 at undercoolings of ~ 90 –100 °C, however high An (An70) and low An (An50) outliers are seen at undercoolings of ~ 65 –70 °C. Plagioclase An contents also increase with increasing experimental PH_2O . With the exception of some outlying points, the general trend shows An contents increasing from

~An_{50–55} at pressures ≤ 100 MPa to An₇₀ at 170 MPa. This relationship between An content and P_{H₂O} is observed in all experiment types, but again, is least pronounced in experiments using the crushed HSA starting material. This suggests that sluggish kinetics in crushed HSA experiments is inhibiting the full re-equilibration of plagioclase on experimental timescales.

Experimental pyroxenes show a range of compositions, some of which overlap with the compositions of the natural HSA phenocrysts (Figure 2.7a; Table 2.5). While some experimental clinopyroxene compositions overlap with those in the natural HSA starting material, in general clinopyroxenes in low-T experiments tend toward lower Ca and higher Fe. Similarly, while some experimental orthopyroxene compositions overlap with those in the natural HSA starting material, most tend toward relative enrichment in the enstatite end member. In general, trends in experimental pyroxene compositions with changing P_{H₂O}-T are weak (Figure 2.7b). Experimental clinopyroxene, which were only identified in sintered-and-seeded experiments, show no systematic variation in Mg# (Mg/Mg+Fe) with changes in experimental pressure or temperature (Figure 2.7b, c). They exhibit slightly lower Mg#'s (~0.7–0.74) in comparison to natural clinopyroxene from the starting material (Mg# ~0.76). There is a weak positive correlation between the Mg# of experimental orthopyroxene and both experimental pressures and temperatures (Figure 2.7b, c). In general experimental orthopyroxenes overlap natural orthopyroxene Mg#'s (~0.67) between ~100 and 150 MPa and between 820 and 870°C, although there is significant scatter in the data. As with the plagioclase data, when crushed HSA experiments are discounted the trends in the data become clearer.

Experimental amphiboles show a range of compositions. All amphiboles (Natural HSA, seed grains, and experimental amphiboles) are magnesiohornblende (Figure 2.8; Table 2.5). While there is some overlap (mainly with seed compositions), experimental amphiboles trend away from both Augustine HSA and seed amphibole compositions, exhibiting relatively elevated Si and relatively low Mg/ Mg + Fe²⁺ and Al.

2.5.3 Experimental Glass Compositions

Despite the small low-amperage beam utilized for glass analysis, locating areas of exposed glass in some experimental charges was unsuccessful. In experiments where glass was positively identified and successfully analyzed, data show consistently low totals (~ 91–94 wt%) and low alkali values (<2 wt% K₂O and <3.5 wt% Na₂O; Figure 2.9, Table 2.3). The veracity of these results was confirmed by re-probing the samples following re-polishing and reapplication of the carbon coat and by performing repeat analyses using a second microprobe (Cameca SX5 at the Cameca Demonstration Laboratory in Madison, Wisconsin). Working standards and re-analyzed natural HSA samples yield results consistent with published compositions and thus also indicate that the observed data trends are real. Low totals on electron microprobe data are a commonly observed feature of hydrous experimental glasses. For example, Hammer et al. (2002) report original total values as low as 90.2 wt % (P_{H₂O} = 100 MPa), while Rutherford and Devine (2003) report original total values as low as 93.7 (P_{H₂O} = 50 MPa). A number of factors could contribute to this issue, including errors introduced by the migration of alkali elements (e.g. Na) away from the electron beam. It is well known that this is an issue with Na (e.g., Neilsen and Sigurdsson 1981), and it is possible that the more “fragile”, depolymerized nature of hydrous silicic glasses causes similar issues in other elements as well. Following the method of Lange et al (2009), glass analyses where original totals + calculated H₂O were <97 wt% or >101 wt % were filtered out.

Experimental glasses exhibit a range of compositions that depend upon experimental conditions and on the phase assemblage (Figure 2.9; Figure 2.10). At 1060°C and 140 MPa P_{H₂O}, experimental charges (experiments Aug 76a and Aug 76b) are completely aphyric. Major oxide compositions from both sintered and crushed-HSA liquidus experiments are similar to the whole-rock composition of the high-silica andesite starting material to within ~1.3 wt% or less. Major oxide glass compositions in sub-liquidus high-T experiments (experiments Aug 65, Aug 66, Aug 67, Aug 73a, and Aug 73b; held at P_{H₂O}-T beyond the stability of plagioclase) show a progression away from the values of liquidus glasses and the whole-rock composition of the starting material (Figure 2.9). Glasses become progressively more silicic, increasing by ~5.6 wt% (Aug 73a; 1000 °C/150 MPa) to 10.2 wt% (Aug 67; 960 °C/150 MPa) silica. Concurrently, Al₂O₃

decreases by 0.6 wt% (Aug 73b; 1000 °C/150 MPa) to 2.2 wt% (Aug 67) and CaO decreases by ~1.5 wt % (Aug 73a) to 2.2 wt% (Aug 66; 940 °C/130 MPa). Glass compositions also decrease away from whole-rock and liquidus glass compositions in FeO (depleted by up to ~3 wt% (Aug 73b) and MgO (depleted by up to 1.4 wt% (Aug 66), reflecting crystallization of orthopyroxene and ilmenite in the hottest sub-liquidus experiments. K₂O values in glasses from liquidus experiments are consistent with the natural whole-rock K₂O contents. However, contrary to expectation, experimental glasses fail to become more K₂O enriched in these lower-temperature experiments following the crystallization of plagioclase, pyroxenes, and oxides. Na₂O values are also consistently depleted by between ~0.5 and 2wt% in all but one experiment (Aug 73a).

Experimental glasses from runs at conditions between the plagioclase and quartz in-curves (experiments Aug 40, Aug 45, Aug 48) evolve toward the natural HSA glass composition (Figure 2.9). SiO₂ values range from ~0 wt% (Aug 40; 880 °C/ 200 MPa) to 4 wt% (Aug 45; 925 °C/ 150 MPa) depletion in comparison to natural glass compositions. Al₂O₃ is enriched by ~1.8 wt% (Aug 40) to 2.5 wt % (Aug 45) and CaO is enriched by 0.7 wt% (Aug 40) to 2.8 wt % (Aug 45). FeO values are within less than 0.6 wt% of published HSA glass values. However, glasses are relatively highly enriched in MgO (~0.6 wt % (Aug 48; 880°C/ 160 MPa) to 1.3 wt% (Aug 45). K₂O and Na₂O remain depleted in all experiments, relative to natural HSA glasses.

For experiments within the quartz and biotite stability fields (Aug 32, Aug 37, Aug 41, Aug 49), experimental glasses show significant similarities to the natural HSA glass compositions for Al₂O₃, CaO, and FeO (to within ~1.1 wt % or less). Experimental glasses are relatively significantly enriched in SiO₂ by ~0.3 wt % (Aug 32; 860°C/ 130 MPa) to 2.2 wt% (Aug 41; 850°C/ 200 MPa) and in MgO by ~0.5 wt% (Aug 37; 840°C/ 130 MPa) to 1 wt% (Aug 41) as compared to natural HSA glasses. Again, experimental glasses are significantly depleted in K₂O with respect to natural HSA matrix glasses (by ~1 wt%). A single low-K HSA sample was identified in the 2006 deposits. It is interesting to note that the K₂O values of matrix glasses in the lowest-T experiments show excellent agreement those in this low-K HSA sample.

When major oxide glass analyses from a narrow range of pressures in the predicted storage region (130–160 MPa) are plotted against experimental temperatures, the glass compositions form a trend that extends between the compositions of the HSA whole-rock and natural glasses (Figure 2.10). For SiO₂, FeO,

and CaO (Figures 2.10a, b, c) the hottest (1060°C; experiments Aug 76a and Aug 76b) experimental glasses overlap in compositions with HSA whole-rock compositions, whereas glasses in the coolest experiments (840–850°C; experiments Aug 37 and Aug 49) overlap the HSA groundmass glasses. Two 1000 °C experiments (Aug 73a and Aug 73b) contain anomalously low FeO values. Given that this is observed in two separate experimental charges and that neither experiment is anomalous in any other major oxide a likely explanation is Fe loss to the gold capsule, although in general this process is less pronounced in high f_{O_2} (NNO+2) systems (Ratajeski and Sisson 1999). Experimental glass MgO values are elevated (by ~0.5 wt %) above both the natural whole-rock HSA (for the hottest experiments; Aug 76a and Aug 76b) and above the natural glass (for the coolest experiments; Aug 37 and Aug 49; Figure 2.9d). A similar elevation above whole-rock values is seen in the Al₂O₃ contents of the hottest (1060 °C) experimental glasses (by ~1.1 wt%). K₂O values remain similar to those of the whole-rock composition for the majority of experimental temperatures and only increase slightly in the coolest experiments (840–860 °C; Aug 37, Aug 49, Aug 32; Figure 2.9e). In these experiments K₂O values are consistent with the composition of matrix glasses in the single low-K HSA sample identified in the 2006 deposits.

2.6 DISCUSSION

2.6.1 Attainment of Equilibrium

In silicic, crystal-rich systems, crushed natural powders most closely replicate the textural conditions in the natural system. However, the solid-state re-equilibration of many silicate minerals, including plagioclase and amphibole, is an extremely slow process, taking many years to accomplish for complete equilibration (e.g. Scaillet and Evans 1999). On the scale of days to weeks, as is practical for experimental durations, only local equilibrium between crystal rims and coexisting glass may be achieved, and some phases may show no evidence for re-equilibration (Scaillet and Evans 1999). In contrast, crystallization experiments using crystal-free glass starting materials may achieve local equilibrium more quickly (e.g., Pichavant et al. 2007). However, the lack of crystals in the starting materials to act as “seed crystals” can dramatically

affect experimental kinetics. High nucleation rates may inhibit the growth of experimental “phenocrysts”, and the resulting fine-grained texture leaves few large areas of glass exposed between the crystals, making analyses problematic. Therefore, three different types of starting materials were used, consisting of both completely glassy, seeded, and crystal-rich natural powders, to assess the achievement of equilibration in experiments approaching equilibrium from melt and crystal-rich starting points, similar to reversals.

Experiments on highly silicic systems can be challenging because of slow reaction timescales, especially in crystal-rich charges with high SiO_2 groundmass melts (e.g., Brugger et al. 2003; Lange et al. 2009). This study produced experiments that evolve to melt $\text{SiO}_2 > 75$ wt. %, and thus assessment of the approach to equilibrium is critical to ensure the results compare well with the natural system. In order to achieve sufficient local equilibrium at least between crystal rims and the adjacent melt, long run times (to > 500 hours) were used, as suggested by a variety of experimental studies (e.g. Brugger et al. 2003; Martel and Schmidt 2003). Martel and Schmidt (2003) found that rhyolitic melts ($\text{SiO}_2 > 75$ wt. %) achieve equilibrium within 7 days (168 hours) for pressures greater than or equal to 100 MPa. Brugger et al. (2003) found that in their most silicic experiments ($\text{SiO}_2 \sim 75.7\text{--}77.6$) run times of 3.5 days (84 hours) or longer were required for the attainment of equilibrium. In this study of 35 experiments, 21 were held for greater than 168 hours (Table 2.2). For only 8 experimental runs were durations less than 84 hours (Table 2.2), and those were all at temperatures $> 900^\circ\text{C}$, at which equilibration timescales should be much shorter.

Standard deviations on average major oxide glass compositions for each experiment are relatively low and consistent with those deemed acceptable by other experimental studies (e.g. Hammer et al. 2002; Brugger et al. 2003; Sisson et al. 2005). For example, the mean standard deviation (1s) on Al_2O_3 for glass analyses in this study is 0.27, with a maximum of 0.62 (Aug 45). In contrast, Hammer et al. (2002), Brugger et al. (2003), and Sisson et al. (2005) report maximum standard deviations of 0.7, 0.7, and 0.9, respectively. Thus experimental glasses are sufficiently homogeneous as compared with similar studies to exhibit an acceptable approach to equilibrium.

Two double capsule experiments, in which both crushed-HSA and sintered powders were loaded in separate compartments of a single capsule (Aug 73, Aug 76), were conducted. Those experiments served as “reversals” to help assess equilibration. For the double-capsule experiments at 1000°C , phase

assemblages are the same (Table 2.2) and while mass balance calculations were only possible for the SNS experiment, visual inspection and EDS point counting reveals that phase proportions are very similar. Glass compositions are similar, with all major oxides except SiO_2 and Al_2O_3 showing compositional overlap between the experiments. Average SiO_2 and Al_2O_3 values differ by 1.5 and 0.67 wt%, respectively. One-sigma standard deviation envelopes around these values approach each other but do not converge. The lower SiO_2 and Al_2O_3 values are both seen in the crushed-HSA experiment and it is possible that minor amounts of a non-stable phase (e.g. plagioclase) have not completely dissolved, however the amount must be very minor as none was observed during extensive microprobe sessions. Both charges from the double capsule liquidus experiment are 100% glass. Average values for all major oxides are within 0.52 wt% between the experiments. One sigma standard deviation envelopes around these values converge for all oxides with the exception of SiO_2 , where uncertainty envelopes are just 0.01 wt% apart. On the basis of these results, it appears that both double capsule experiments exhibit an acceptable approach to equilibrium.

The comparison of corresponding melt-mineral compositions to established models as a means of assessing equilibrium (e.g. Lange et al. 2009) is problematic as so few models are calibrated on systems with glass compositions as evolved as those in this study. For example, only one glass data point (Aug 45; 71.7 wt% SiO_2) contains an SiO_2 value that falls within the calibration of the Lange et al. (2009) hygrometer (calibrated up to $\text{SiO}_2 < 74$ wt%). At 33 modal % crystallinity, this sample falls slightly outside of the maximum crystallinity of experiments used to calibrate the Lange et al. (2009) model. Despite this, for a glass of the composition seen in Aug 45 (H_2O calculated following the method of Newman and Lowenstern 2002), measured plagioclase An contents are similar to those predicted by the Lange et al. (2009) model (differing by just An 0.06).

While trends are generally apparent, there is significant scatter in mineral compositional data for experiments. This scatter is more pronounced in data from crushed HSA experiments. Two experiments contain unstable plagioclase that remain in the process of dissolution and resorption, indicating that while experiments are approaching equilibrium, it has not been fully or satisfactorily achieved. Crushed HSA experiment Aug 40 ($\text{PH}_2\text{O} = 200$ MPa, $T = 880^\circ\text{C}$) contains stable, euhedral plagioclase microlites, but

remnant plagioclase phenocrysts from the HSA starting material are resorbed and clearly not in equilibrium at experimental conditions. Crushed HSA experiment Aug 67 ($P_{H_2O} = 150$ MPa, $T = 960^\circ\text{C}$) contains minor quantities of small, resorbed plagioclase crystals (Figure 2.5b). This relatively short experiment (43 hours; Table 2.2) is the hottest experiment in which plagioclase is observed, yet it is no longer stable in and that the documented grains are in the final stages of dissolution.

2.6.2 Phase Stability

There is a significant increase in the total crystallinity of experimental products with decreasing P/T conditions (Figure 2.4). At the lowest P/T conditions, mass balance calculations suggest that crystallinity exceeds 80%, explaining the difficulties encountered in identifying and probing glass in many experimental charges. Average crystallinity in the natural HSA is estimated at between 45 and 55 modal % (Larsen et al. 2010), although values for 06AUMC004c specifically are slightly lower, at 40 modal %. Sintered and sintered-and-seeded experiments at 850°C and 200 MPa, and 860°C and 150 MPa, provide the closest overall match with the natural HSA, in both total crystallinity and in identified phases. However, at 860°C and 150 MPa small quantities of biotite are present. At 850°C and 200 MPa clinopyroxene was not identified. Clinopyroxene is typically the dominant pyroxene in the natural HSA, although in 06AUMC004c it is marginally less abundant than orthopyroxene. However, its appearance in experiments is not systematic.

The position and shape of the phase curves for amphibole, plagioclase, and pyroxene (Figure 2.3) are consistent with the results from other experimental studies of similar volcanic systems (e.g. Rutherford and Devine 2003, Browne and Gardner 2006). The liquidus phases are orthopyroxene and ilmenite, but there is not have enough resolution at this P-T range to determine their order relative to one another. At P_{H_2O} 130–60, magnetite becomes stable at $\sim 990^\circ\text{C}$, plagioclase at 930°C , and amphibole at 880°C .

In contrast, phase curves for quartz and biotite show significant differences in comparison with most other similar experimental studies. For example, while the natural HSA glasses are similar to those of Soufrière Hills Volcano andesite (Rutherford and Devine, 2003) and Unzen Volcano dacite (Holtz et al.

2005), the Augustine quartz curve is ~ 20–40°C hotter. However, similarities are seen with an experimental study of 1991 Mount Pinatubo dacites (Rutherford and Devine 1996). The intersection between the quartz and amphibole phase curves at Augustine is similar to that of the 1991 Mount Pinatubo dacite at ~120 MPa and 850–860°C, despite a ~0.8 wt % higher SiO₂ content of Mount Pinatubo glasses (Rutherford and Devine 1996). Further, at its highest temperature, the biotite curve for the Mount Pinatubo dacite is at 830°C. This is hotter than in other studies of similar systems. The Mount Pinatubo experiments were conducted at high f_{0_2} conditions (NNO+3), even more oxidizing than Augustine. With the exception of the Pinatubo study, the relatively high-temperature appearance of quartz at Augustine in comparison to other studies is potentially significant. It is possible that the high crystallinity of the experiments has driven the melt close to the ternary minimum (e.g., Blundy and Cashman, 2001) and near-saturation with late stage quartz and biotite. It is also possible that the high oxygen fugacity (RRO) has driven the melt to evolve to higher SiO₂ at higher P_{H₂O}-T conditions relative to systems with f_{0_2} closer to NNO. Magmatic f_{0_2} influences both the P-T range of mafic (Fe-bearing) mineral crystallization and the order in which phases appear. In the context of basaltic magmas, Sisson et al (2005) find that f_{0_2} exerts a strong influence on near-solidus phases and on melting and crystallization behavior. They find that at constant temperature, increasing the f_{0_2} of basaltic magmas encourages the consumption of both melt and Fe²⁺ amphibole components and results in the crystallization of plagioclase and Fe-Ti oxides and the production of H₂O (in the fluid and/or melt; Sisson et al. 2005). This should result in a reduction of melt fraction, driving the liquid toward more evolved compositions that encourages the stabilization of quartz.

2.6.3 Phase Compositions

Plagioclase An contents that most closely match those from natural HSA plagioclase phenocrysts are seen at undercoolings of ~90–100°C (corresponding to absolute experimental temperatures of ~840–850°C) in sintered experiments and ~70–100°C (corresponding to absolute experimental temperatures of 840–880°C) in experiments using the crushed HSA starting material (Figure 2.6a). With respect to experimental P_{H₂O},

An contents most closely match the natural system between ~120–140 MPa (Figure 2.6b). While plagioclase microlites appear to be stable, larger HSA seed phenocrysts in sintered-and-seeded experiments are resorbed at 200 MPa, suggesting that this pressure exceeds that of the natural storage region. At pressures of 120–140 MPa experimental An contents match the natural HSA at temperatures of 820 to 860°C. At these conditions, biotite and quartz are stable, although biotite only appears in experiments using a sintered starting material. The trends in An content with estimated undercoolings indicate that at >860 °C and <880 °C (where the natural phase assemblage is stable) plagioclase An contents fall between 55 and 60. These values are slightly higher than the mode of An values observed for natural plagioclase rims (~An50–55) although they encompass the mean An values of natural plagioclase rims at $An56 \pm 1$.

Experimental orthopyroxenes show weak correlations with changing experimental conditions. In contrast clinopyroxene data, albeit limited, shows no systematic changes with changing experimental conditions (Figure 2.7). While there is a known pressure dependence on the Al_2O_3 component of clinopyroxene at constant T and changing P (e.g. Putirka, 1999; Putirka et al. 2003), the lack of clinopyroxene in most experiments in this study makes assessing this relationship for the Augustine system problematic. Clinopyroxene data for experiments at constant T, but differing PH_2O , is only available for two experiments. In this limited example, the relationship holds true, with the Al_2O_3 contents of experimental clinopyroxene increasing from 1.33 ± 0.27 wt% at 860°C and 100 MPa (experiment Aug 21) to 2.66 ± 0.72 wt% at 860°C and 150 MPa (experiment Aug 10). Significantly more data is available for experimental orthopyroxene. However, there is little clear correlation between changing compositions and changing experimental PH_2O -T conditions. This is consistent with the results of other experimental studies (e.g. Prouteau and Scaillet 2003; Rutherford et al. 1985) where no clear systematic variations in pyroxene compositions were observed.

The relative scarcity of amphibole both in the natural HSA and in experimental charges makes robust conclusions from its presence and compositions challenging. While still similar in composition to both natural HSA and seed amphibole, experimental amphibole compositions are depleted in aluminum and enriched in silica (Figure 2.8). It is possible that these amphibole compositions reflect the highly evolved glasses found in low- to medium-T sintered and sintered-and-seeded experiments as a result of their high

crystallinities (~58 modal % at 860°C and 150 MPa; Figure 2.4). Unfortunately, while amphiboles crystallized in crushed HSA experiments, they were too small to yield reliable microprobe analyses. The compositions of experimental amphiboles exhibit little systematic variation with changing PH_2O -T conditions. As a result, amphibole compositions do little to further constrain the geothermobarometry of the storage region.

The lack of amphiboles in some natural Augustine magmas is likely primarily as a result of a spread in storage temperatures. Upper limits of Fe-Ti oxide derived-temperature estimates suggest that some HSA magmas were stored at temperatures exceeding that stability of amphibole (~880°C; based on the algorithm of Ghiorso and Evans 2008). Prevailing models predict that the magmas beneath Augustine are housed in a potentially complex network of interconnected dikes (Roman et al. 2006; Chapter 1), rather than a single, contiguous magma reservoir. The pressures and temperatures of the magmas stored in these dikes will vary, depending on the relative depth (and thus pressure) within the crust and on their level of interaction with hot replenishing magmas from depth.

It is possible that the relative scarcity of amphibole in Augustine HSA magmas is a direct result of this spread in storage pressures and temperatures. In addition, other factors may contribute to making the Augustine system unfavorable to amphibole stability. For example, Sisson et al. (2005) note high f_{O_2} as a potential factor in reducing quantities of amphibole at f_{O_2} conditions more oxidizing than QFM. At $f_{\text{O}_2} = \text{RRO}$, Augustine magmas are ~3 log units more oxidizing than at QFM.

Experimental glasses trend between the values for the whole-rock HSA starting material and the natural HSA glasses for all major oxides with the exception of the alkalis (K_2O and Na_2O ; Figure 2.9), which are depleted in almost all experimental glasses (see below). Experimental glasses formed between 130 and 160 MPa most closely match the composition of the natural HSA glass. However, by 860 °C minor quantities of biotite are stable in sintered starting material experiments and by 850°C quartz stability has been reached (at $\text{PH}_2\text{O} < 150$ MPa). As such, natural HSA glass compositions are not experimentally re-created in regions in which the phase inventory matches the natural system.

2.6.4 Low Alkalis in Experimental Glasses

Low alkali values are a feature of almost all experimental glasses in this study. With respect to sodium, low Na values are also seen in working standards and likely stem from Na migration in the glass away from the electron beam, as noted by previous authors (Nielsen and Sigurdsson 1988; Devine et al. 1995). However, an intriguing aspect of the experimental glass chemistry is the behavior of potassium. For experiments approaching the liquidus, K_2O behaves as expected, decreasing in the melt from starting concentrations close to those of the whole-rock (~1 wt%; Figure 2.9c). Highly incompatible in most minerals, K_2O in experimental glasses should increase with increasing SiO_2 and with increasing degree of crystallization as experimental temperatures and pressures decrease. The only experiments to exhibit a clear increase in K_2O (up to ~1.5 wt%) are those that fall within the stability fields of biotite and quartz. In no experiment do K_2O values reach the level seen in the natural HSA glasses (~2–3 wt%). Similar to Na migration, the migration of K away from the electron beam during electron microprobe analysis has also been documented. However, the effect is significantly less pronounced (Reed 2005) and given the low amperage beams utilized, it is unlikely that loss of this kind is significant. This is supported by the electron microprobe data that do not show similar K depletion in working standards. Further, time dependent K count data on experimental glasses do not exhibit systematic decreases with time. Potassium is relatively insoluble in super-critical H_2O fluid and is not known to alloy with gold capsules during hydrothermal experiments like Fe does (Ratajeski and Sisson 1999). To deplete the melt by the extent observed, potassium must be taken into mineral phases. The only viable options are the crystallization of potassium-rich feldspars (e.g. sanidine) or biotite micas.

Glass compositions in this group show similarities in composition with glasses from a single low-K HSA sample identified in the natural Augustine 2006 deposits. Mass balance calculations predict that the crystallization of ~2–3 wt% biotite in the natural HSA would produce the observed low-K composition. However, biotite has not been identified in the low-K sample (or any natural sample). Sanidine has also not been identified in any natural or experimental samples, where feldspars are all plagioclase. A small number of experimental plagioclase do show significant potassium enrichment, some with >5 mol % Or which may

also account for some of the K_2O depletion observed in the melt. Another possible explanation for apparent K enrichment in feldspars is the contamination of data from the electron beam partially hitting areas of K-enriched glass. However, given both the relative ease of plagioclase analyses (resulting from the abundance of relatively large crystals) and the low-K nature of the experimental glasses in general, this is unlikely.

2.6.5 Biotite Crystallization from a Low-K Andesite

Experimental biotite is generally not observed above $\sim 800^\circ\text{C}$ in experimental studies of calc-alkaline andesitic systems (e.g. Rutherford and Devine 2003, Holtz et al. 2005), although in studies of more mafic and crystal-poor magmas, biotite has been seen to crystallize at temperatures greater than 900°C (Barclay and Carmichael 2004). The only exception is in an experimental study of a similarly highly oxidized system (Mt Pinatubo, Philippines; $\text{NNO}+2$ to $\text{NNO}+3$) where biotite is also seen to crystallize at relatively high temperatures ($810\text{--}830^\circ\text{C}$ at $150\text{--}250$ MPa; Rutherford and Devine 1996). This suggests that f_{O_2} exerts a significant influence on the stability of biotite in silicic systems.

The possibility of contamination of experiments with biotite during seeding with Soufrière Hills derived amphiboles is excluded for three reasons: 1) biotite is not stable in Soufrière Hills andesites under natural storage conditions (although it has been formed experimentally at temperatures $<780^\circ\text{C}$; Rutherford and Devine 2003); 2) even if biotite was present in seed material it should have been removed during the process of heavy liquid separation (biotite has lower density than hornblende) and the during the hand picking of seed amphibole grains; and 3) biotite has been identified in experiments using both seeded and unseeded starting materials. However, starting material is clearly an important factor as sintered (seeded and unseeded) experiments are the only ones to contain biotite crystals. The high crystallinity, evolved melt compositions and slow kinetics of the natural high-silica andesite may explain why biotite fails to crystallize in the natural system, despite being stable (as indicated by their presence in experiments utilizing the sintered starting material). On the basis of phase stability alone, it is entirely possible for HSA storage to have occurred within the biotite stability zone without the appearance of biotite in the natural

samples. However, the lower temperatures of HSA storage are still constrained only by the relatively hot quartz curve, as quartz is identified in experiments of all kinds.

2.7 CONCLUSIONS: MODEL FOR PRE-ERUPTIVE MAGMA STORAGE

On the basis of petrological, seismic and geodetic data, previous estimates for the depth of shallow storage at Augustine have ranged between 2.5 to 8 km bsl (65 to 210 MPa) for the top of the storage region and ~ 5 to 12 km bsl (170 to 310 MPa) for the base (Cervelli et al. 2010; Power and Lalla 2010; Webster et al. 2010; Chapter 1). Temperature estimates for HSA, calculated from the composition of co-existing Fe-Ti oxide pairs and the algorithm of Ghiorso and Evans (2008), are 853–908°C, with an average value of 880°C \pm 13°C (Figure 2.2). While the lower end of the range encompasses the experimental estimates (~850–860°C), the average is higher (880°C \pm 13°C). In contrast, when the QUILF algorithm (Andersen et al. 1993) is applied to the same Fe-Ti oxide compositional data, the temperature range is 811–868°C, with an average value of 838°C \pm 14°C (Figure 2.2; Larsen et al. 2010). These QUILF-derived temperatures have been corrected (reduced) by 30°C (from original values of 841–898°C) to account for an overestimation by the algorithm when applied to highly oxidized magmas (RRO or NNO+ 2 to NNO+3; Geschwind and Rutherford 1992; Rutherford and Devine 1996).

Experimental mineral stability and compositions provide a significant refinement in the range of possible P_{H_2O} -T conditions for the Augustine HSA (Figure 2.3). The early (hot) appearance of quartz and biotite means that the natural HSA assemblage is only observed in a restricted area of the phase diagram: above 120 MPa and between approximately 860 and 880°C. Plagioclase An contents indicate HSA storage at pressures of 130–150 MPa and at temperatures of ~ 820–870°C, whereas glass compositions indicate a range in temperatures from ~ 850 to 860°C (at P_{H_2O} ~130–160 MPa). Estimated temperatures fall between those estimates from the two Fe-Ti oxide algorithms applied to the natural HSA (Andersen et al. 1993; Ghiorso and Evans 2008). They also straddle the boundary of biotite stability. Biotite has not been identified in any natural HSA samples. Given that experimental biotite is only identified in experiments using the sintered starting material, it would appear that the high crystallinity, highly evolved melt

compositions, and slow kinetic regime inhibits the initiation of biotite crystallization in crushed HSA experiments (and in natural HSA). As such, natural HSA stability may intrude into the biotite stability zone, although temperatures below ~850 °C are still unlikely given the stability curve of quartz.

2.8 ACKNOWLEDGEMENTS

The authors are indebted to Ken Severin and to the staff of the Alaska Volcano Observatory. This work was supported by a grant from the National Science Foundation (NSF EAR 0911694).

2.9 FIGURES

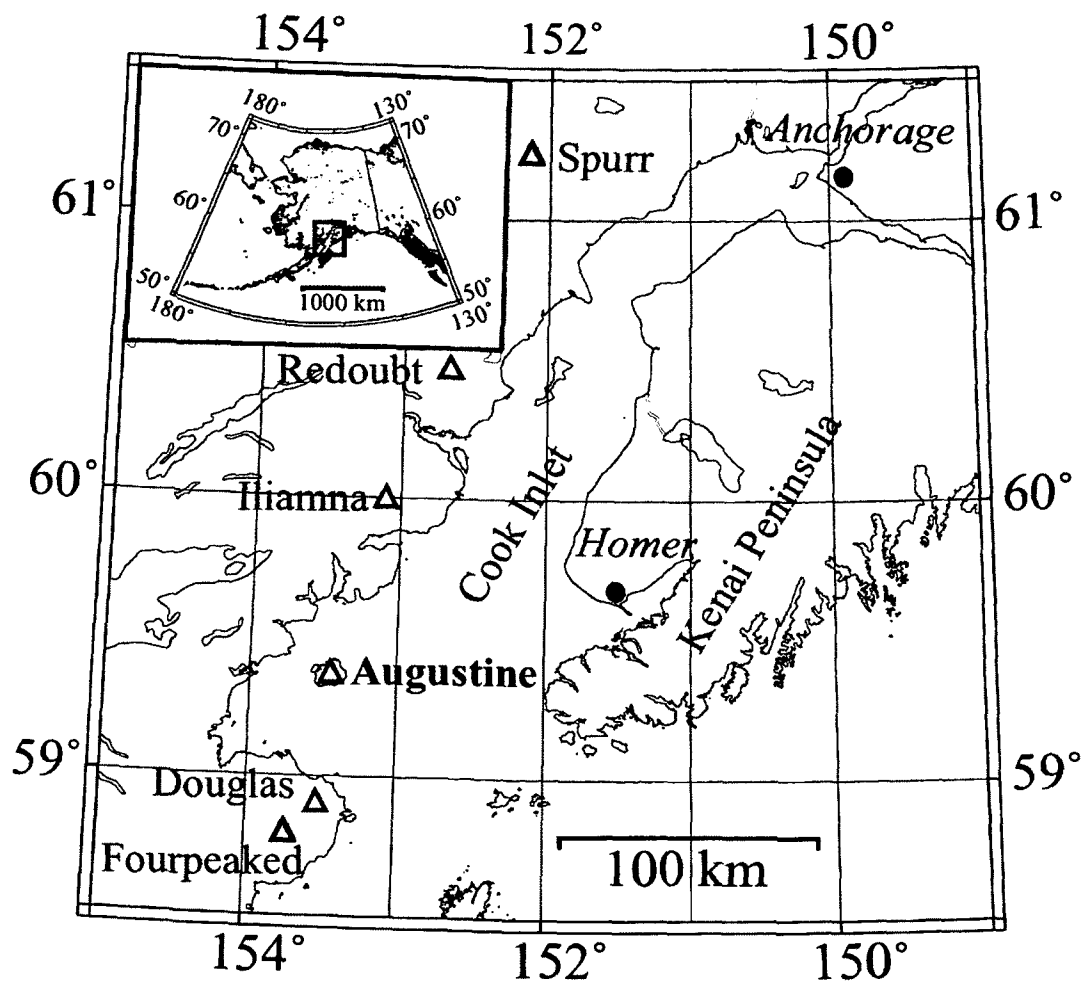


Figure 2.1 Maps showing the location of Augustine Volcano. Inset map shows Alaska with the Cook Inlet region highlighted. Triangles denote volcanoes.

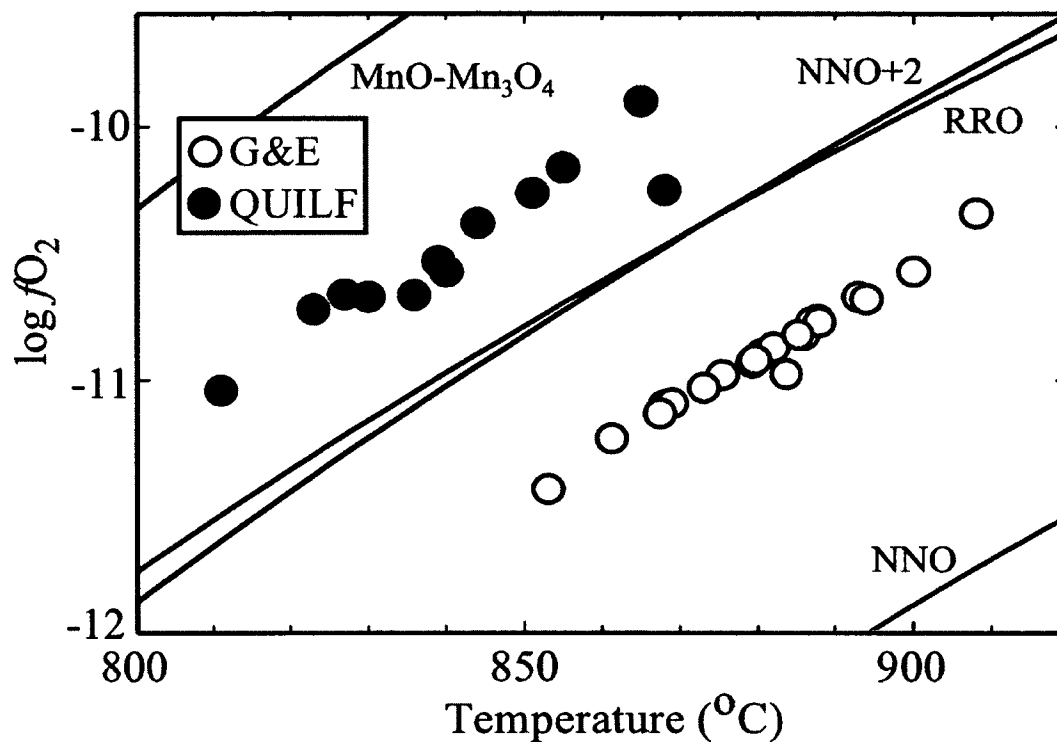
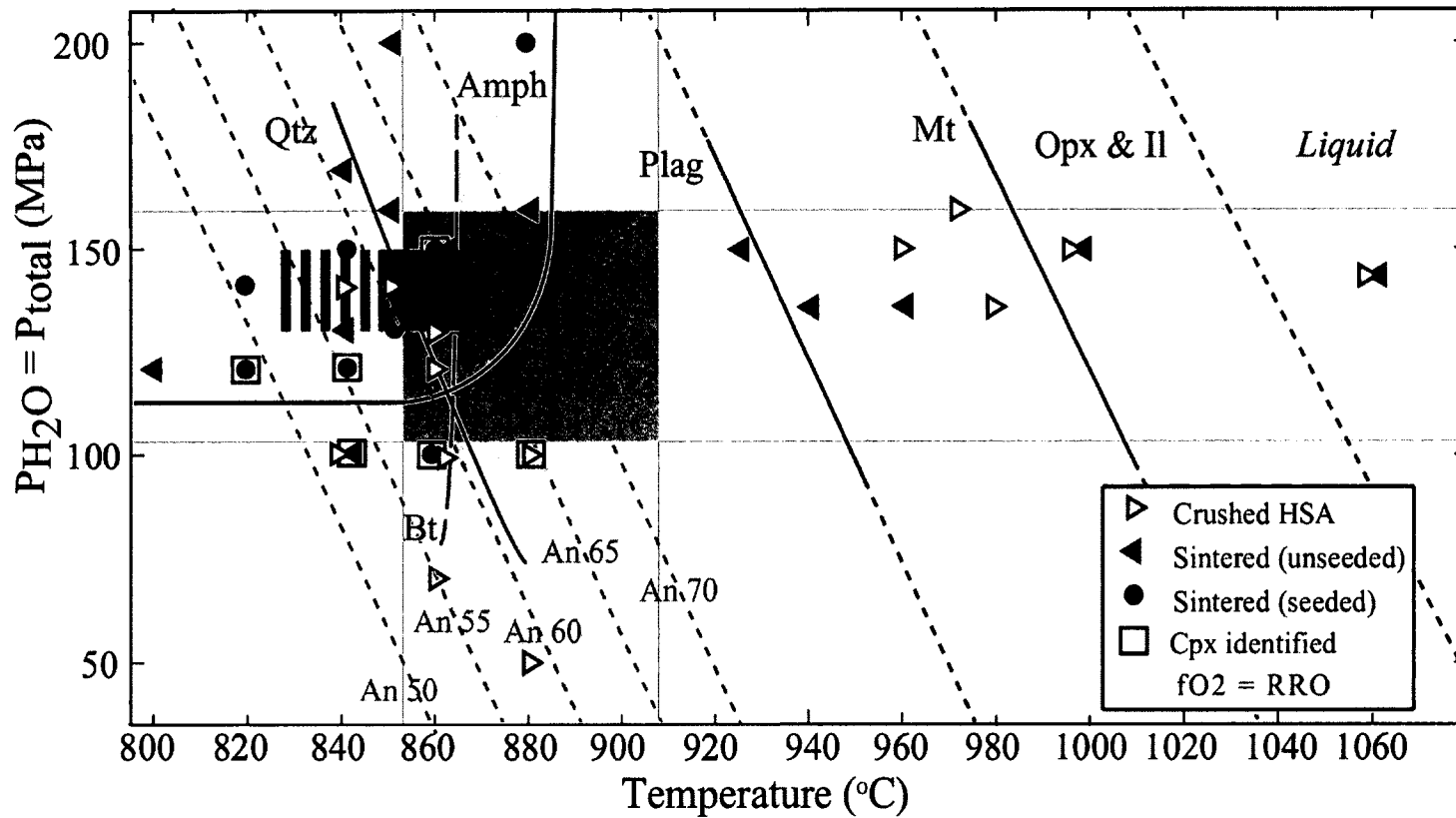


Figure 2.2 High-silica andesite oxygen fugacity and temperatures. Data calculated from the compositions of euhedral touching Fe-Ti oxide pairs. White circles denote calculations following the algorithm of Ghiorso and Evans (2008). Grey circles denote recalculations, on a subset of the same data, following QUILF algorithm (Andersen et al. 1993). QUILF derived temperatures have been corrected by 30°C to account for an overestimation by the algorithm when applied to highly oxidized magmas (Geschwind and Rutherford 1992; Rutherford and Devine 1996).

Figure 2.3 Phase diagram. The biotite phase curve is coarsely dashed indicating identification only in experiments using a sintered starting material. Finely dashed curves indicate extrapolated phase boundaries. Right-pointing triangles denote crushed HSA starting material, left-pointing triangles denote sintered-and-unseeded starting material, black circles denote sintered-and-seeded starting material. The direction of the arrows approximates the approach to equilibrium with the crystal-rich crushed starting materials as melting experiments and the glassy (sintered) materials as crystallization runs. White squares indicate the presence of clinopyroxene. Qtz = quartz, Bt = biotite, Amph = amphibole, Plag = plagioclase, Mt = magnetite, Opx = orthopyroxene, Il = ilmenite, Cpx = clinopyroxene. Light gray dashed lines indicate estimated mol % An (anorthite) for plagioclase at given P/T conditions. The lightly shaded horizontal grey box denotes the pressure range for HSA storage based on natural melt inclusions (Webster et al. 2010). The lightly shaded vertical grey box denotes the temperature range for HSA storage based on Fe-Ti oxides in natural HSA samples. The dark grey horizontal shaded area denotes the area in which experimental glass compositions most closely match that of the natural HSA starting material (06AUMC004c). The hashed grey area denotes the region in which experiment plagioclase exhibit mol % An contents that match the natural HSA starting material (06AUMC004c)



Pressure range from melt inclusions
(Webster et al, 2011)

Experimental An matches HSA

Fe-Ti Temperature range
(Based on the algorithm of Ghiorso and Evans, 2008)

Estimated temperature to form HSA glass

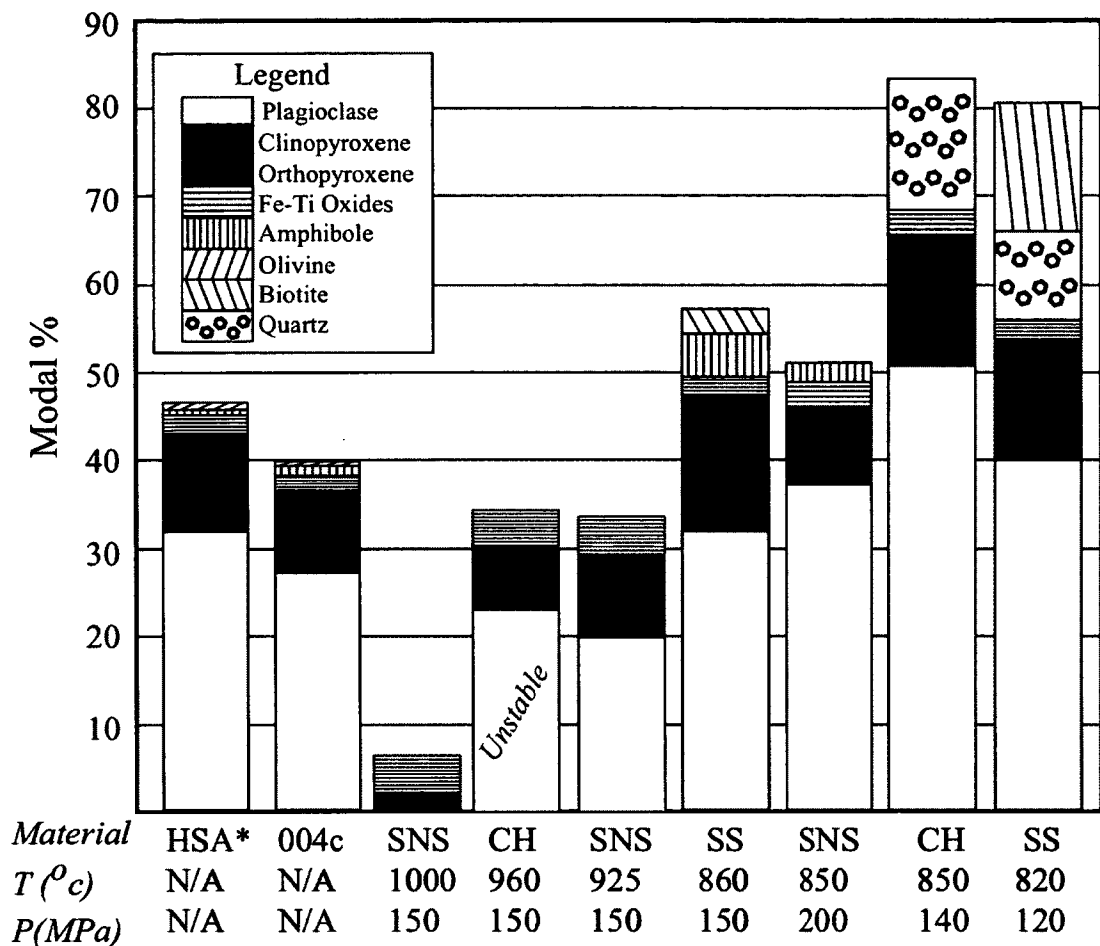


Figure 2.4 Modal abundance of minerals in natural HSA and selected experiments. HSA* represents the average modal abundance of all natural high-silica andesite samples (Larsen et al. 2010) and 004c represents modal abundances of the experimental starting material (06AUMC004c). Data on the experimental samples determined by mass balance. SNS = sintered-and-unseeded starting material, SS = sintered-and-seeded starting material, CH = crushed HSA starting material. T = temperature, P = pressure

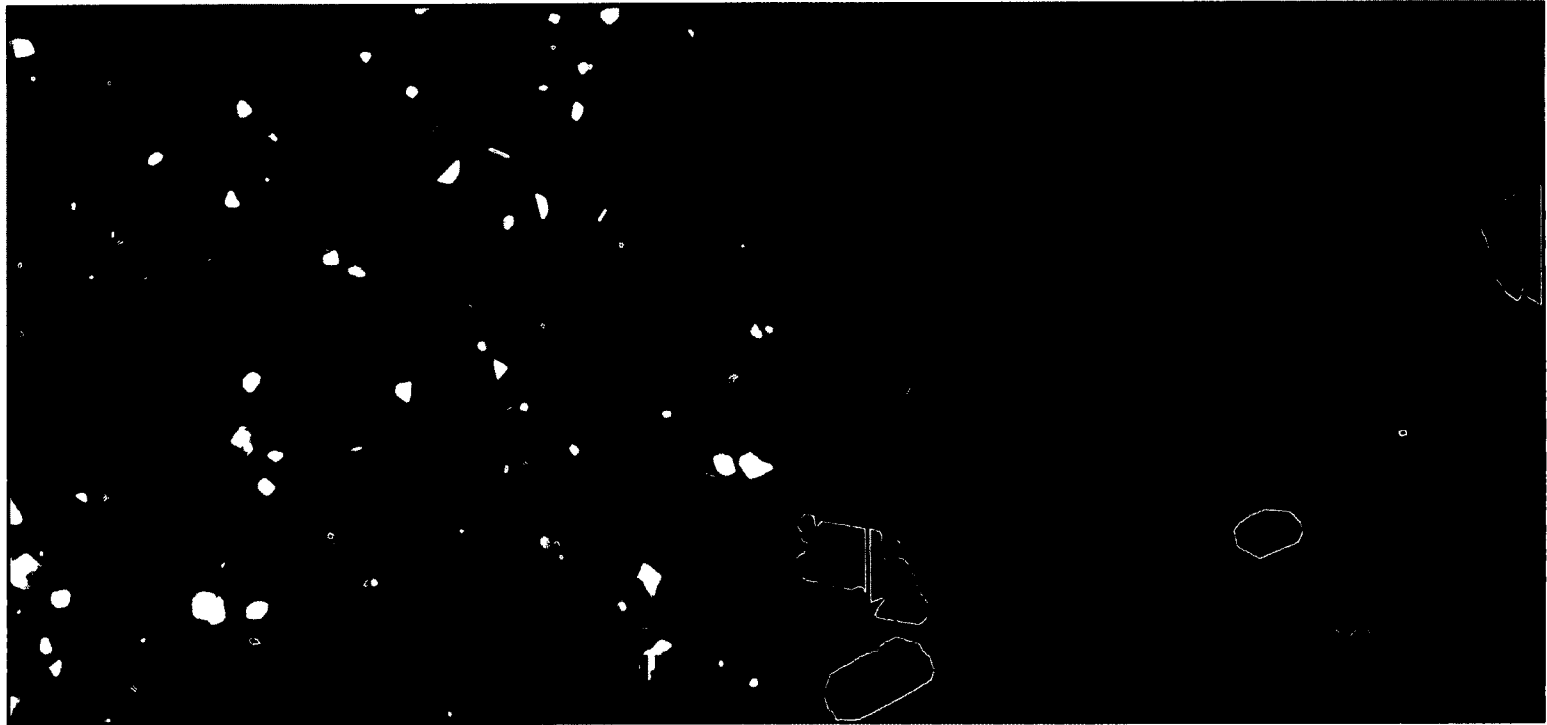


Figure 2.5 BSE images of experimental groundmass. Panel (a) shows microlite rich groundmass in experiment Aug 31. This experiment was conducted using the sintered-and-seeded starting material and was held at 840°C and 150 MPa for 539 hours. Panel (b) shows glass-rich experiment Aug 67. This experiment was conducted using the crushed-HSA starting material and was held at 960°C and 150 MPa for 43 hours. Unstable plagioclase in Aug 67 indicates that this experiment only reached partial equilibrium. Plag = plagioclase, Px = pyroxene, Gl = glass, Fe-Ti Ox = Fe-Ti oxides (magnetite and ilmenite).

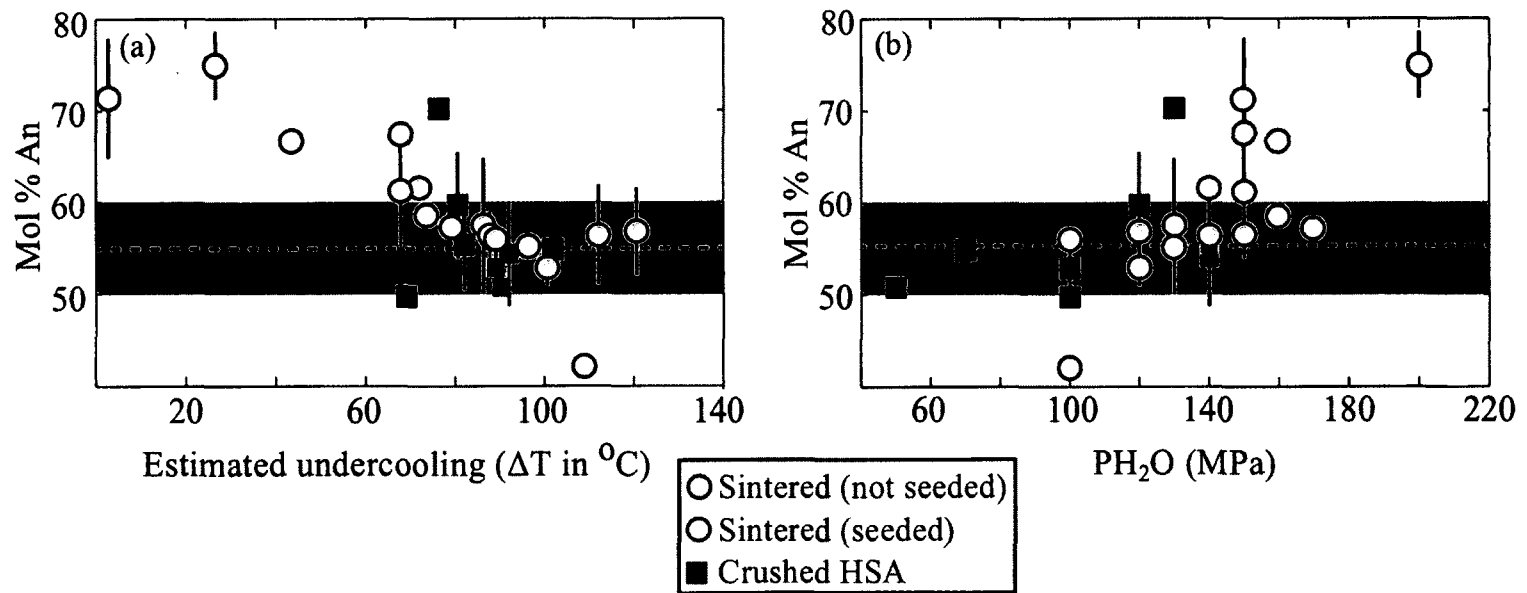
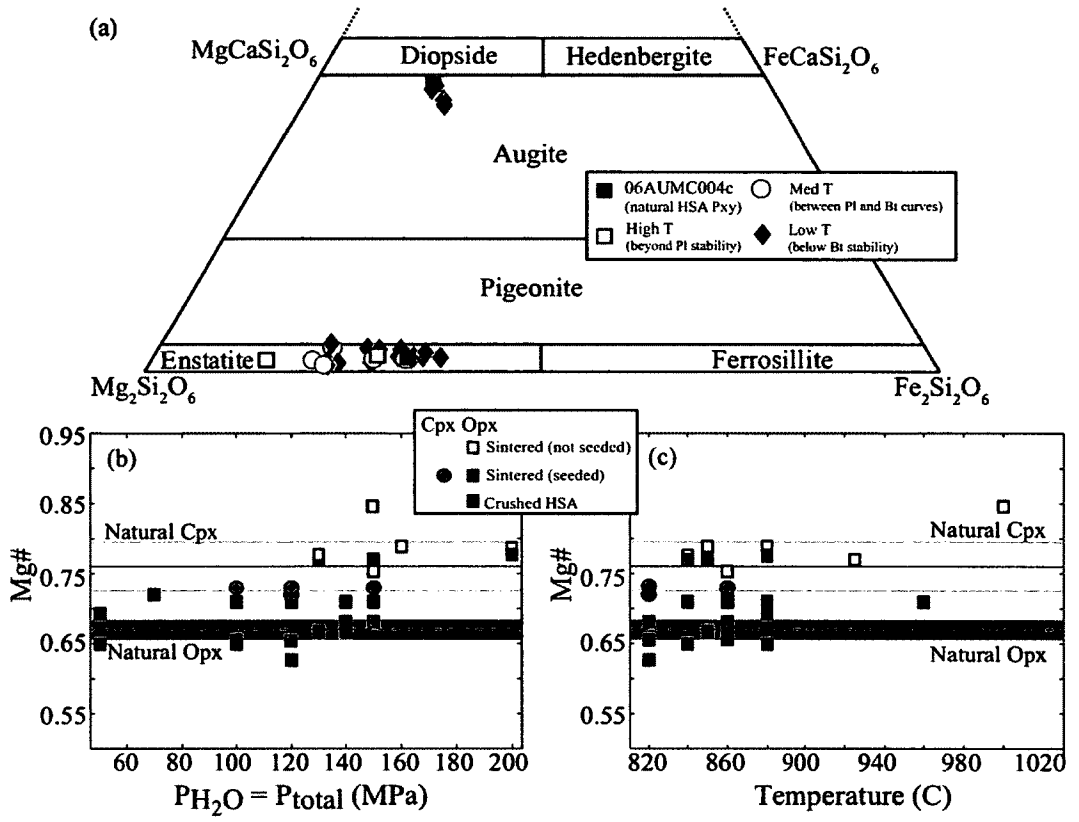


Figure 2.6 Experimental and natural plagioclase compositions. Panel (a) represents variations in experimental mol % An (anorthite) values with estimated degree of undercooling away from the plagioclase stability curve; (b) Mol % An (anorthite) plotted against experimental PH_2O . Each data point represents the average of all analyses for a given experiment. Error bars on mol % An represent the (1s) standard deviation. The dashed black line and surrounding lightly shaded grey area represents the mean and standard deviation (1s) of the An content of plagioclase phenocryst rims in the natural HSA.

Figure 2.7 Experimental and natural pyroxene compositions. Panels (a) represents the pyroxene classification quadrilateral showing the average compositions from all analyses within each sample or experiment. Data points are larger than the calculated error bars (1s) estimated using the full uncertainty propagation methods of Giaramita and Day (1990) and De Angelis and Neill (2012). Black squares denote rim compositions of pyroxene in the natural high-silica andesite (HSA) starting material (06AUMC004c). Experimental data are sorted according to the region of the phase diagram in which they were conducted: White squares denote high temperature experiments in the region beyond the stability of plagioclase (Pl); grey circles denote medium temperature experiments conducted between the plagioclase and biotite (Bt) phase curves; grey diamonds denote low temperature experiments conducted within the biotite stability field (in which quartz is also often present). (b) Plot showing the variation in Mg# ($Mg/(Mg+Fe)$) of experimental pyroxene with changing experimental pressures. Each point represents the average of all analyses from each experiment. The solid black line and surrounding darkly shaded grey area represents the average standard deviation (1s) of the Mg# for orthopyroxene rims in the natural high-silica andesite (HSA) starting material (06AUMC004c). The dashed black line and surrounding lightly shaded grey area represents the mean and standard deviation (1s) of the Mg# for clinopyroxene rims in the natural high-silica andesite (HSA) starting material (06AUMC004c). Cpx = clinopyroxene, Opx = orthopyroxene. Sintered- and-seeded experiments contained all identified Cpx.



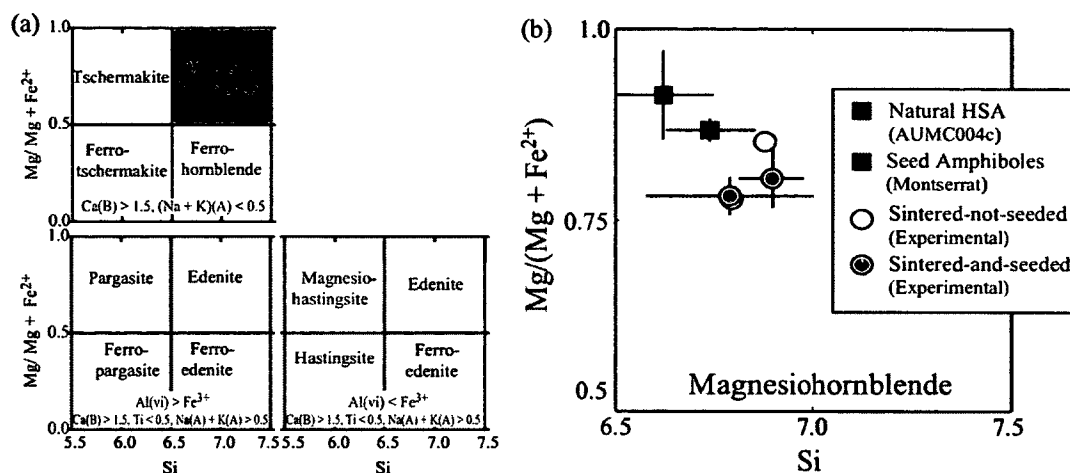


Figure 2.8 Experimental and natural amphibole compositions. Panel (a) denotes the Leake et al. (1997) classification diagram for calcic amphiboles. Grey shading indicates the fields in which natural and experimental amphiboles are found. These fields are expanded in (b) which shows the variations in Si and Mg# for natural and experimental amphiboles. Each symbol represents the average of all compositional analyses from each sample/ experiment. Error bars (1s) were calculated using full uncertainty propagation methods (Giaramita and Day 1990, De Angelis and Neill 2012). Black squares denote amphiboles from the natural high-silica andesite (HSA) starting material (06AUMC004c); grey squares denote amphibole seed compositions from the Soufrière Hills, Montserrat andesite; white circles denote amphibole from experiments using the sintered-and-unseeded starting material; grey circles denote amphibole from experiments using the sintered-and-seeded starting material.

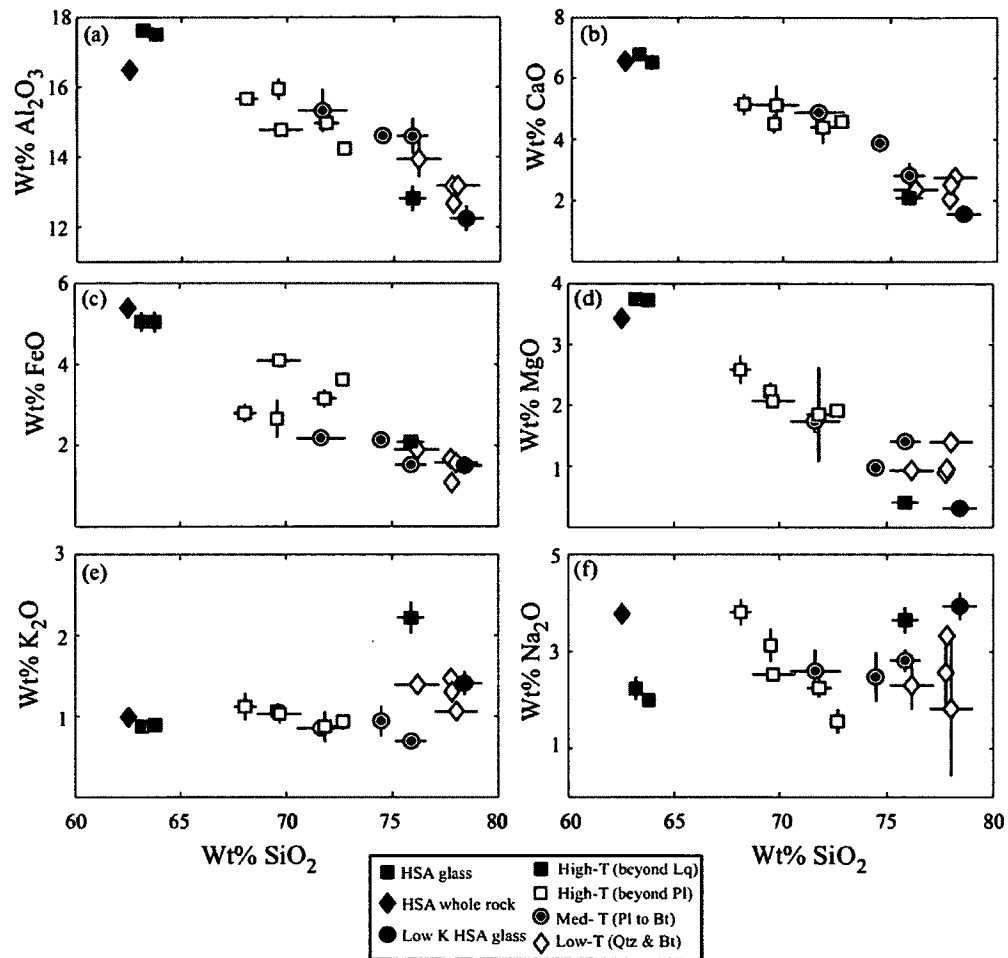


Figure 2.9 Harker plots of experimental and natural glass compositions. Panels denote variations of SiO_2 with (a) Al_2O_3 ; (b) CaO ; (c) K_2O ; (d) Na_2O ; (e) FeO ; and (f) MgO . Data represent the average of all data points for a given sample/experiment. Error bars represent the analytical standard deviation (1s). Black squares denote natural HSA groundmass glasses and the black diamonds denote the natural HSA starting material whole-rock composition (both from sample 06AUMC004c). Black circles represent the average groundmass glass composition from the natural low-K HSA sample (Larsen et al. 2010). Experimental data are classified by mineralogy of the experimental charges: Grey squares Lq denote experiments conducted at temperatures exceeding the liquidus; white squares denote experiments conducted at temperatures between the liquidus and the stability curve for plagioclase (Pl); grey circles denote medium-temperature experiments conducted within the plagioclase stability zone that do not contain quartz (Qtz) and/ or biotite (Bt); grey diamonds denote low-temperature experiments within the quartz and biotite stability fields.

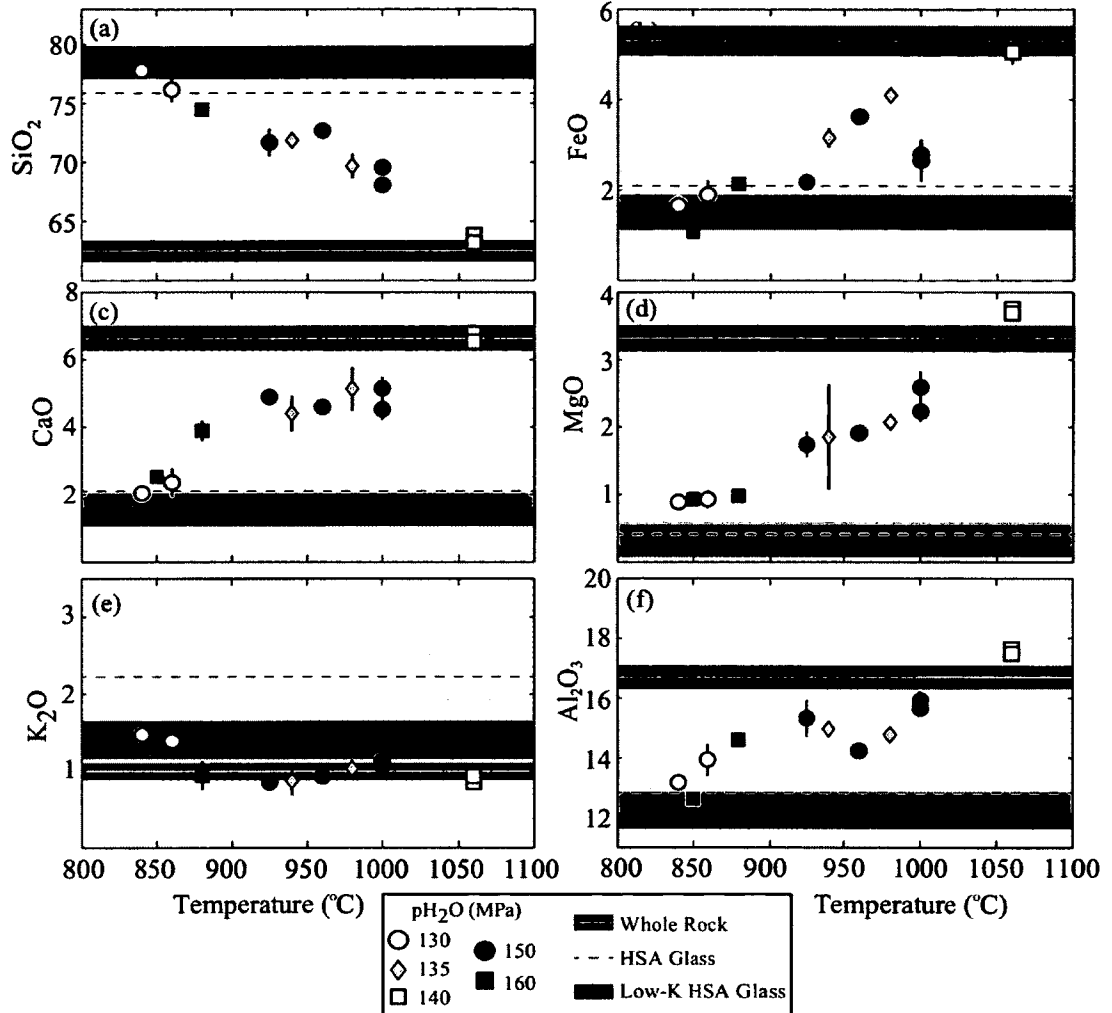


Figure 2.10 Near isobaric variations in experimental glass major oxide compositions. Panels represent variations in (a) SiO₂; (b) FeO; (c) CaO; (d) MgO; (e) K₂O; (f) Al₂O₃. Each symbol represents the average of all glass analyses for each experiment, with error bars representing the standard deviation (1s). The dashed line and surrounding light grey shaded area denotes the average and standard deviation (1s) for natural HSA groundmass glass (06AUMC004c). The solid grey line and surrounding dark grey shaded area denotes the average and standard deviation (1s) from the natural HSA whole-rock (06AUMC004c). The dotted line and surrounding medium-grey shaded area denotes the average and standard deviation (1s) for the low-K HSA groundmass glass compositions (Larsen et al. 2010).

2.10 TABLES

Table 2.1: Representative starting material compositions

	HSA Whole Rock ^b	HSA Matrix Glass ^b	HSA Amph ^{a,d}	SHV Seed Amph ^a	HSA Plag ^a	HSA Opx ^a	HSA Cpx ^a
Sample	MC004c ^c	MC004c	MC004c Grain 1	SH08 Grain 7	MC004c Grain 31	MC004c Grain 8	MC004c Grain 6
SiO ₂	62.52	75.86 (0.64) [*]	46.65 (0.52)	47.21 (0.10)	53.76 (0.30)	53.18 (0.26)	52.11 (0.21)
TiO ₂	0.56	0.44 (0.18)	1.57 (0.27)	1.39 (0.03)	N/A	0.16 (0.02)	0.31 (0.02)
Al ₂ O ₃	16.48	12.81 (0.36)	8.71 (0.36)	7.44 (0.07)	28.87 (0.24)	0.83 (0.15)	1.72 (0.09)
FeO (t)	5.39	2.08 (0.18)	11.93 (0.42)	14.23 (0.21)	0.49 (0.09)	20.12 (0.41)	9.34 (0.24)
MnO	0.13	0.08 (0.09)	0.48 (0.09)	0.56 (0.07)	N/A	0.74 (0.14)	0.38 (0.07)
MgO	3.43	0.41 (0.06)	15.31 (0.33)	13.99 (0.16)	N/A	23.41 (0.21)	14.04 (0.23)
CaO	6.58	2.09 (0.19)	10.64 (0.18)	10.76 (0.03)	11.33 (0.04)	0.99 (0.06)	20.90 (0.46)
Na ₂ O	3.78	3.65 (0.27)	1.74 (0.10)	1.20 (0.07)	4.91 (0.08)	0.02 (0.01)	0.41 (0.04)
K ₂ O	0.99	2.22 (0.20)	0.12 (0.03)	0.14 (0.02)	0.12 (0.02)	N/A	N/A
P ₂ O ₅	0.14	0.08 (0.04)	N/A	N/A	N/A	N/A	N/A
Cl	N/A	0.28 (0.06)	N/A	N/A	N/A	N/A	N/A
Total ^e	100.34	99.49 (0.61)	97.15 (0.51)	96.91 (0.31)	99.48 (0.56)	99.44 (0.60)	99.21 (1.10)
n	N/A	37	9	5	3	3	3

^a Full dataset available in Appendix 2.1.

^b Data from Larsen et al. 2010

^c "06AU" removed from sample name for the sake of brevity

^d Amph = amphibole; Plag = plagioclase; Cpx = clinopyroxene; Opx = orthopyroxene

^e Glass totals are original totals. Glass data are anhydrous and normalized to 100

^{*} Data average of 'n' analyses with standard deviation in brackets

Table 2.2: Experiments and experimental products

Code	SM ^a	T (°C)	P (MPa)	Time (Hrs)	Phases ^a
Aug 09	SS	860	140	330	Pl, Op, Ox, gl
Aug 10	SS	860	150	162	Pl(0.32) ^c , Opx(<0.1), Cpx(0.1), Hb(<0.1), Ox(0.1), B(<0.1), A(<0.1), gl(0.42)
Aug 11	CH	850	140	186	Pl(0.51), Opx(0.15), Q(0.15), Ox(<0.1), A(<0.1), gl(0.16)
Aug 12	CH	860	120	285	Pl, Opx, Q, Ox, gl
Aug 14	CH	840	140	354	Pl, Opx, Hb, Q, Ox, gl
Aug 15	SS	840	120	309	Pl, Opx, Cpx, Hb, Ox, B, A
Aug 16	SS	820	140	309	Pl, Opx, Hb, Q, Ox, B, gl
Aug 19	SS	820	120	239	Pl(0.4), Opx(<0.1), Cpx(<0.1), Q(0.1), Ox(<0.1), B(0.15), gl(0.2)
Aug 21	SS	860	100	286	Pl, Opx, Cpx, Ox, B
Aug 24	SS	820	120	237	Pl, Opx, Cpx, Hb, Q, Ox, gl
Aug 28	SS	850	130	360	Pl, Opx, Hb, Q, Ox, gl
Aug 31	SS	840	150	539	Pl, Opx, Hb, Q, Ox
Aug 32	CH	860	130	277	Pl, Opx, Hb, Ox, gl
Aug 33	CH	860	100	384	Pl, Opx, Q, Ox
Aug 34	CH	860	70	360	Pl, Opx, Q, Ox, A
Aug 35	CH	840	100	381	Pl, Opx, Q, Ox, A, gl
Aug 36	CH	880	100	404	Pl, Opx, Cpx, Hb, Ox, A
Aug 37	SNS	840	130	190	Pl, Opx, Hb, Q, Ox, gl
Aug 38	CH	880	50	215	Pl, Opx, Ox
Aug 40	SS	880	200	480	Pl ^d , Opx, Hb, Ox, gl
Aug 41	SNS	850	200	145	Pl(0.37), Opx(<0.1), Hb(<0.1), Ox(<0.1), gl(0.5)
Aug 42	SNS	860	150	317	Pl, Opx, Hb, Ox, gl
Aug 43	SNS	840	100	220	Pl, Cpx, Q, Ox, B
Aug 44	SNS	800	120	162	Pl, Hb, Q, Ox
Aug 45	SNS	925	150	72	Pl ^e (0.2), Opx(<0.1), Ox(<0.1), gl(0.67)
Aug 47	SNS	840	170	162	Pl, Opx, Hb, Q, Ox, A, gl
Aug 48	SNS	880	160	162	Pl, Opx, Hb, Ox, gl
Aug 49	SNS	850	160	166	Pl, Opx, Hb, Ox, gl
Aug 50	SNS	960	130	30	Opx, Ox ^f , gl
Aug 64	CH	970	160	48	Opx ^g , Ox, gl
Aug 65	CH	980	135	47	Opx ^g , Ox, gl
Aug 66	SNS	940	135	52	Opx, Ox, gl
Aug 67	CH	960	150	43	Pl ^e (0.23), Opx(<0.1), Ox(<0.1), gl(0.66)
Aug 73a ^h	CH	1000	150	69	Opx, Ilm, gl
Aug 73b ^h	SNS	1000	150	69	Opx ^f (<0.1), Ilm(<0.1), gl(0.9)
Aug 76a ^h	CH	1060	140	23	gl(1)
Aug 76b ^h	SNS	1060	140	23	gl(1)

^a Starting Material: CH=Crushed HSA, SS= Sintered, SNS=Sintered (not seeded)

^b Pl=plagioclase, Opx=orthopyroxene, Cpx=clinopyroxene, Q=quartz, Ox=oxides (magnetite and ilmenite), B=biotite, A=Apatite, Ilm=ilmenite, gl=glass

^c Modal data calculated by mass balance. Full data in Appendix 2.2.

^d Large plagioclase seeds are unstable and skeletal. Small plagioclases are stable and euhedral

^e All plagioclase are rounded and <20 µm

^f All crystals are <20 µm

^g All crystals are unstable and resorbed

^h Double capsule experiment

Table 2.3: Representative experimental glass compositions^a

SM ^b	SNS	SNS	CH	CH
Experiment	Aug 37	Aug 48	Aug 65	Aug 76a
T (°C)	840	880	980	1060
P (MPa)	130	160	135	140
SiO ₂	77.77 (0.30)*	74.48 (0.31)	69.64 (0.74)	63.80 (0.23)
TiO ₂	0.30 (0.03)	0.41 (0.18)	0.55 (0.24)	0.52 (0.09)
Al ₂ O ₃	13.18 (0.16)	14.60 (0.25)	14.78 (0.06)	17.51 (0.11)
FeO (t)	1.66 (0.04)	2.13 (0.08)	3.90 (0.33)	5.04 (0.26)
MnO	0.09 (0.00)	0.28 (0.00)	0.04 (0.16)	
MgO	0.89 (0.03)	0.98(0.09)	2.17 (0.18)	3.73 (0.08)
CaO	2.04 (0.08)	3.89 (0.30)	5.04 (0.48)	6.53 (0.25)
Na ₂ O	2.56 (0.66)	2.48 (0.51)	2.51 (0.04)	1.99 (0.13)
K ₂ O	1.47 (0.03)	0.94 (0.19)	1.29 (0.46)	0.89 (0.04)
Cl	0.04 (0.01)	0.00 (0.00)	0.08 (0.06)	
Original Total ^c	92.80 (0.71)	92.56 (0.62)	93.62 (1.12)	93.45 (0.29)
n	3	3	3	5
H ₂ O ^d	4.56	4.71	4.25	4.15

^a Full dataset available in Full dataset available in Appendix 2.3.

^b Starting Material: CH=Crushed HSA, SS= Sintered, SNS=Sintered (not seeded)

^c Glass totals are original totals. Glass data are anhydrous and normalized to 100%

^d H₂O calculated using VolatileCalc (Newman and Lowenstern, 2002)

^e Modal data calculated by mass balance

* Data average of 'n' analyses with standard deviation in brackets

Table 2.4: Representative experimental plagioclase compositions^a

SM ^b	SS	SS	SNS	CH
Experiment	Aug 21	Aug 31	Aug 47	Aug 36
T (°C)	860	840	840	880
P (MPa)	100	150	170	100
SiO ₂	53.71 (0.31)*	55.11 (1.92)	58.20	55.43 (1.07)
Al ₂ O ₃	29.39 (0.06)	28.26 (0.19)	25.37	27.71 (0.45)
FeO (t)	0.60 (0.04)	0.69 (0.24)	1.15	0.42 (0.06)
MgO	N/A	N/A	0.36	N/A
CaO	11.54 (0.26)	10.83 (0.44)	9.47	9.84 (0.53)
K ₂ O	0.11 (0.02)	0.13 (0.05)	0.34	0.20 (0.07)
Na ₂ O	4.81 (0.21)	4.55 (0.50)	3.68	5.51 (0.15)
Total	100.19 (0.28)	99.58 (1.35)	98.57	99.11 (1.19)
n	4	3	1	5
An	56.65 (1.47)**	56.43 (2.51)	57.28	49.05 (1.78)
Ab	42.71 (1.51)	42.73 (2.71)	40.28	49.73 (1.73)
Or	0.64 (0.09)	0.84 (0.42)	2.45	1.22 (0.40)
Wt % H ₂ O ^c	4.9	N/A	6.0	N/A

^a Full dataset available in Appendix 2.4.

^b Starting Material: CH=Crushed HSA, SS= Sintered, SNS=Sintered (not seeded)

^c H₂O calculated using the hygrometer of Lange et al. 2009

* Data average of 'n' analyses with standard deviation in brackets.

**Uncertainty calculated using the MINERAL software (De Angelis and Neill 2012)

Table 2.5: Representative experimental pyroxene, amphibole, and biotite compositions^a

SM ^b	SS	SS	CH	SNS	SS	SS	SS
Experiment	Aug 10	Aug 19	Aug 33	Aug 37	Aug 15	Aug 16	Aug 19
Phase	Cpx ^c	Cpx	Opx	Opx	Amph	Amph	Bit ^d
T (°C)	860	820	860	840	840	820	820
P (MPa)	150	120	100	130	120	140	120
SiO ₂	51.05 (1.32)	52.68 (0.86)	53.52 (0.41)	52.37 (0.48)	46.60 (1.55)	47.66 (0.60)	40.31 (1.17)
TiO ₂	0.67 (0.19)	0.44 (0.24)	0.15 (0.06)	0.16 (0.14)	1.37 (0.22)	1.43 (0.05)	1.98 (0.37)
Al ₂ O ₃	2.66 (0.72)	1.80 (0.89)	0.94 (0.26)	7.08 (3.30)	7.48 (0.71)	7.10 (0.33)	14.68 (0.56)
FeO (t)	10.67 (1.27)	9.35 (0.31)	20.29 (0.59)	12.23 (1.96)	14.70 (0.70)	13.88 (0.75)	19.78 (2.04)
MnO	0.57 (0.07)	0.54 (0.11)	0.71 (0.14)	0.65 (0.19)	0.53 (0.08)	0.54 (0.02)	N/A
MgO	14.22 (0.23)	14.03 (0.68)	22.31 (0.33)	23.25 (2.86)	13.45 (0.17)	13.90 (0.55)	14.24 (0.60)
CaO	19.33 (1.09)	20.16 (0.71)	1.13 (0.06)	1.80 (0.97)	10.98 (0.03)	10.77 (0.12)	0.88 (0.11)
Na ₂ O	0.32 (0.04)	0.30 (0.07)	0.03 (0.03)	0.97 (0.76)	1.42 (0.13)	1.31 (0.17)	1.26 (0.24)
K ₂ O	N/A	N/A	N/A	N/A	0.31 (0.02)	0.19 (0.03)	6.96 (0.55)
Total	99.49 (0.03)	99.30 (0.39)	99.10 (0.35)	98.51 (0.34)	96.78 (0.03)	96.88 (0.68)	N/A
n	2	3	3	4	2	4	3
En	41.69 (0.48)	41.55 (1.52)	64.65 (0.94)	73.92 (1.75)	N/A	N/A	N/A
Fs	17.55 (2.01)	15.54 (0.76)	32.99 (0.96)	21.76 (1.49)	N/A	N/A	N/A
Wo	40.76 (2.48)	42.91 (1.48)	2.36 (0.12)	4.32 (2.66)	N/A	N/A	N/A

^a Full dataset available in Appendix 2.5.

^b Starting Material: CH=Crushed HSA, SS= Sintered, SNS=Sintered (not seeded)

^c Cpx = clinopyroxene; Opx = orthopyroxene; Amph = amphibole

^d Data from semi-quantitative EDS analyses. EDS software automatically normalizes all data to 100%.

2.11 REFERENCES

- Andersen, DJ, Lindsley DH, Davidson PM (1993) QUILF: A Pascal program to assess equilibria among Fe–Mg–Mn–Ti oxides, pyroxenes, olivine, and quartz. *Comput Geosci* 19:1333–1350.
- Barclay J, Carmichael ISE (2004) A hornblende basalt from western Mexico: Water-saturated phase relations constrain a pressure-temperature window of eruptibility. *J Petrol* 45(3):485–506
- Blundy J, Cashman K (2001) Ascent-drive crystallization of dacite magmas at Mount St Helens, 1980–1986. *Contrib Mineral Petrol* 140: 631–650
- Blundy J, Cashman K (2008) Reconstruction of magmatic system variables and processes. In: Putirka KD, Tepley FJ (eds) *Minerals, Inclusions and Volcanic Processes*. *Rev Mineral Geochem* 69:179–239
- Browne BL, Gardner JE (2006) The influence of magma ascent path on the texture, mineralogy, and formation of hornblende reaction rims. *Earth Planet Sci Lett* 246:161–176
- Brugger CR, Johnston D, Cashman KV (2003) Phase relations in silicic systems at one-atmosphere pressure. *Contrib Mineral Petrol* 146: 356–369
- Cervelli P, Fournier T, Freymueller J, Power J, Lisowski M, Pauk BA (2010) Geodetic constraints on magma movement and withdrawal during the 2006 eruption of Augustine Volcano. In: Power JA, Coombs ML, Freymueller JT (eds) *The 2006 eruption of Augustine Volcano, Alaska*. USGS Professional Paper 1769:427–452
- De Angelis SMH, Neill OK (2012) MINERAL: A program for the propagation of analytical uncertainty through mineral formula recalculations. *Comput Geosci*. doi.org/10.1016/j.cageo.2012.05.023

Devine JD, Gardner JD, Brack HP, Layne GD, Rutherford MJ (1995) Comparison of microanalytical methods for estimating H₂O contents of silicic volcanic glasses. *Am Mineral* 80:319–328

Geschwind CHG, Rutherford MJ (1992) Cummingtonite and the evolution of the Mount St. Helens magma system: An experimental study. *Geology* 20: 1011–1014

Ghiorso MS, Evans BW (2008) Thermodynamics of rhombohedral oxide solid solutions and a revision of the Fe-Ti two-oxide geothermometer and oxygen-barometer. *Am J Sci* 308:957–1039

Giaramita M, Day H (1990) Error propagation in calculations of structural formulas. *Am Mineral* 75:170–182

Hammer JE, Rutherford, MJ, Hildreth, W (2002) Magma storage prior to the 1912 eruption at Novarupta, Alaska. *Contrib Mineral Petrol* 144: 144–162

Holtz F, Sato H, Lewis J, Behrens H, Nakada S (2005) Experimental petrology of the 1991–1995 Unzen dacite, Japan. Part 1: Phase relations, phase composition, and pre-eruptive conditions. *J Petrol* 46:319–337

Johnston D (1978) Volatiles, magma mixing, and the mechanism of eruptions at Augustine Volcano, Alaska, Ph.D. Thesis, University of Washington, Seattle

Lange RA, Frey HM, Hector J (2009) A thermodynamic model for the plagioclase-liquid hygrometer/thermometer. *Am Mineral* 94:494–506

Larsen J, Nye C, Coombs M, Tilman M, Izbekov P, Cameron C (2010) Petrology and geochemistry of the 2006 eruption of Augustine Volcano. In: Power JA, Coombs ML, Freymueller JT (eds) The 2006 eruption of Augustine Volcano, Alaska. USGS Professional Paper 1769:335–382.

Leake B, Woolley A, Arps C, Birch W, Gilbert C, Grice J, Hawthorne F, Kisch H, Kato A, Krivovichev V, Laird J, Linthout K, Mandarino J, Maresch W, Nickel E, Rock N, Schumacher J, Smith D, Stephenson N, Ungaretti L, Whittaker E, Youzhi G (1997) Nomenclature of amphiboles: Report of the Subcommittee on Amphiboles of the International Mineralogical Association's Commission on New Minerals and Mineral Names. *Can Mineral* 35:219–246

Martel C, Schmidt BC (2003) Decompression experiments as an insight into ascent rates of silicic magmas. *Contrib Mineral Petrol* 144:397–415

Newman S, Lowenstern JB (2002) Volatile- Calc: A silicate melt–H₂O–CO₂ solution model written in Visual Basic for excel. *Comput Geosci* 28:597–604

Nielsen CH, Sigurdsson H (1981) Quantitative methods of electron microprobe analysis of sodium in natural and synthetic glasses. *Am Mineral* 66:547–552

Pichavant M, Costa F, Burgisser A, Scaillet B, Martel C, Poussineau S (2007) Equilibration Scales in Silicic to Intermediate Magmas- Implications for Experimental Studies. *J Petrol* 48(10):1955–1972

Power J, Lalla D (2010) Seismic observations of Augustine Volcano, 1970–2007. In: Power JA, Coombs ML, Freymueller JT (eds) The 2006 eruption of Augustine Volcano, Alaska. USGS Professional Paper 1769:3–40.

Power JA, Coombs ML, Freymueller JT (eds) (2010) The 2006 eruption of Augustine Volcano, Alaska. USGS Professional Paper 1769.

Prouteau G, Scaillet B (2003) Experimental constraints on the origin of the 1991 Pinatubo dacite. *J Petrol* 44(12):2203–2241

Putirka K (1999) Clinopyroxene + liquid equilibria to 100kbar and 2450 K. *Contrib Mineral Petrol* 135:151–163

Putirka KD, Mikaelian H, Ryerson F, Saw H (2003) New-clinopyroxene thermobarometers for mafic, evolved, and volatile-bearing lava compositions, with applications to lavas from Tibet and the Snake River Plain, Idaho. *Am Mineral* 88:1542–1554

Ratajeski K, Sisson T (1999) Loss of iron to gold capsules in rock-melting experiments. *Am Mineral* 84:1521–1527

Reed SJB (2005) *Electron microprobe analysis and scanning electron microscopy in geology*. Cambridge University Press, Cambridge

Roman, DC, Cashman KV, Gardner CA, Wallace PJ, Donovan JJ (2006) Storage and interaction of compositionally heterogeneous magmas from the 1986 eruption of Augustine Volcano, Alaska. *Bull Volcanol* 68(3):240–254

Rutherford MJ, Devine JD (1996) Pre-eruption pressure-temperature conditions and volatiles in the 1991 dacitic magma of Mount Pinatubo. In: Newhall CG, Punongbayan RS (eds) *Fire and Mud: Eruptions and lahars of Mount Pinatubo, Philippines*. University of Washington Press, Seattle, 751–766

Rutherford MJ, Devine JD (2003) Magmatic conditions and magma ascent as indicated by hornblende

phase equilibria and reactions in the 1995–2002 Soufrière Hills Volcano magma. *J Petrol* 44(8):1433–1454

Rutherford M, Sigurdsson H, Carey S, Davis A (1985) The May 18, 1980 eruption of Mount St. Helens 1. Melt composition and experimental phase equilibria. *J Geophys Res* 90(B4):2929–2947

Scaillet B, Evans B (1999) The 15 June 1991 eruption of Mount Pinatubo. I. Phase equilibria and pre-eruption P-T-fO₂-fH₂O conditions of the dacite magma. *J Petrol* 40(3):381–411

Sisson T, Grove T (1993) Experimental investigations of the role of H₂O in calc-alkaline differentiation and subduction zone magmatism. *Contrib Mineral Petrol* 113:143–166

Sisson TW, Ratajeski K, Hankins WB, Glazner AF (2005) Voluminous granitic magmas from common basaltic sources. *Contrib Mineral Petrol* 148:635–661

Steiner AR, Browne BL, Nye CJ (2012) Quenched mafic inclusions in ≤ 2200 years B.P. deposits at Augustine Volcano, Alaska. *Int Geology Rev* 54: 1241-1270

Tilman, MR (2008) An investigation of symplectite-rimmed olivine and magmatic processes during the 2006 eruption of Augustine Volcano, Alaska. M.S. Thesis, University of Alaska Fairbanks, Fairbanks

Vallance JW, Bull KF, & Coombs ML (2010) Pyroclastic flows, lahars, and mixed avalanches generated during the 2006 eruption of Augustine Volcano. In: Power JA, Coombs ML, Freymueller JT (eds) *The 2006 eruption of Augustine Volcano, Alaska*. USGS Professional Paper 1769: 219–268

Webster JD, Mandeville CW, Goldoff B, Coombs M, Tappen C (2010) Augustine Volcano—The influence of volatile components in magmas erupted A.D. 2006 to 2,100 years before present. In: Power JA, Coombs ML, Freymueller JT (eds) *The 2006 eruption of Augustine Volcano, Alaska*. USGS Professional Paper 1769:383–423

CHAPTER 3:

Experimental insights into the formation of heating- and decompression-induced amphibole reaction rims and implications for shallow-level magmatic processes at arc volcanoes³

3.1 ABSTRACT

The focus of this chapter is the use of novel experiments to examine the differences between amphibole reaction rims created by heating or decompression. The experiments employed calc-alkaline andesite and dacite starting materials at H₂O vapor saturated conditions and buffered at $f_{O_2} = \text{Re-ReO}_2$ (~Ni-NiO+2). Heating experiments equilibrated at 870°C and 140 MPa for 24 hours before single-step isobaric heating to 880°C, 900°C, or 920°C. Decompression experiments equilibrated at 840°C and 150 MPa for 24 hours, before single-step isothermal decompression to 75, 65, or 55 MPa. Duration at the final conditions ranged between 3–48 hours (heating) and from 12–144 hours (decompression). Heating-induced rims form at higher growth rates ($< 0.25 \times 10^{-7}$ – 1.6×10^{-7} cm/s) than observed from the decompression experiments ($< \sim 1.7 \times 10^{-8}$ cm/s). The thicknesses of decompression-induced rims formed at 65 MPa for >50 hours (> 25 μm) overlap with heating-induced rim thicknesses formed at 880°C for ≤ 36 hours or at 900°C–920°C for ≤ 12 hours. Decompression-induced rims primarily contain orthopyroxene and Fe-Ti oxides, with little or no clinopyroxene or plagioclase present. Heating-induced rims contain two pyroxenes, Fe-Ti oxides, and plagioclase in varying amounts. Measurements of the sizes and number densities of crystals that form within the reaction rims reveal differences that appear to be specific to the mechanism of formation. For example, decompression generally produces smaller microlite sizes (< 8 μm) and N_A 's ($> \sim 50,000$ mm⁻²), while heating produces rims with larger grain sizes (> 5 μm) and lower N_A 's ($< \sim 50,000$ mm⁻²). In addition, negative correlations between crystal nucleation and growth rates with time make it possible to estimate the duration of heating events in natural samples. A comparison between decompression-induced

³ Henton De Angelis, S., Larsen, J. & Coombs, M. & Dunn, A. Experimental insights into the formation of heating- and decompression-induced amphibole reaction rims and implications for shallow-level magmatic processes at arc volcanoes. Prepared for submission to *Contributions to Mineralogy and Petrology*

reaction rims formed under different oxygen fugacities reveals growth rates that are a factor of 1.5–4 higher at $f_{O_2} = \text{Re-ReO}_2$ than they are at $\text{NNO}+0.5$ to 1 log units. In conclusion, quantitative textural and mineralogical data (e.g. mineral modes, N_A and crystal area fractions) are crucial for the correct classification of amphibole reaction rims.

3.2 INTRODUCTION

Disequilibrium textures are commonplace in subduction zone magmas, which often undergo complex paths of mixing and episodic ascent on their way to the surface. Amphibole, a common phenocryst phase in intermediate-composition arc magmas, is generally stable at pressures >100 MPa (~ 4 km), in melts that contain at least 4 wt% H_2O (Rutherford and Hill 1993), and at temperatures generally less than ~ 880 – 900 °C. Notably, reaction rims of anhydrous minerals (referred to hereafter as ‘microlites’) form during destabilization of hydrous amphibole phenocrysts. Decompression-induced dehydration is one important mechanism that leads to amphibole breakdown, and measurements of reaction-rim thicknesses are widely used to estimate ascent rates for subduction zone magmas (e.g. Rutherford and Hill 1993; Devine et al. 1998; Luhr, 2002; Nicholis and Rutherford, 2004; Browne and Gardner, 2006; McCanta et al. 2007; Coombs et al. 2012). In addition to decompression-induced dehydration, rims on amphibole can also form due to heating if temperatures exceed the thermal stability of the mineral.

Past studies of natural amphibole reaction rims classified ‘decompression’ and ‘heating’ mechanisms largely based on microlite textures and mineralogy (Garcia & Jacobson 1979; Rutherford and Hill 1993; Devine et al. 1998; Murphy et al. 2000; Rutherford & Devine 2003). Decompression-induced reaction rims are generally described as thin (~ 1 – 40 μm), with microlite grain sizes of 1 – 30 μm , and primarily composed of orthopyroxene, plagioclase, and Fe-Ti oxides. In contrast, heating rims are described as thicker (generally >200 μm), coarser grained (30 – 300 μm grain size), and clinopyroxene-rich. However, only a small number of studies have experimentally confirmed these classifications (e.g. Browne and Gardner 2006; Buckley et al. 2006; Plechov et al. 2008).

Past experimental work has focused on decompression-induced breakdown reactions in order to

provide calibrations for magma ascent rates (Rutherford and Hill 1993; Rutherford and Devine 2003; Browne and Gardner 2006). Less than 7% of all experiments from prior studies yielded data on heating-induced amphibole breakdown reactions. Only Buckley et al. (2006) described the mineralogy of reaction rim microlites and compared their results with a mass balance approach. Browne and Gardner (2006) presented a comprehensive and quantitative account of how reaction rim textures change with variable disequilibrium conditions.

This study focuses on the first experiments to compare the growth rates, mineralogy, and microlite textures of heating- vs. decompression-induced amphibole reaction rims. The experiments demonstrate that heating-induced rims can grow rapidly and thus suggest that thickly rimmed or pseudomorphed amphiboles found in natural samples may form over remarkably short timescales (<48 hours). Contrary to previous classifications, this study shows that heating-induced experimental reaction rims have textural and mineralogical similarities with those formed during decompression experiments. The implications of these results are that natural amphibole reaction rims may not be simply classified on the basis of semi-quantitative textural and mineralogical observations. Instead, measurements quantifying modal mineral abundances, crystal number densities and calculations of crystal nucleation and growth rates are crucial. With an increase in experimental data applied to the problem, it may be possible to infer the cause of the breakdown rim formation from those parameters. However, experimental calibrations of reaction rates are best applied to natural systems when independent observations are available to reliably infer the mechanisms of their formation.

3.3 METHODOLOGY

Heating experiments were conducted using finely ground, fused glass derived from high-silica andesite pumice produced during the 2006 eruption of Augustine Volcano, Alaska, and seeded starting powders with ~20 unreacted amphibole phenocrysts. Decompression experiments were conducted using crushed dacite from the 1989–90 eruption of Redoubt Volcano, Alaska (Browne and Gardner 2006). All experiments were H₂O vapor saturated, buffered at fO_2 of Re-ReO (RRO~Ni-NiO+2), and conducted using

TZM alloy or externally heated, Rene-style, Waspaloy cold-seal pressure vessels. Heating experiments were initially held at 870°C and 140 MPa for 24 hours before isobaric heating to 880°C, 900°C, or 920°C. Likewise, the decompression experiments initially thermally equilibrated at 840°C and 150 MPa (Browne and Gardner 2006) for 24 hours before isothermal decompression to 75, 65, or 55 MPa. Experiments were heated or decompressed in a single step before being held for 3–48 hours (heating) or 12–144 hours (decompression) at the final conditions.

Major oxide compositional data from experimental amphiboles was collected using a Cameca SX50 electron microprobe with a focused (1–5 μm), 15kV, 10nA beam. BSE images and X-ray maps of 1 to 5 amphibole reaction rims per experiment were collected using an EDS equipped scanning electron microscope set to a 25kV accelerating voltage, large spot size (~65–80), and a 10 mm working distance. Image processing was performed using the ImageJ software package. Reaction rim thickness was measured at 5 to 20 different locations around the grains, from which average thicknesses were calculated. The mineral phase, size, aspect ratio, and position within the rim for <10 to >200 microlites per reaction rim were recorded. Reaction rim microlite size is represented by the Feret's diameter (FD), or the longest distance between any two points around the boundary of the crystal, as measured by ImageJ. Crystal number densities (N_A) and microlite area fraction measurements were used to calculate crystal growth (G), and nucleation rates (I) were calculated following the method of Brugger and Hammer (2010).

3.4 RESULTS

3.4.1 Reaction Rim Mineralogy

Reaction rims have formed during all experiments in this study. Reaction rims show systematic changes in mineralogy and textural complexity with increasing time at disequilibrium (Figure 3.1, Figure 3.2), the magnitude of disequilibrium, and with different forcing mechanisms (heating vs. decompression).

All heating-induced reaction rims contain Fe-Ti oxides and pyroxene (Figure 3.2). Pyroxene is invariably the primary phase (57.4 to >90 modal %) and includes both ortho- and clinopyroxene varieties. However, at constant temperature, the abundance of clinopyroxene consistently decreases with increasing

time, from >70 modal % at 3-hours to 0 modal % at 48 hours. This is most apparent in the 900°C and 920°C series. Minor mineral phases include plagioclase (0 ~15 modal %) and fragments of amphibole in short duration (3 hour) experiments at 880 and 900°C. The modal abundance of oxides increases with time in all temperature series.

Decompression-induced reaction rims contain 71.3 to 82.8 modal % orthopyroxene (Figure 3.2). Clinopyroxene is observed at one set of experimental conditions (840°C, 65 MPa, and 114 hours) but it is volumetrically minor at 0.34 modal %. Fe-Ti oxides range from 17.2 to 25.6 modal %, and plagioclase ranges from 1 to 3.2 modal %. Decompression-induced reaction rims show much less mineralogical variability with experimental duration than do heating-induced reaction rims.

3.4.2 Reaction Rim Textures

3.4.2.1 *Thicknesses, Growth Rates, and Microlite Size*

Heating-induced reaction rims increase in thickness with both the magnitude of imposed disequilibrium (degree of heating) and experimental duration (Figure 3.3A). The thickest reaction rims form during heating to 920°C (from a starting temperature of 870 °C). Complete breakdown to pseudomorphs occurs after 12 hours at 920°C and 24 hours at 900°C, with the exception of an unusually large grain yielding a small remnant core and a >200µm thick rim after 48 hours at the final temperature. The slowest rim growth occurs in experiments heated to 880°C. However, between 36 and 48 hours the reaction rate increases greatly and by 48 hours at this temperature, all amphiboles form pseudomorphs.

Correspondingly, heating-induced rim growth rates increase with final temperature (Figure 3.3B). The highest growth rates of 1.6×10^{-7} cm/s occur in experiments held at 920°C for 3 hours. At 6 hours the rates fall to 9.1×10^{-8} cm/s, but by 12 hours they rise again to 1.3×10^{-7} cm/s. At 900°C growth rates are > 45% lower but their progression with time shows the same pattern. At 900°C, the growth rates remain relatively low ($< 1 \times 10^{-7}$ cm/s) for at least 12 hours before rising again to a high of $\sim 1.3 \times 10^{-7}$ cm/s. At 880°C growth rates start at $\sim 0.7 \times 10^{-7}$ cm/s, similar to those at 900°C in the shortest duration experiments, and then they decrease $< 0.25 \times 10^{-7}$ cm/s. They remain low compared to the higher temperature experiments for

up to 36 hours before increasing rapidly to 1.1×10^{-7} cm/s at hold times >36 hours.

In decompression experiments held at 55 and 75 MPa, the reaction rims (Figure 3.3D) never exceed $15 \mu\text{m}$. Rims formed by decompression to a final pressure of 65 MPa are significantly thicker and exceed $20 \mu\text{m}$ by ~ 50 hours and are $>25 \mu\text{m}$ by 144 hours. While thicker than some heating-induced rims, the decompression rims form over much longer timescales due to much lower growth rates, peaking at $\sim 1.7 \times 10^{-8}$ cm/s when held for 50 hours at 65 MPa. However, even at their peak, the growth rates observed are up to a factor of 4 faster than those reported by Browne and Gardner (2006) at similar final pressures. Both studies utilized the same starting material, but in this study an oxygen fugacity ~ 1 to 1.5 log units higher was utilized.

Heating-induced reaction rims contain a wide range of microlite sizes although few exceed $20 \mu\text{m}$ (Figure 3.3C). Microlites in decompression-induced reaction rims show less variation and are typically $<8 \mu\text{m}$ in size (Figure 3.3F). There is no systematic relationship between microlite size and the degree of heating/decompression outside of stability, reaction timescale, or the position of a microlite within each reaction rim.

3.4.2.2 Reaction Rim Crystal Number Densities, Nucleation, and Growth Rates

In general, reaction rims created in both the heating and decompression experiments exhibit a negative correlation between crystal number density per unit area (N_A) and average microlite size (FD; Figure 3.4A), with decompression-induced reaction rims anchoring the high N_A ($\sim 10^5 \text{ mm}^{-2}$) and low microlite size ($<8 \mu\text{m}$) end of the data range, and the heating experiments producing lower N_A s and larger crystals size textures. There is a weak negative correlation between reaction rim thicknesses and N_A .

When crystal nucleation rates are calculated (as N_A over average crystal size, divided by the experimental timescale at the final conditions), there is a negative correlation between the calculated nucleation rates and time for heating experiments (Figure 3.4C), with nucleation rates highest in the short duration experiments. In contrast, the variation in nucleation rates with time is more subdued for decompression experiments. The most robust kinetic observation is that the growth rate of crystals within

the reaction rims appears to decrease with increasing experimental duration (Figure 3.4D), with the shortest experiments (primarily heating experiments) showing the highest crystal growth rates (Figure 3.4D).

3.5 DISCUSSION

3.5.1 Initiation of Reaction Rim Formation

There are three modes of reaction rim initiation: 1) Crystallization of anhydrous minerals from the melt (Figure 3.5A); 2) Physical shedding of amphibole from the host phenocryst (Figure 3.5B); and 3) Zones of pyroxene (most commonly clinopyroxene) still attached to the amphibole host (Figure 3.5C). Two possible explanations exist for the formation of attached pyroxene zones: 1) solid state phase transition (e.g. Wartho 1995), or 2) pyroxene overgrowth (e.g. Streck 2008). The observed pyroxene zones contain the continuation of cleavage traces and cracks from the host amphibole and on this basis formation by pyroxene overgrowth is rejected. Wartho (1995) used a photo emission electron microscope apparatus to view in real time the solid-state transition of tschermakitic hornblende to oxyhornblende and then to an ‘amphiboloid’ phase with a clinopyroxene structure during heating from 750–1000°C. These experiments were conducted in a vacuum, and the exact duration of experiments is not disclosed but is on the scale of hours. As with the clinopyroxene zones observed in the experiments, the ‘amphiboloid’ phase retains original amphibole features such as cleavage traces.

In heating experiments, the different modes of reaction initiation are observed not only within the same experiments but also at different points around the same amphiboles. This suggests that the processes controlling the initiation of breakdown are independent of the magnitude of disequilibrium and/or of the amphibole composition. Likely, amphibole shedding is encouraged where cracks or pronounced cleavage planes in the host phenocrysts weaken its physical strength. Modes of formation may also be related to local melt conditions, such as the melt viscosity in the immediate vicinity of the amphibole boundary. Higher viscosity conditions (perhaps resulting from variable glass compositions and crystallinities) may inhibit physical amphibole breakdown (Browne and Gardner 2006; Coombs et al. 2012). In such cases, solid-state transition may be the easiest way for amphiboles to react to changing temperature conditions.

3.5.2 Separating Heating from Decompression-Induced Rim Formation

3.5.2.1 Mineralogy

The mineralogy of amphibole reaction rims has been a key component used to classify the causes of reaction rim formation. Most studies of natural amphiboles (e.g. Rutherford and Devine 2003) reported that orthopyroxene dominates over clinopyroxene in decompression-induced reaction rims. Prior experimental results also suggest that decompression-induced reaction rims can be identified by the total or near total absence of clinopyroxene (e.g., Browne and Gardner 2006). However, mass balance and X-ray mapping observations later revealed that clinopyroxene exists in significant quantities in natural amphibole rims previously described as containing orthopyroxene only (Figure 3.2; Buckley et al. 2006). A recent study by Plechov et al. (2008) provides convincing evidence of natural amphiboles with orthopyroxene-only reaction rims although they attribute the formation of these rims to isobaric heating, not decompression, yet, it is also commonly suggested that heating-induced reaction rims are clinopyroxene rich (e.g. Rutherford and Devine 2003; Browne and Gardner 2006). This study represents the first to attempt to quantify experimental reaction rim mineralogy through the use of high-resolution X-ray maps, and these support prior observations that decompression-induced rims are clinopyroxene-free. However, contrary to prior studies, in this study heating-induced reaction rims contain both pyroxenes in varying amounts. This is consistent with the conclusions of Chapter 2, which suggest that in the Augustine system, heating-induced reaction rims contain both pyroxenes in significant quantities.

There is a relationship between heating-induced rim mineralogy and the experimental duration (Figure 3.2). With increasing time at the final temperature, the modal abundances of clinopyroxene fall (Figure 3.2). In pseudomorphs formed during the longest-duration experiments, only orthopyroxene is identified. This suggests that phase relations within an individual system are the primary control on rim mineralogy. For Augustine Volcano high-silica andesites, clinopyroxene is not stable above 880°C (Chapter 2) and thus clinopyroxene is a meta-stable phase in the experimental reaction rims that forms upon initial breakdown during heating above 880°C. Due to its significant calcium content, it may form

early during the process of amphibole decomposition, thus explaining its presence in short duration experiments (3–12 hours). However, clinopyroxene eventually dissolves into the melt because it is unstable at the final experimental conditions. Further, in this study differences in amphibole composition do not control reaction rim mineralogy. Amphiboles in this study show little compositional variability, both within and between phenocrysts. Moreover, there is no correlation between variations in any amphibole major oxides with variations in the proportions of clino- and orthopyroxene in the reaction rims. Although this study provides the first published data set of this kind, further experimental work on compositions relevant to a broad range of volcanic systems is needed to more completely understand the relative stabilities and abundances of ortho- and clinopyroxene in both heating and decompression-induced reaction rims.

3.5.2.2 *Textures and Growth Rates*

For similar experimental durations, heating produces thicker reaction rims and faster growth rates (Figure 3.3). However, a region of overlap exists between reaction rims from long duration decompression (>50 hours) and shorter duration heating experiments (3–12 hours at 900–920°C and 3–36 hours at 880°C). The sizes of microlites in those decompression reaction rims are consistently <10 µm. In comparison, a large number of heating reaction rims from those short duration experiments also contain microlites that are on average < 10 µm.

In general, these new experimental results agree with previous studies and confirm that decompression-induced rims are typically thinner and finer grained than heating-induced ones. However the new data clearly demonstrate that the ranges of rim thicknesses and grain sizes used to classify heating versus decompression rims from natural samples may fall within the region of overlap observed in the long duration decompression and shorter duration heating experiments. For example, over 80% of heating-induced reaction rims in this study are <40 µm in thickness. Thus, a short-term heating event due to magma mixing in a natural magma could produce the same texture and thickness of rim as decompression during relatively slow magma ascent. If similar rims are observed in nature, they might be mistakenly classified as decompression-induced based on their relatively small thicknesses and fine-grained texture (e.g. Murphy et

al. 2000; Rutherford and Devine 2003). Thus, caution is urged when using measurements of amphibole reaction rim thicknesses alone to classify the provenance of natural amphibole textures

3.5.2.3 Discrimination by Rim Microlite Number Densities

As demonstrated above, it may be difficult to classify natural rims according to their forcing mechanisms on the basis of individual parameters alone. However, one method that shows promise is to compare microlite number densities as a function of average microlite size in the rim (Figure 3.3A). Experimental results predict that decompression produces microlite sizes that are typically $<5 \mu\text{m}$ and N_A 's $> \sim 50,000 \text{ mm}^{-2}$ regardless of time at the final pressure. This indicates rapid nucleation of anhydrous phases in the reaction rim and limited growth over the observed experimental timescales. In contrast, the heating-induced rims typically produce coarser grained ($>12 \mu\text{m}$) rims with lower N_A ($< \sim 50,000 \text{ mm}^{-2}$) than in the decompression rims. Some overlap exists where microlite sizes range from $5\text{--}12 \mu\text{m}$ and N_A 's range from $30,000\text{--}80,000 \text{ mm}^{-2}$ (Figure 3.3A). The addition of data points from future experimental work may determine whether the distinction between heating- and decompression-induced reaction rims can be made with confidence.

3.5.3 Estimating Timescales of Disequilibrium

Previous experimental results (e.g., Browne and Gardner 2006) demonstrate that different combinations of disequilibrium magnitude and duration can produce indistinguishable reaction rims. The results suggest that for heating-induced reaction rims, experimentally derived crystal nucleation and growth rates may represent reliable proxies for heating duration estimates in nature (Figure 3.4C and D). The reliability of this method is contingent on the rapid quenching of the magma soon after the heating event. Additional experiments are needed to refine calibrations, particularly for crystal nucleation rates, which exhibit more scatter with time (Figure 3.4C). Unfortunately there is little systematic change in crystal nucleation or growth rates with magnitudes of heating, and as such distinguishing the degree to which a magma may

have been heated on the basis of amphibole reaction rims remains elusive. If the degree of heating is known with accuracy from independent methods (e.g. Fe-Ti oxide re-equilibration timescales; Devine et al. 2003), then it may be possible to estimate heating durations on the basis of reaction rim thicknesses alone, assuming the natural heating event ends as the samples are quenched during eruption. For decompression reaction rims, variations in crystal growth rates, and (especially) crystal nucleation rates with time, are minor and not always systematic. As a result they currently cannot be used for estimating timescales of decompression.

3.5.4 Observations of Reaction Rim Kinetics

Kinetic studies of disequilibrium (cooling or decompression) plagioclase crystallization have linked changing textural features (e.g. N_A , aspect ratio, and microlite size) as a function of experimental duration to nucleation vs. growth-dominated crystallization regimes (e.g., Muncill and Lasaga 1988; Hammer and Rutherford 2002). Nucleation rates are highest when the degree of disequilibrium is high, while growth rates are highest when the degree of disequilibrium is low (e.g. Brugger and Hammer 2010). High N_A and small crystal sizes are indicative of nucleation-dominated crystallization during reactions in which the system is forced far from equilibrium over short timescales (Hammer and Rutherford 2002). In contrast, reduced N_A and larger crystal sizes indicate a growth-dominated crystallization regime in a system reacting to a smaller degree of forcing away from equilibrium. Nucleation and growth rates typically show separate but overlapping curves as a function of degree of (effective) undercooling, whereby growth rates increase as nucleation rates fall.

Experimental amphibole reaction rims in this study show alternative patterns. In heating rims, crystal nucleation (I) and growth rates (G) are both high following short durations at the final conditions, and fall together as experimental durations increase (Figure 3.4C and D). This could mean that almost all nucleation is accomplished early, and that in longer experiments this early nucleation “event” is averaged over longer and longer experimental timescales. At the same time, crystal growth is rapid early in the breakdown process, but slows with time. There is also little systematic change in crystal sizes or N_A with

different degrees of thermal disequilibrium. The same relationships are observed for decompression rims, although the relationships are not as strong. Decompression rims, which contain the highest N_A values and smallest microlite sizes (Figure 3.4A), should yield the highest crystal nucleation rates (Brugger and Hammer 2010). However, calculated values are intermediate to those for heating rims, and are an order of magnitude lower than the highest nucleation rates calculated for heating-induced breakdown reaction rims.

Plagioclase nucleation studies have focused on single-mineral crystallization from the melt (e.g. Brugger and Hammer 2010). In contrast, amphibole reaction rim formation is a complex process. For example, in some cases it might involve amphibole dissolution followed by the nucleation and growth of multiple minerals (e.g. Rutherford and Hill 1993; Browne and Gardner 2006). In others, it might involve the solid-state phase transition of amphibole (e.g. Wartho 1995) to pyroxene followed by growth-dominated crystallization. Thus the measured crystal number densities, crystal nucleation rates, and crystal growth rates in the experiments reflect the sum of multiple different reactions and processes. It is therefore not surprising that the relationships seen in the experimental data for amphibole reaction rims do not agree with the models based on plagioclase crystallization kinetics. In future work it may be interesting to differentiate between the N_A , G , and I properties of different mineral phases within reaction rims in order to better understand the kinetics of reaction rim formation.

3.5.5 Effects of Changing Oxygen Fugacity

The effects of oxidation on reaction rim formation rates was tested using decompression experiments. A small number of the single-step decompression experiments performed utilized the same 1989–1990 Redoubt Volcano dacite starting material that was employed in the Browne and Gardner (2006) study. Browne and Gardner (2006) buffered experiments at an fO_2 of $NNO+0.5$ to 1 log unit. In contrast, the fO_2 of experiments in this study was fixed at RRO ($\sim NNO+2$ log units). In agreement with Browne and Gardner (2006), reaction rim growth rates peak at 65 MPa (~ 35 MPa below amphibole barometric stability). However, growth rates are significantly elevated in experiments buffered at RRO . At final pressures of 65 MPa growth rates are 1.5–4 times faster, while at 55 MPa growth rates are approximately a

factor of 2 faster. These results highlight the sensitivity of amphiboles to changes in magmatic conditions and the individuality of different volcanic systems. As a result, experimental calibrations must be used with caution when applied to different volcanic systems.

3.5.6 Combined Disequilibrium Conditions: Simultaneous Heating and Decompression

Given the complexity of volcanic systems, amphiboles can be exposed to multiple disequilibrium conditions either concurrently or in succession prior to eruption. As a result, natural amphibole reaction rims may reflect multiple processes, such as decompression followed by shallow level oxidation (e.g. Genareau and Clarke 2010). In other cases magma ascent could initiate rim formation, but release of latent heat during decompression-induced crystallization of the groundmass could then act to heat the amphiboles in the ascending magma. Indeed, Blundy et al. (2006) cite evidence for heating during magma ascent of up to 100°C. The results show that heating of amphibole by much smaller degrees can produce reaction rims on a scale of hours. Thus, while the rims may start to form because of decompression, they may grow and mature texturally because of simultaneous heating and evidence for their decompression origin would be overprinted and obscured by the effects of heating.

3.5.7 Formation of Pseudomorphs

Pseudomorphs form very quickly in heating experiments. Even at temperatures of 880°C, <10°C above the amphibole thermal stability boundary (Chapter 2), pseudomorphs form after only 48 hours. Some represent the natural culmination of rim thickening, when the inward progression of reaction rim formation ceases due to the exhaustion of host amphibole. In contrast, other pseudomorphs form rapidly after decomposition of the entire grain. For example, in the 880°C heating experiments pseudomorphs form suddenly and rapidly between 36 and 48 hours, following relatively slow growth in the preceding 36 hours. The results of the 880°C heating experiments suggest that amphibole can resist small degrees of thermal destabilization for a small amount of time, for the most part maintaining their structure and only breaking down along the

outer boundary with the melt. As time progresses the amphibole becomes less able to resist the effects of increased temperature. Eventually the system reaches a critical threshold after which breakdown occurs throughout the phenocryst. This theory is consistent with reaction rim growth rates (Figure 3.3B), which increase with time. Breakdown progresses along planes of weakness as demonstrated by the alignment of microlites along cleavage planes in many pseudomorphs (Figure 3.5D). The maintenance of the host amphibole shape and quickness of this reaction suggest that it reflects solid-state phase transition to pyroxene (e.g. Wartho 1995) rather than amphibole dissolution and re-nucleation of microlites.

3.5.8 Implications for Natural Augustine Amphibole Reaction Rims

This new experimental data can be used to make tentative interpretations regarding the genesis of Augustine Volcano 2006 amphibole reaction rims. Type 1 reaction rims (those <50 μm thick; Chapter 1) are closest to the textures of experimental decompression reaction rims. However, they contain significant clinopyroxene (in contrast to experimental decompression reaction rims). Therefore, while decompression remains the most likely process driving their formation, it is also possible that some or all represent short duration (<36 hours) heating. Type 2 reaction rims (50–80 μm thick; Chapter 1) are texturally and mineralogically consistent with heating-induced formation over timescales <48 hours. Type 3 reaction rims (>80 μm thick; Chapter 1) have mineral modes consistent with heating. However, average reaction rim thicknesses and microlite sizes exceed those of most heating experiments (although total conversion to pseudomorphs has not occurred). These rims also contain lower crystal number densities than any experimental reaction rims. It is possible that these reaction rims are the result of the slow, long-term decomposition of amphiboles stuck along conduit walls below amphibole barometric stability. Technically this would make these decompression-induced reaction rims, albeit ones formed in a sluggish kinetic environment over a scale of months to years, rather than days to weeks. However, the abundance of clinopyroxene in these rims goes against this theory.

3.6 CONCLUSIONS

This study represents the first comprehensive experimental study of heating-induced amphibole breakdown reaction rims. The new experiments show textural and mineralogical differences between heating-induced and decompression-induced amphibole reaction rim formation. Heating-induced reaction rims form more rapidly, resulting in growth rates approximately 1 order of magnitude faster ($< 0.25 \times 10^{-7} - 1.6 \times 10^{-7}$ cm/s) compared with the decompression experiments ($\sim 1.7 \times 10^{-8}$ cm/s). Decompression reaction rim thicknesses (up to 25 μm) overlap with heating-induced reaction rim thicknesses formed at 880°C for <36 hours or 900°C to 920°C for <12 hours. As a result, distinguishing the forcing mechanism on the basis of reaction rim thickness and microlite sizes alone may not be possible. However, it may be possible to distinguish heating- from decompression-induced reaction rims by more in-depth textural and mineralogical observations.

In contrast with heating-induced reaction rims, current experimental results show that decompression-induced rims contain little or no clinopyroxene. The results of this study suggest that the mineralogies of heating-induced reaction rims are a function of phase stability within an individual volcanic system. However, additional experimental data are needed at a broader range of conditions to confirm these findings. Without further experiments on a range of volcanic products, this also remains a possibility for decompression-induced reaction rims.

It may be possible to use the relationship between microlite number densities and microlite sizes within the rims to distinguish heating- from decompression-induced reaction rims. Decompression generally produces microlites <10 μm in size and with N_A 's $> \sim 50,000 \text{ mm}^{-2}$, indicating rapid nucleation of anhydrous phases in the reaction rim and limited growth over the observed experimental timescales. However, some overlap with heating-induced reaction rims occurs where microlite sizes range between 5–12 μm and N_A 's are from 30,000 – 80,000 mm^{-2} . The addition of data points from future experimental studies will help to refine this boundary region. For heating-induced reaction rims, durations of heating can be estimated from crystal nucleation and growth rates.

Reaction rims from higher f_{O_2} experiments buffered at RRO ($\sim \text{NNO}+2$) are greater than those at

NNO + 0.5 to 1 log units (Browne and Gardner 2006) by a factor of 1.5 to 4. Future investigations of natural amphibole reaction rims from relatively oxidized volcanic systems should employ experimentally calibrated reaction rates at the appropriate fO_2 when assessing timescales of decompression.

There are clear textural and mineralogical similarities between experimental heating-induced rims and natural reaction rims. In the past, heating-induced reaction rims may have been mistakenly attributed to decompression processes. A better way to decipher the causes of natural rim formation is to take a quantitative approach based on characterization of the rim textures and mineralogies, as used here on this new experimental data set. Relying on estimates of reaction rim thickness and microlite sizes alone may not be sufficient to uniquely characterize the provenance of natural amphibole reaction rims. With further research on experimental and natural reaction rims, it may be possible to estimate both the magnitudes of thermal disequilibrium and the heating durations required to form a given reaction rim. This would require more detailed quantification of textural and mineralogical data (e.g. modal mineral abundances, crystal number densities, crystal nucleation and growth rates) as a function of different experimental conditions and timescales to correctly classify amphibole reaction rims. The results of this study also highlight the fact that there are significant differences in amphibole reaction rates observed between different experimental conditions (e.g., fO_2) and compositions (e.g. Rutherford and Hill 1993; Browne and Gardner 2006; this study). Thus, application of experimental results to natural systems must be approached with caution, and extrapolation of the experimental results to different natural systems could create errors in the modeling of amphibole reaction timescales.

3.7 ACKNOWLEDGEMENTS

This work was supported by a grant from the National Science Foundation (NSF EAR 0911694).

3.8 FIGURES

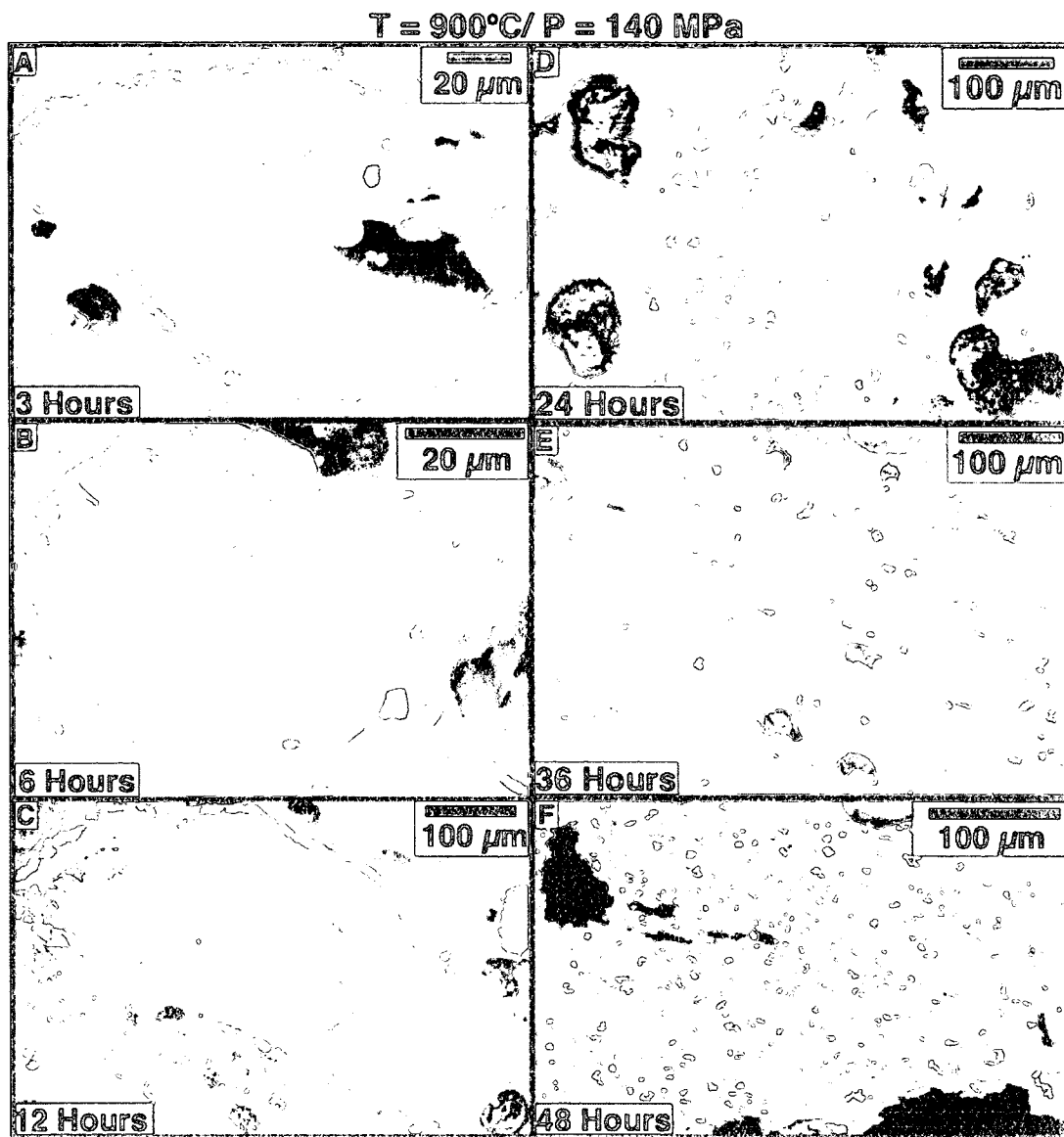


Figure 3.1 Composite X-Ray maps of experimental amphibole reaction rims. Reactions depicted were all formed at a temperature of 900°C and at a pressure of 140 MPa. Successive images reflect increasing experiment durations: A) 3 hours; B) 6 hours; C) 12 hours; D) 24 hours; E) 36 hours; F) 48 hours. Different colors depict different minerals. Exact shading varies between images but in general: blue = glass; purple = plagioclase; red = magnetite; yellow = ilmenite; 'olive' green = amphibole; green = orthopyroxene; yellow/green = clinopyroxene.

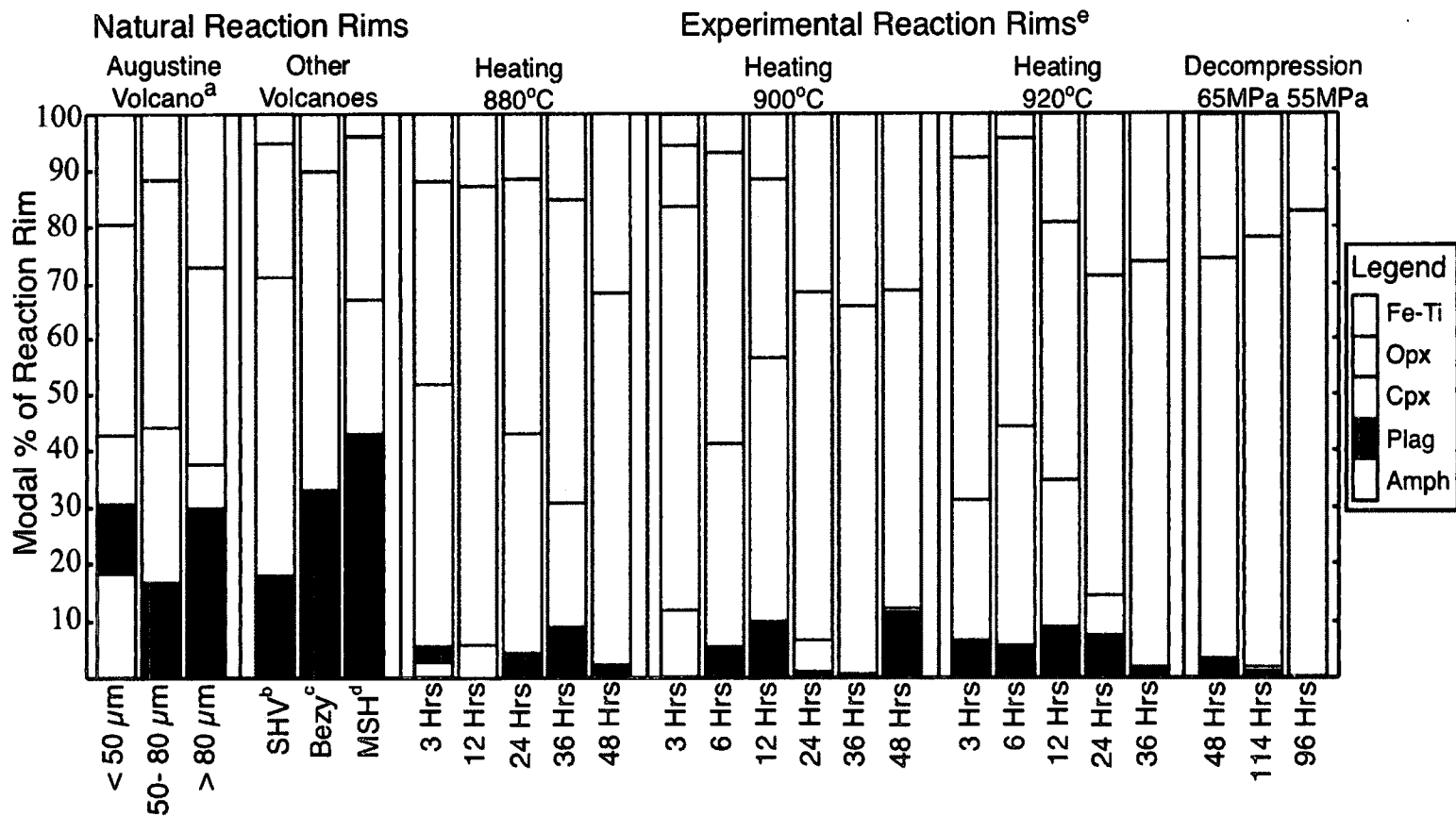


Figure 3.2 Natural and experimental amphibole reaction rim mineralogies. Natural reaction rim data from Augustine Volcano (Chapter 1) and Soufriere Hills Volcano, Montserrat (SHV; Buckley et al. 2006), and experimental reaction rim data represents directly measured modal percentages from the analysis of X-Ray maps. Natural reaction rim data from Bezyminyany (Bezy) Volcano (Plechov et al. 2008) and Mount St Helens (MSH; Rutherford and Hill 1993) represent mass balance calculations. Full data in Appendix 3.1.

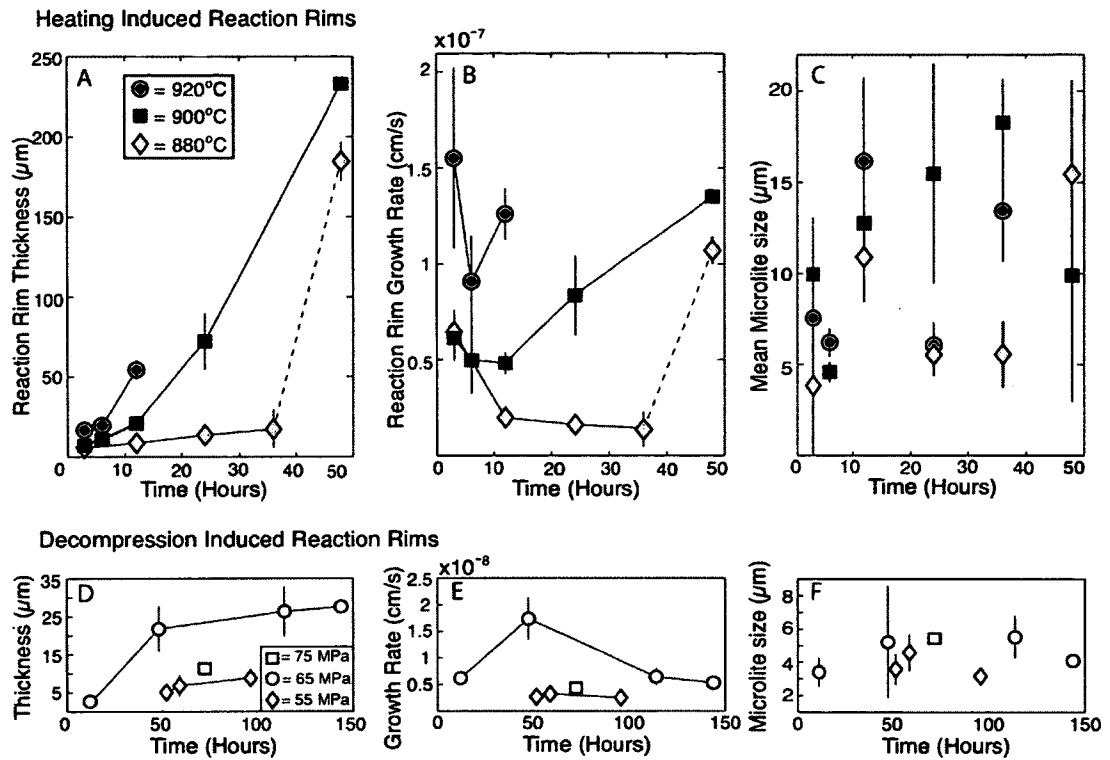


Figure 3.3 Average reaction rim thicknesses, growth rates, and microlite sizes. Panels A-C represent heating experiments. Panels D-F represent decompression experiments. Note that growth rate values are expressed as $\times 10^{-7}$ and $\times 10^{-8}$ (Panels B and E). Error bars represent 1-sigma uncertainty on the average values for 2–5 reaction rims per experiment. Full data in Appendices 3.1 and 3.2.

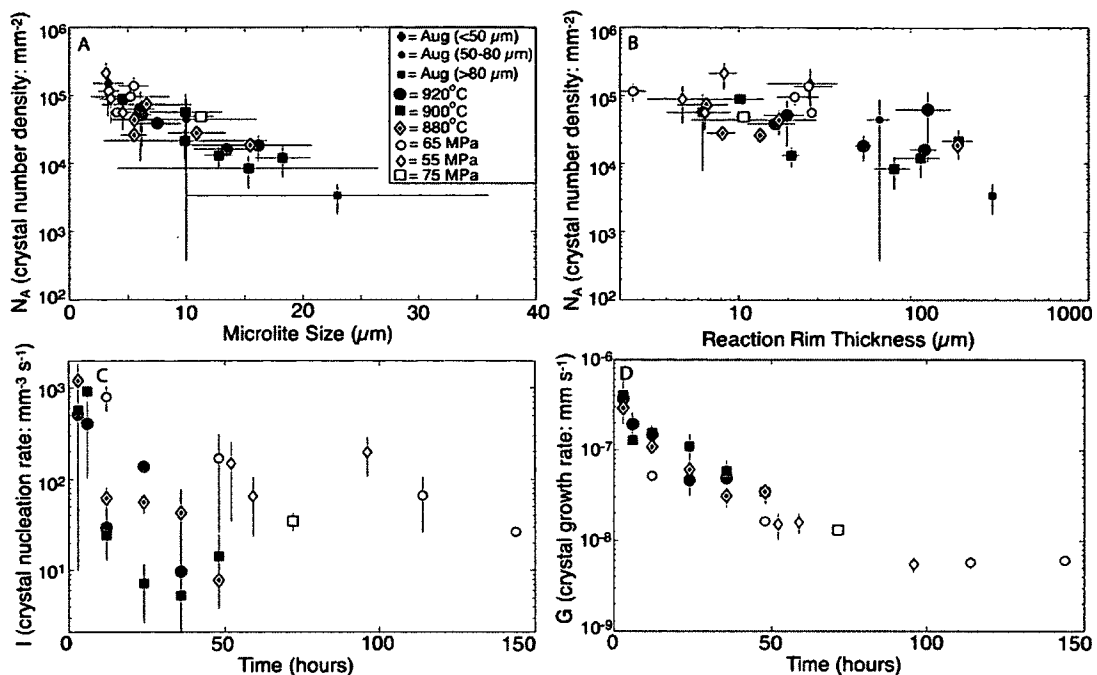


Figure 3.4 Kinetic features of experimental and natural reaction rims. A) Crystal number density (N_A ; mm^{-2}) as a function of average microlite size (μm); B) Crystal number density (N_A ; mm^{-2}) as a function of average reaction rim thickness (μm); C) Crystal nucleation rates (I ; $\text{mm}^{-3} \text{ s}^{-1}$) as a function of experimental time (hours); D) Crystal growth rates (G ; mm s^{-1}) as a function of experimental time (hours); Experimental data characterized by degree of disequilibrium. Natural amphibole data from Augustine Volcano (Aug) categorized by average reaction rim thickness. Note the log scales on most axes. Error bars represent 1-sigma uncertainty on the average values for 2–5 reaction rims per experiment. In many cases uncertainty is smaller than symbols. Full data in Appendix 3.3.

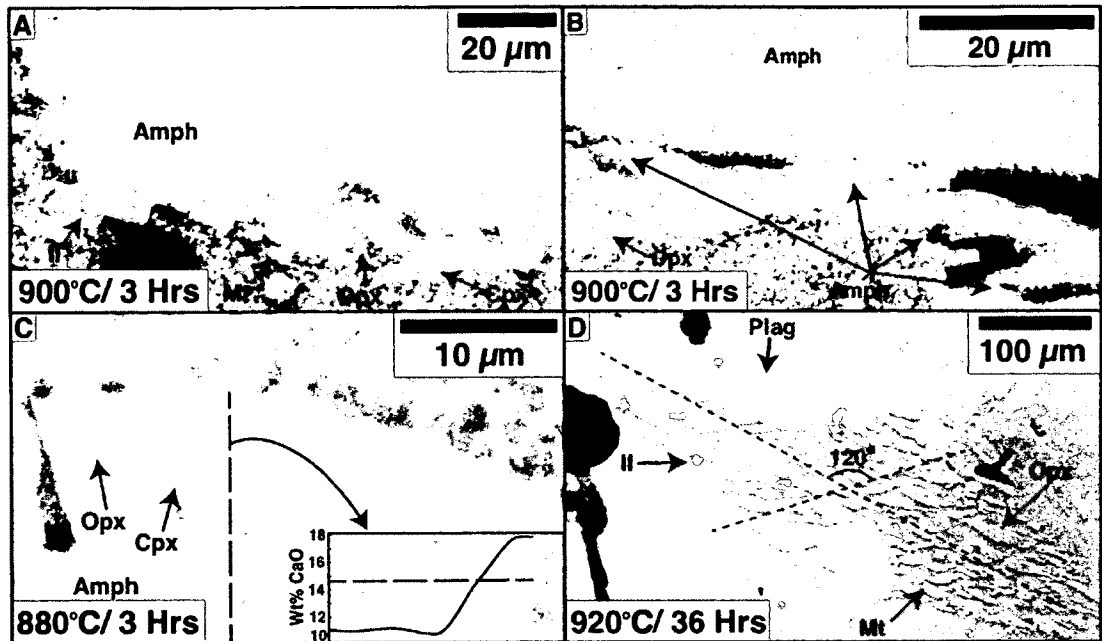


Figure 3.5 Composite X-Ray maps of notable textural features. Panels A-C depict different modes of rim initiation. Panel D depicts pseudomorph formation along lines of weakness in the host amphibole. Different colors depict different minerals. Exact shading varies between images but in general: blue = glass; purple = plagioclase; red = magnetite; bright yellow = ilmenite; 'olive' green/brown = amphibole; green = orthopyroxene; pale yellow/green = clinopyroxene.

3.9 REFERENCES

Blundy J, Cashman K, Humphreys M (2006) Magma heating by decompression-driven crystallization beneath andesite volcanoes. *Nature* 443:76-80.

Browne BL, Gardner JE (2006) The influence of magma ascent path on the texture, mineralogy, and formation of hornblende reaction rims. *Earth Planet Sc Lett* 246 (3–4):161–176.

Brugger CR, Hammer JE (2010) Crystallization kinetics in continuous decompression experiments: Implications for interpreting natural magma ascent processes. *J Petrol* 51(9):1941–1965.

Buckley VJE, Sparks RSJ, Wood BJ (2006) Hornblende dehydration reactions during magma ascent at Soufrière Hills volcano, Montserrat. *Contrib Mineral Petrol* 151(2):121–140.

Coombs M, Sisson T, Bleick H, Henton S, Nye C, Payne A, Cameron C, Larsen J, Wallace K, Bull K (2012) Andesites of the 2009 eruption of Redoubt Volcano, Alaska, *J Volcanol Geoth Res*, Special Issue on the 2009 Redoubt Eruption, In Press.

Devine JD, Rutherford MJ, Gardner JE (1998) Petrologic determination of ascent rates for the 1995–1997 Soufrière Hills Volcano andesite magma. *Geophys Res Lett* 25(19), 3673–3676.

Devine JD, Rutherford MJ, Norton GE, Young SR (2003) Magma storage region processes inferred from geochemistry of Fe-Ti oxides in andesitic magma, Soufrière Hills Volcano, Montserrat, W.I. *J Petrol* 44(8):1375-1400.

Garcia MO, Jacobson SS (1979) Crystal clots, amphibole fractionation and the evolution of calc-alkaline magmas. *Contrib Mineral Petrol* 69:319–327.

Genarreau KD, Clarke AB (2010) Determining magma ascent rates from overprinted amphibole breakdown textures: The Soufrière Hills 2003 lava dome. American Geophysical Union, Fall Meeting 2010, Abstract V43B-2377.

Hammer JE, Rutherford MJ (2002) An experimental study of the kinetics of decompression-induced crystallization in silicic melt. *J Geophys Res* 107(B1, 2021), 10.1029/2001JB000281.

Luhr JF (2002) Petrology and geochemistry of the 1991 and 1998-1999 lava flows from Volcan de Colima, Mexico: implications for the end of the current eruptive cycle. *J Volcanol Geoth Res* 117:169-194.

McCanta MC, Rutherford MJ, Hammer JE (2007) Pre-eruptive and syn-eruptive conditions in the Black Butte, California dacite: Insight into crystallization kinetics in a silicic magma system. *J Volcanol Geoth Res* 160:263–284.

Muncill GE, Lasaga AC (1988) Crystal-growth kinetics of plagioclase in igneous systems: Isothermal H₂O-saturated experiments and extension of a growth model to complex silicate melts, *Am Mineral* 73:982-992.

Murphy MD, Sparks RSJ, Barclay J, Carroll MR, Brewer TS (2000) Remobilization of andesite by intrusion of mafic magma at the Soufrière Hills Volcano, Montserrat, West Indies. *J Petrol* 41(1):22–42.

Nicholis MG, Rutherford MJ (2004) Experimental constraints on magma ascent rate for the Crater Flat volcanic zone hawaiite. *Geology* 32:489-492.

Plechov P, Tsai A, Shcherbakov V, Dirksen O (2008) Opacitization conditions of hornblende in Bezymianny volcano andesites (March 30, 1956 eruption). *Petrology* 16(1):19–35.

Rutherford M, Devine J (2003) Magmatic conditions and magma ascent as indicated by hornblende phase equilibria and reactions in the 1995–2002 Soufrière Hills magma. *JPetrol* 44(8):1433–1454.

Rutherford M, Hill P (1993) Magma ascent rates from amphibole breakdown: An experimental study applied to the 1980–1986 Mount St. Helens Eruptions. *J Geophys Res* 98(B11):19,667–19,685.

Streck MJ (2008) Mineral textures and zoning as evidence for open system processes. *RevMin Geochem* 69:595-622.

Wartho JA (1995) Photo-emission electron microscopy (PEEM) heating investigation of a natural amphibole sample. *Mineral Mag* 59:121-127.

CHAPTER 4:

MINERAL: A program for the propagation of analytical uncertainty through mineral formula recalculations⁴

4.1 ABSTRACT

MINERAL (MINeral ERror AnaLysis) is a MATLAB® based program that performs mineral formula recalculations and calculates the error on formula unit cations through the propagation of analytical uncertainties. The program is focused on 9 common mineral groups. Other minerals are accommodated through a generic routine in which users designate the number of cations and oxygens in the desired formula. Additional functionalities provide users with a range of mineral-appropriate output options. Recalculations and uncertainty calculations include site assignments for multi-site cations (e.g. tetrahedral and octahedral Al in mafic minerals), partitioning of Fe²⁺ and Fe³⁺, and calculations of mol fractions of end members. Until now, performing full propagation of uncertainty through mineral formula recalculations was labour intensive and, for users unfamiliar with statistical notation or techniques, a significant computational challenge. The lack of precedent set by previous studies has made it accepted practice within the discipline to not provide recalculated uncertainty information. This oversight prevents analysts from assessing the quality of their data and interpretations in a robust and quantitative manner. This automated toolbox renders the process fast and simple.

4.2 KEYWORDS: Error, uncertainty, mineral recalculation

⁴ De Angelis, S. H. & Neill, O. K. (2012). MINERAL: A program for the propagation of analytical uncertainty through mineral formula recalculations, *Computers and Geosciences* **48**, 134-142

4.3 INTRODUCTION

The quantification and reporting of analytical uncertainty is an essential aspect of scientific data presentation because the magnitude of uncertainty can directly influence data interpretation. Error estimation is a function of uncertainties inherent in acquiring raw data, as well as in applied post-processing procedures. Rigorous propagation of uncertainty through all steps of data processing requires specific and sometimes complex calculations based on statistical methods.

In geology and petrology, major-element compositions of solid phases, normally determined by electron probe micro-analysis (EPMA), are commonly reported in two ways: a) wt% abundances of elemental or oxide components; and b) atomic proportions within a mineral formula, referred to as 'formula cations' or 'atoms per formula unit' (a.p.f.u.). Despite the automated pre-processing commonly associated with EPMA data (e.g. Donovan et al. 2007), elemental abundances in wt% are often considered the 'raw' results. Typically, users will convert these to wt% oxides, where oxygen is calculated stoichiometrically. Where results are calculated from averaging 'n' data points, uncertainty is reported as the standard deviation on 'n' analyses. On individual data points, uncertainty can be calculated based on either the counting statistics of each individual measurement or multiple analyses of a "bench" standard.

To report data as a.p.f.u., analysts are required to apply mineral-specific recalculations to their data. These calculations are used to determine the proportions of elements in each crystallographic position and are based on normalizing oxide percentages against an ideal chemical formula. The recalculation process involves multiple steps. Different methods exist for the estimation of uncertainty on recalculated data. The two simplest methods are: 1) to estimate uncertainties from the standard deviation on 'n' analyses of a bench standards or 2) to perform formula recalculations on 'n' analyses of a sample and then calculate the average and associated standard deviation. Alternatively, uncertainty of formula cations can be calculated by propagating uncertainty through each step of the recalculation using a standard statistical method. In some cases the different methods may yield similar (or functionally identical) results, while in others uncertainties can vary by up to an order of magnitude (Table 4.1).

While the most robust method statistically, propagating uncertainty through mineral formula re-

calculations using standard error analysis techniques is complex. Each step in the recalculation procedure involves an associated calculation for error propagation. This process cannot be performed for individual oxides independently, as both the composition and uncertainty on a cation is a function of the composition and uncertainty of all input oxides.

Published a.p.f.u. results typically do not include uncertainties, due to two primary issues. First, propagation of uncertainty through multi-step, mineral specific recalculations of a mineral formula is laborious, and analysts may be unwilling and/or unable to perform the necessary calculations. Second, the lack of precedent set by previous studies has made it accepted practice within the discipline to not provide recalculated uncertainty information.

A.p.f.u. data is often used in models to infer geological processes (e.g. Anderson et al., 1993; Holland & Blundy, 1994; Putirka et al., 2003). Lack of uncertainty data is an oversight that prevents analysts from quantitatively assessing the quality of their data. Performing uncertainty calculations not only conforms to standard scientific protocols but also helps to identify 'bad' data (e.g. outliers, mixed analyses, compositionally heterogeneous crystals) and confirm the validity of conclusions. For example, relationships between tetrahedral Al (in the crystallographic T site) and A-site alkalis (Na + K; Figure 4.1a) and tetrahedral Al and B-site (the crystallographic M4 site) Ca in a volcanic amphibole dataset (Figure 4.1b) both show positive correlations, indicating a relationship between the variables. The relatively small error bars (in both X and Y; Figure 4.1c) strengthen this conclusion with respect to tetrahedral Al and A-site alkalis. However, analytical uncertainty accounts for a significant portion of the total variation in B-site Ca (Figure 4.1d).

MINERAL (MINeral ERror AnaLysis) is a new MATLAB® based program that provides mineral formula recalculations combined with the associated propagation of the analytical uncertainties. Methods are based on the work of Giannarita and Day (1990). However, additional features have been added to provide users with greater flexibility in data reporting. Many programs exist to recalculate wt% data into formula unit cations. Some generalized programs can be used to recalculate the formula of multiple minerals e.g. CALCMIN (Brandelik, 2009) and HYPER-FORM (De Bjerg et al., 1992). Other programs are mineral specific e.g. AMPH CLASS (Esawi, 2004) and PROBE AMPH (Tindle and Webb, 1994) for

the recalculation of amphibole analyses; ILMAT (Lepage, 2003) for the recalculation of magnetite and ilmenite; and PX-NOM (Sturm, 2002) for the recalculation of pyroxene analyses. MINERAL provides a rapid method for the recalculation of multiple common minerals. However, its strength lies in the fact that it is the first tool to incorporate the associated uncertainty propagation calculations. As these are performed concurrently with the standard recalculations, no additional time is needed to perform uncertainty propagation. While an understanding of the underlying calculations is strongly recommended, MINERAL is designed to allow users with little or no experience operating MATLAB® and/or performing mineral formula recalculations and uncertainty propagation to undertake both with ease.

4.4 REVIEW OF PAST WORK

Giaramita and Day (1990) provide equations for the recalculation of mineral formulae and for propagating the associated uncertainties through these calculations. Two methodologies are presented: full or partial uncertainty propagation. Full uncertainty propagation includes the calculation of a covariance matrix. The covariance matrix is omitted in the partial routine. For both methods, different equations are provided depending on the type of cation under consideration, e.g. single or multi-valence, single or multi-site. A full description of the equations provided by Giaramita and Day (1990), and used in MINERAL, are provided in Appendices 4.1 and 4.2

Giaramita and Day (1990) tested their method on amphibole (hornblende), pyroxene (augite) and feldspar (bytownite) datasets. They conclude that: (1) While the uncertainty on major oxides is a good approximation for uncertainty for single valence, single-site cations, the same is not for true multi-valence, multi-site cations; (2) The absolute differences between uncertainties calculated from full and partial error propagation are not large, but relative differences may be significant. For high precision work, multi-site cations, or multi-valence cations, it is advisable to conduct full error propagation. For example, Giaramita and Day (1990) show that counting errors of just 0.5 % relative on FeO in amphibole and augite can be magnified to 2.25% and 7.26% for Fe³⁺ calculations, respectively; (3) Errors in structural formulae are magnified or reduced compared to uncertainties on oxides. Magnification depends on the composition of

the mineral, the normalization scheme employed, the structural formula, the magnitude of uncertainty on oxides, and the contribution from covariance.

4.5 MINERAL (MINeral ERror AnaLysis)

The implementation of the Giaramita and Day (1990) method is long and labour intensive (especially if full covariance is calculated) and, for users unfamiliar with statistical notation or techniques, may present a significant challenge. This automated toolbox provides for fast and simple implementation of their method along with added functionality that provides users with a range of output options appropriate to the mineral under consideration.

MINERAL is a toolbox that is run using the MATLAB® platform. The current version of MINERAL includes options for the recalculation of 9 common mineral groups: pyroxenes, feldspars, olivine, spinels, ilmenite, amphiboles, micas, garnets, and epidotes. The program also includes a generic recalculation function that incorporates user-defined recalculation parameters. Users are able to select the type of uncertainty propagation, the type of uncertainty reported, and, where appropriate, the method of mineral recalculation. MINERAL can be operated from a simple Graphical User Interface (GUI; Figure 4.2), from the command line using a wrapper script, or by embedding any of MINERAL functions into users' own MATLAB® scripts. Full operating procedures can be found in the MINERAL user manual, provided with the program.

The input and output of MINERAL depends on the type of error propagation required. For full error propagation, users input 'n' analyses from which average oxide composition, standard deviations, and a covariance matrix are calculated. For partial error propagation, users input a single set of wt% oxide values and an associated (pre-calculated) uncertainty for each. Input data are passed through the error propagation equations to yield recalculated and site-assigned cations and the associated uncertainties. Additional functionality is provided on a mineral-by-mineral basis.

Giaramita and Day (1990) suggest that the primary advantage to performing partial error propagation is simplicity. With MINERAL, the application of either method is straightforward. However,

partial error propagation has other benefits. While full uncertainty propagation is preferred for multi-valence or multi-site cations, or when high precision is required, it restricts the input uncertainty to the standard deviation of 'n' analyses. Some users may feel that analytical uncertainty is better expressed as the standard deviation calculated from working standards or counting statistics and applied uniformly to each analysis. Uncertainties of this kind can only be handled using the partial error propagation method, which allows the input of a user-defined uncertainty on major oxides, rather than the calculation of one by MINERAL itself.

For each calculation, MINERAL must know the molecular weights of all input oxides, and for this reason, the program is currently restricted to 12 of the most common major oxides: SiO₂, TiO₂, Al₂O₃, FeO, MnO, MgO, CaO, Na₂O, K₂O, Cr₂O₃, V₂O₃, NiO, as well as F and Cl for amphibole. Output for full uncertainty propagation includes calculated average oxides, calculated cations, cation uncertainties, cation sum, and any mineral specific-outputs. Output for partial uncertainty propagation includes calculated cations, cation uncertainties, cation sum, and any mineral-specific outputs. For each type of error propagation, users are able to select how uncertainties are reported, e.g. absolute 1σ , 2σ , 3σ , or σ^2 (variance). Users may view other calculation outputs, e.g. calculated covariance matrices, by editing the desired MATLAB® script (see user manual for details).

MINERAL imports data from .csv files. These files can be created in standard spreadsheet programs. Data must be input in a specific manner, as explained in detail in the user manual. MINERAL output is written to both .txt files and to MATLAB® .mat structures. The provision of MATLAB® structures makes it easier for users to continue using MATLAB® for further data manipulation or plotting. The .txt files can be read in common spreadsheet software.

Users wishing to recalculate amphibole can choose between normalization to 15 or 13 cations. For normalization to 13 cations: $13 = \text{Si} + \text{Ti} + \text{Al} + \text{Fe} + \text{Mn} + \text{Mg}$ in the T and C (M1, M2, M3) sites. This method excludes Ca from the C sites and Fe²⁺, Mn and Mg from the B (M4) site. In contrast, for normalization to 15 cations: $15 = \text{Si} + \text{Ti} + \text{Al} + \text{Fe} + \text{Mn} + \text{Mg} + \text{Ca}$ in the T, C, and B sites. Users should refer to the literature for the more appropriate choice of calculation type (Cosca et al., 1991; Leake et al., 1997; Robinson et al., 1982; Schumacher, 2007).

The stoichiometric calculation of Fe^{2+} and Fe^{3+} in minerals such as amphibole and pyroxenes is standard practice and this is reflected in the calculations offered by MINERAL. However, numerous studies have shown stoichiometric methods to be unreliable and prone to significant uncertainty, especially in amphiboles where incomplete occupancy of the hydroxyl site is common (Al'meev et al., 2002; Blundy and Holland, 1990; Cosca et al., 1991; Hawthorne and Oberti, 2007). For calcic amphibole, it is generally thought that 13-cation normalization is the most accurate stoichiometric methods of calculating Fe^{2+} and Fe^{3+} , while for Fe-Mg-Ca amphibole, 15-cation normalization is more appropriate (Al'meev et al., 2002). However, those requiring highly accurate data on $\text{Fe}^{2+}/\text{Fe}^{3+}$ partitioning should consider direct measurement by wet chemistry techniques or Mössbauer spectroscopy (e.g. Blundy and Holland, 1990; Cosca et al., 1991). MINERAL users should be aware of the pitfalls of stoichiometric calculations and recognize that uncertainties on Fe^{2+} and Fe^{3+} represent minimum error estimates.

Most MINERAL recalculations are based on normalization to cations except for the amphibole-15, epidote, and mica routines, which are normalized to formula oxygen. This is consistent with other commonly used programs for the recalculations of mineral formulae e.g. CALCMIN (Brandelik, 2009); ILMAT (Lepage, 2003); PROBE AMPH (Tindle and Webb, 1994). The generic routine allows users to decide between recalculation normalized to oxygen or cations.

Additional functionalities, above and beyond the calculations of Giaramita and Day (1990), primarily include the calculation of mol fraction mineral end members (and their associated uncertainties). For ease of calculation, and regardless of the type of uncertainty propagation used to calculated cation errors, the errors on end members are calculated without the use of the covariance term. Calculated variables and end members for each mineral were chosen to allow users the greatest flexibility in reporting their results. However, users should be aware that not all variables are appropriate for all recalculations, despite their presence in the output. For example, the mol fraction ulvospinel calculated by the spinel routine is only appropriate for magnetite spinels. Similarly, the end members reported for the complex mineral groups, e.g. epidote and garnet, are not exhaustive and users should be aware that other, rarer end members also exist. Users should take care to report the most appropriate variables for their analyses. For some users, this may mean discarding end members, and site assigned cations, and reporting the total

cations (and associated uncertainties) only.

4.5.1 Mineral Specific Considerations

4.5.1.1 Feldspar

Feldspar end member calculations include mol fraction An (anorthite; Ca end member), Ab (albite; Na end member), and Or (orthoclase; K end member). Fe is reported as Fe(t). As only Fe^{3+} is incorporated into the feldspar structure, Fe(t) represents $\text{Fe}^{3+}(\text{t})$. The conversion of FeO (Fe^{2+}) to Fe_2O_3 (Fe^{3+}) is performed within MINERAL; users should ensure that the original data input is in wt% FeO.

4.5.1.2 Olivine

Olivine end member calculations include mol fractions of Fo (forsterite; Mg end member), Fa (fayalite; Fe end member), Te (tephroite; Mn end member), CaOl (calcium olivine end members), and Lei (liebenbergite; Ni end member). All Fe is assumed to be Fe^{2+} .

4.5.1.3 Pyroxene

Pyroxene end member calculations include those appropriate for both calcic and sodic pyroxenes. Users should decide which classification scheme is the most appropriate. Calcic end members include mol fraction En (enstatite; Mg end member), Fs (ferrosilite; Fe end member), and Wo (wollastonite; Ca end member). Sodic end members include mol fraction Aeg (aegirine; Na/Fe end member), Jd (jadite; Na/Al end member), and Di (diopside; Ca/Mg end member). In addition to total Fe and Al, Fe^{2+} , Fe^{3+} , Al^{iv} , and Al^{vi} (tetrahedral and octahedral Al) cation proportions and uncertainties are calculated. The calculation of FeO and Fe_2O_3 oxide wt% is based on stoichiometric and charge balance criteria (Droop, 1987).

4.5.1.4 *Spinel*

Spinel end member calculations include those for both magnetite spinels and for the spinel group. Users should decide which classification scheme is the most appropriate. Mol fractions are calculated for Chr (chromite group), Mag (magnetite group), and Spl (spinel group). Further, the mol fraction Usp (ulvospinel) is calculated. Usp is only appropriate for magnetite spinels; mol fraction Mag (magnetite) may be calculated as 1-Usp. In addition to Fe(t), Fe²⁺ and Fe³⁺ cations and cation uncertainties are calculated. The calculation of FeO and Fe₂O₃ oxide wt% is based on stoichiometric and charge balance criteria (Carmichael, 1967).

4.5.1.5 *Ilmenite*

The ilmenite routine includes the calculation of mol fraction Ilm; mol fraction Hem (hematite) may be calculated as 1-Ilm. In addition to Fe(t), Fe²⁺ and Fe³⁺ cations and cation uncertainties are calculated. The calculation of FeO and Fe₂O₃ oxide wt% is based on stoichiometric and charge balance criteria (Carmichael, 1967).

4.5.1.6 *Amphibole*

In addition to total Fe, Al, Na, Fe²⁺, Fe³⁺, Al^{iv}, and Al^{vi}, Na (B site) and Na (A site) cations (and their uncertainties) are calculated. The halogens (F and Cl) are calculated, although H₂O is not. The calculation of FeO and Fe₂O₃ oxide wt% is based on stoichiometric and charge balance criteria (Droop, 1987). Users are referred to Leake et al. (1997) for amphibole classification nomenclature. End member calculations may be added to MINERAL at a later date.

4.5.1.7 Garnet

Given the large number of garnet varieties, only the most commonly found end members are calculated by MINERAL. Pyrope (Al in y-site) garnet end members included are almandine, pyrope, and spessartine. Ugrandite (Ca in X-site) garnet end members included are andradite, grossular, and uvarovite. In addition to Fe(t), Fe²⁺ and Fe³⁺ cations and uncertainties are calculated. The calculation of FeO and Fe₂O₃ oxide wt% is based on stoichiometric and charge balance criteria (Droop, 1987).

4.5.1.8 Epidote

Given the large number of epidote end members, only the most commonly found are calculated by MINERAL. For monoclinic epidote users should refer to the end members: epidote (Fe end member), clinozoisite (Al end member), and tawmawite (Cr end member; Franz & Liebscher, 2004). For zoisite, the orthorhombic polymorph of clinozoisite, users should refer to the calculated mol fractions of Fe, Mn, and V. Users are referred to Franz & Liebscher (2004) for a full discussion of the nomenclature of epidote group minerals. As only Fe³⁺ is incorporated into the epidote structure, all Fe is converted to Fe₂O₃ and Fe(t) represents Fe³⁺(t). The conversion of FeO (Fe²⁺) to Fe₂O₃ (Fe³⁺) is performed within MINERAL; users should ensure that the original data input is in wt% FeO.

4.5.1.9 Mica

Mica is a complex mineral for which there are a number of recalculation methods. MINERAL performs its calculations based on normalization to 22 oxygens per formula unit. Halogens (F and Cl) are recalculated, although H₂O is not. This method assumes that all Fe is present as FeO. Cation normalization methods that calculate the distribution of FeO and Fe₂O₃ are available, but are only appropriate when there are no vacancies in the octahedral sites (Yavuz & Oztas, 1997). The option to recalculate micas based on cation normalization may be added to MINERAL at a later date. Al^{iv}, Al^{vi} and their uncertainties are calculated.

Users are referred to Rieder et al. (1998) for amphibole mica nomenclature. End member calculations will be added at a later date.

4.5.1.10 *Generic*

The generic routine allows users to calculate uncertainties on minerals not specifically included in MINERAL. Cation calculations for all input elements are made, However, no site assignment calculations are included. In addition to Fe(t), Fe²⁺ and Fe³⁺ cations and cation uncertainties are calculated. The generic calculation function cannot be used if unusual mineral-specific changes need to be made to the recalculation scheme. For example, recalculating feldspar through the generic routine would be problematic, as the generic routine does not convert FeO(t) to Fe₂O₃(t). Similarly, the generic routine could not be used for the recalculation of amphibole, as recalculations of amphibole exclude Ca, Na, and K from the cation sum.

4.6 TESTING MINERAL

4.6.1 Mineral Formula Recalculations

To test the formula recalculations performed by MINERAL, results were compared with those derived from published results and other published recalculation programs (Figure 4.3). There is excellent correlation between the results from MINERAL and other published sources. For example, calculated X_{ILM} values for ilmenite were equal to 7 or more decimal places (d.p.) (relative differences < 0.001 %). Calculated An values for plagioclase were identical to 6 or more d.p. (relative differences < 0.01 %). Calculated X_{Fo} values for olivine were identical to 4 or more d.p. (relative differences \leq 0.1 %). The results from amphibole comparisons depend on valency and on the number of sites in which a cation resides. However, in general calculated values are identical to 3-4 or more d.p. (relative differences predominantly \leq 0.5 %). Given that a.p.f.u results are rarely reported to greater than 3 d.p., the MINERAL calculations are

functionally identical to other calculation tools. Minor variations are likely the result of differences in the number of significant figures used for the input molecular weights of each oxide, as well as differences between programs in rounding and the number of significant digits that are carried through the calculations.

4.6.2 Formula Uncertainty Calculations

MINERAL is tested by attempting to reproduce the results of calculations reported in Giaramita and Day (1990). For partial error propagation, recalculated formula unit cations show relative differences between 0.00 and 4.17% (Table 4.2). However, in absolute terms the results are identical to 4 or more significant figures. Given that oxide and cation data are rarely reported to more than 3 decimal places, the results are functionally identical. The relative differences between calculated uncertainties are higher, ranging between 0.00 and 12.0%. However, in absolute terms, the results are identical to 3 or more significant figures.

For full propagation, Giaramita and Day (1990) provide the calculated covariance matrix (with data rounded to 2 decimal places) but not the original oxide data (as required by MINERAL). As a result, the full error propagation results cannot be realistically compared. However, complex spreadsheets set up to test the calculations (in preparation for the writing of MINERAL) indicate that the Giaramita and Day (1990) results can be reproduced to levels similar to those seen for the partial error propagation routine (Table 4.2). In summary, the results reported by Giaramita and Day (1990) and those calculated by MINERAL are close, but not identical. As with the recalculated cations themselves, these minor variations likely result from differences in the number of significant figures used for the molecular weights of each oxide and also in the way the results of various stages of the calculations have been rounded.

Giaramita and Day (1990) highlighted the particular importance of uncertainty propagation for multi-site and multi-valence cations. MINERAL results are consistent with this observation. For example, Figure 4.4 shows a.p.f.u. values for total Fe, Fe³⁺ and Fe²⁺ in a number of magnetite analyses plotted against their calculated error (reported as relative standard deviation). When recalculated values are reported as total Fe, relative uncertainty is less than 1%. However, when the distribution of Fe²⁺ and Fe³⁺ is calculated, uncertainties are magnified by up to 3-fold.

4.7 CONCLUSION

Giaramita and Day (1990) conclude that for minerals containing single-valence, single-site cations, uncertainties on measured oxides provides a good approximation for uncertainties on recalculated cations. Several subsequent studies have cited this as a reason to ignore full uncertainty propagation calculations (e.g. Agrosi et al, 2002). However, the provision of an automated system for performing uncertainty propagation renders the complexity and time-intensive nature of the calculations irrelevant and eliminates the need for approximations. The MINERAL package will continue to be developed and expanded. It is likely that developments will include amphibole classification, plotting tools, adoption of the covariance term in the calculation of end member error, and addition of other mineral groups such as sulphides and carbonates.

MINERAL is designed to be easily accessible for users with no prior knowledge of either MATLAB® or statistical analyses. The program transforms calculations of analytical uncertainty on formula unit cations from a time-consuming effort, ignored by most, to a simple and fast procedure. With the main barrier to performing these calculations removed, it is hoped that a precedent for reporting uncertainty on recalculated data will be developed. In the long term this will help to encourage a culture of more robust evaluation of data quality in geology and petrology.

4.8 ACKNOWLEDGEMENTS

The authors wish to extend their gratitude to Marty Giaramita and Howard Day for their support of this project, and Ken Severin for providing formative ideas and computational assistance. The authors also thank John Brady, Silvio De Angelis, Ronni Grapenthin, Julia Hammer, Eric Hellbrand, Pavel Izbekov, Jessica Larsen and Franz Meyer for providing data and critical comments on early versions of MINERAL. Pavel Pletchov and Thomas Shea provided constructive reviews that helped to improve the manuscript and software. The authors wish to acknowledge the following grants that helped support this work: NSF EAR 0911694 (S.M.H. De Angelis through J.F. Larsen), NSF PIRE – Kamchatka Award OISE

0530278 (O.K. Neill through P.E. Izbekov and J.C. Eichelberger), and NSF CAREER Award EAR04-49888 (O.K. Neill through J.E. Hammer).

4.9 FIGURES

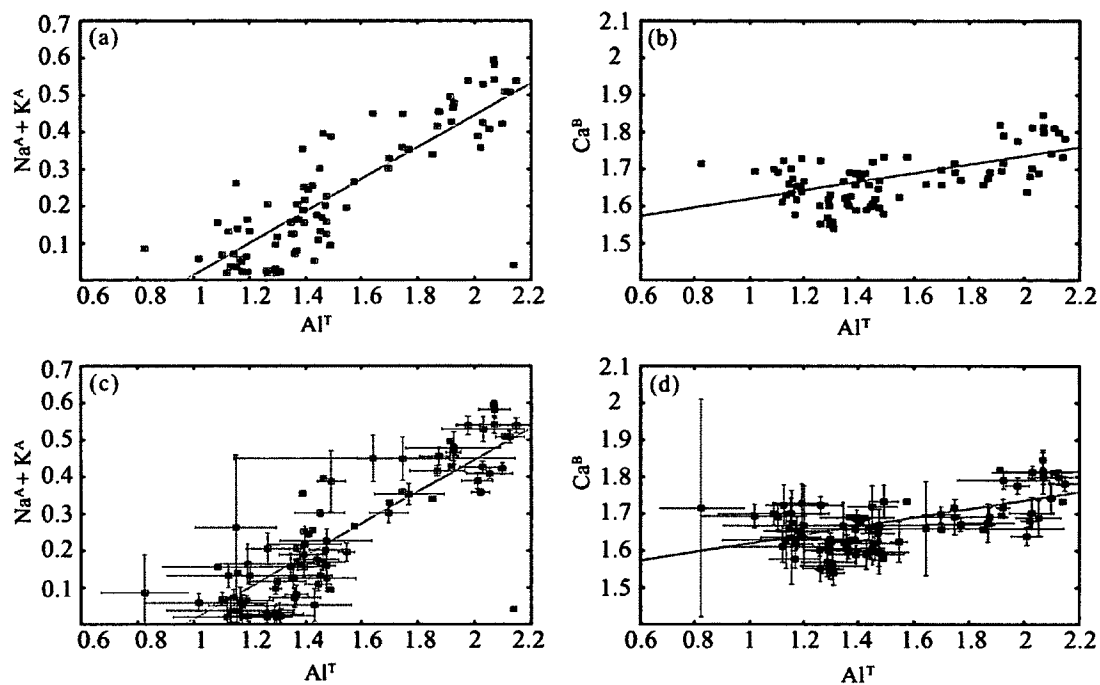


Figure 4.1 Recalculated amphibole cations with and without propagated errors. (A) tetrahedral aluminium (X axis) plotted against A-site alkalis (sodium + potassium; Y axis). (B) tetrahedral aluminium (X axis) plotted against B-site calcium (Y axis). (C, D) contain the same datasets as in (A) and (B), respectively, with the inclusion of error bars as calculated using MINERAL. Dataset taken from author's unpublished data.

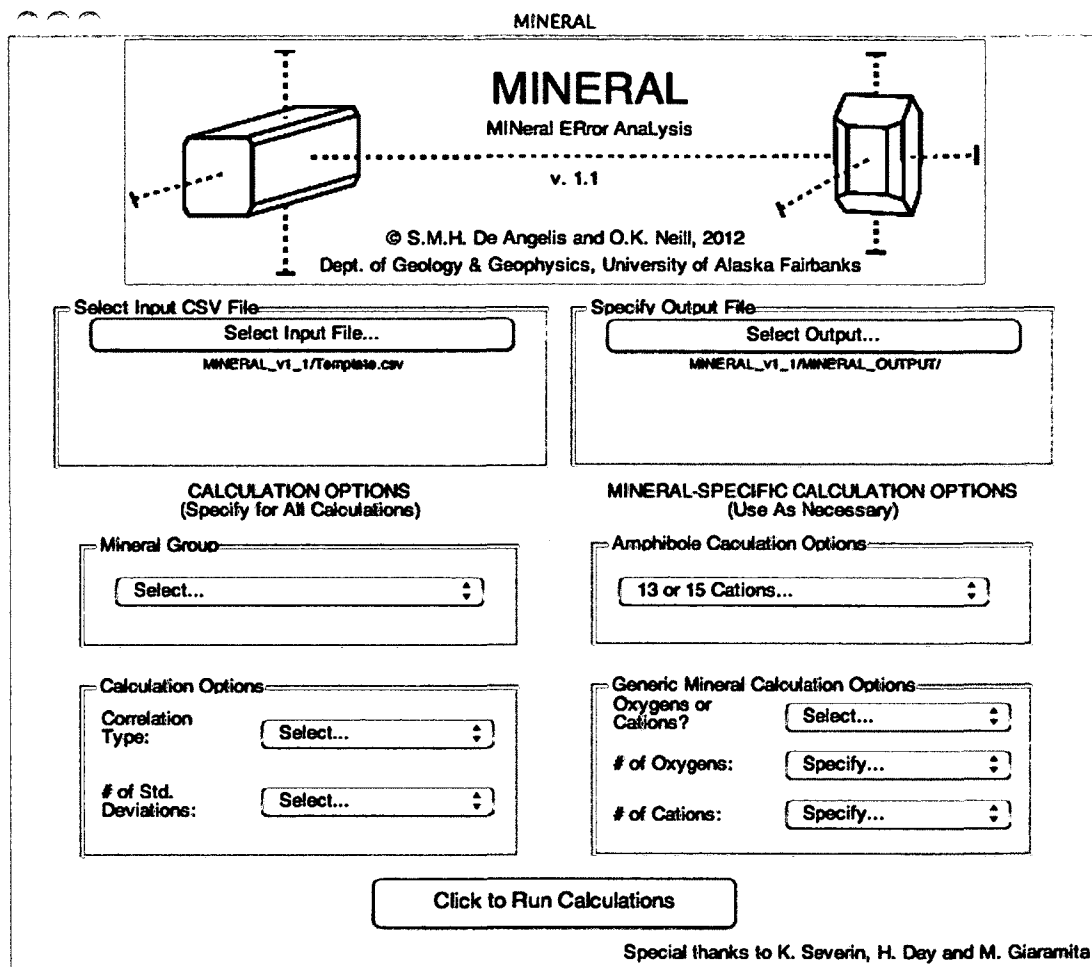


Figure 4.2 Screen shot of the MINERAL GUI. Users are able to define input and output files and select mineral type and calculation options. For amphibole data, users can define the type of recalculation (13 or 15 cations). For generic recalculations (i.e. for minerals not included in the main mineral list) users can choose recalculation based on either cation or oxygen normalization, utilizing any desired number of oxygens and cations per formula unit.

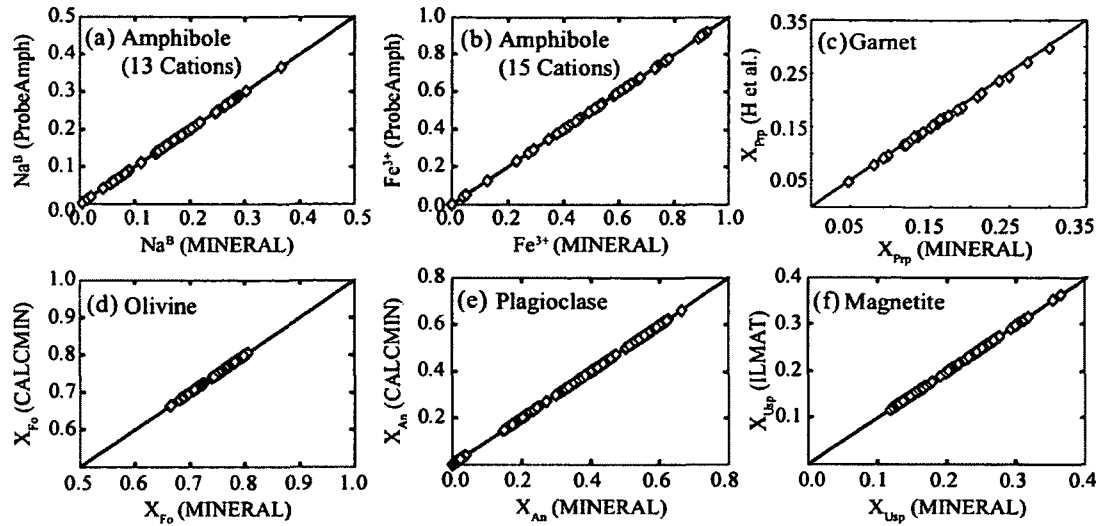


Figure 4.3 MINERAL vs. published recalculations. Amphibole recalculations (a & b) were conducted in both MINERAL and PROBE AMPH (Tindle & Webb, 1994). Garnet (c) recalculations are compared to the results of Harangi et al. (2001). Olivine (d), plagioclase, and plagioclase (e) recalculations were conducted in both MINERAL and CALCMIN (Brandelik, 2009). Magnetite (e) recalculations were conducted in both MINERAL and ILMAT (Lepage, 2003). Datasets taken from: Author's unpublished data; Allialy et al.(2011); Erlund et al. (2010); Harangi et al. (2001); Izbekov et al. (2004); Niedermeier et al. (2009); Robinson et al. (2002); Shamberger and Hammer (2006).

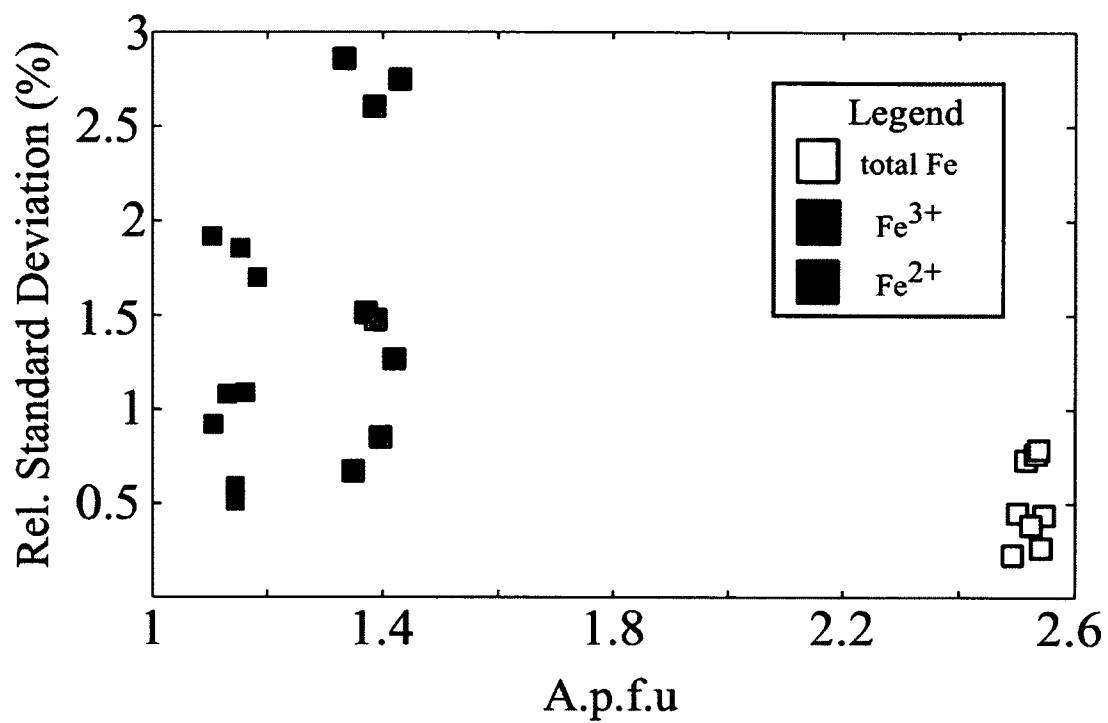


Figure 4.4 Total Fe, Fe³⁺ and Fe²⁺ in magnetite plotted against calculated error. Calculated error reported as relative standard deviation.

4.10 TABLES

Table 4.1: MINERAL uncertainty calculations

	A.p.f.u.	Analytical ^a	Type of uncertainty		
			Average ^b	MINERAL uncorrelated ^c	MINERAL correlated ^d
Plagioclase Feldspar					
Si	2.34	0.019	0.009	0.013	0.009
Al	1.663	0.009	0.009	0.010	0.009
Fe ³⁺	0.02	0.002	0.002	0.002	0.002
Ca	0.67	0.012	0.007	0.011	0.007
Na	0.30	0.009	0.005	0.008	0.005
K	0.010	0.001	0.001	0.001	0.001
Orthopyroxene					
Si	1.96	0.013	0.017	0.014	0.017
Ti	0.004	0.001	0.001	0.001	0.001
Al ^{iv}	0.020	0.001	0.014	0.008	0.012
Al ^{vi}	0.023	0.001	0.007	0.007	0.000
Fe ³⁺	0.039	0.001	0.026	0.024	0.029
Fe ²⁺	0.60	0.010	0.023	0.026	0.025
Mn	0.037	0.003	0.004	0.003	0.004
Mg	1.25	0.022	0.014	0.016	0.014
Ca	0.067	0.003	0.003	0.003	0.003

a. Standard deviation on 'n' analyses of the bench standard

b. Standard deviation on the average a.p.f.u. calculated from 'n' analyses of the sample

c. Standard deviation on the average oxide values from 'n' analyses of the sample, propagated through the formula recalculation using the partial error method in the MINERAL software.

d. Standard deviation on the average oxide values from 'n' analyses of the sample, propagated through the formula recalculation using the full error method in the MINERAL software.

Table 4.2: Comparison to past studies

	Atoms per formula unit				Calculated 1 sigma uncertainty			
	G&D	MINERAL	Ab. Diff	% Diff.	G&D	MINERAL	Ab. Diff	% Diff.
Si ^a	1.8264	1.8265	0.0001	0.01	0.0070	0.0071	0.0001	1.43
Ti ^b	0.0231	0.0230	0.0001	0.43	0.0014	0.0014	0.0000	0.00
Fe ^{3+c}	0.0363	0.0364	0.0001	0.28	0.0145	0.0148	0.0003	2.07
Fe ²⁺	0.1520	0.1518	0.0002	0.13	0.0139	0.0142	0.0003	2.16
Mn ^d	0.0048	0.0046	0.0002	4.17	0.0013	0.0012	0.0001	7.69
Mg ^e	0.9002	0.9006	0.0004	0.04	0.0064	0.0065	0.0001	1.56
Ca ^f	0.6230	0.6231	0.0001	0.02	0.0054	0.0054	0.0000	0.00
Na ^g	0.0848	0.0847	0.0001	0.12	0.0025	0.0028	0.0003	12.0
Cr ⁱ	0.0043	0.0043	0.0000	0.00	0.0015	0.0014	0.0001	6.67

a. 50.16 (0.23); b. 0.84 (0.05); c. 6.18 (0.16); d. 0.15 (0.04); e. 16.59 (0.14); f. 15.97 (0.15); g. 1.2 (0.04); i. 0.15 (0.05)

4.11 REFERENCES

- Agrosi, A. & Schingaro, E. & Pedrazzi, G. & Scandale, E. & Scordari, F. & (2002). A crystal chemical insight into sector zoning of a titanian andradite ('melanite') crystal, *European Journal of Mineralogy* **14**, 785-794.
- Allialy, M. E. & Cherubin, D. S. & Batumike, J. M. & Yacouba, C. & Nicaise, K. A. & Bertin, D. Y. (2011). Chromite, Mg-ilmenite and Priderite as Indicators Minerals of Diamondiferous Cretaceous Kimberlites and Lamproites from Côte d'Ivoire (West Africa), *European Journal of Scientific Research* **48**(4), 665-693.
- Al'meev, R. R. & Ariskin, A. A. & Ozerov, A. Y. & Kononkova, N. N. (2002). Problems of the Stoichiometry and Thermobarometry of Magmatic Amphiboles: An Example of Hornblende from the Andesites of Bezmyannyi Volcano, Eastern Kamchatka, *Geochemistry International* **40** (8), 723-738.
- Andersen, D. J. & Lindsley, D. H. & Davidson, P. M. (1993). QUILF: A pascal program to assess equilibria among Fe-Mg-Mn-Ti oxides, pyroxenes, olivine, and quartz, *Computers and Geosciences* **19**(9), 1333-1350.
- Blundy, J. D. & Holland, J. B. (1990). Calcic amphibole equilibria and a new amphibole-plagioclase geothermobarometer, *Contributions to Mineralogy and Petrology* **104**(2), 208-224.
- Brandelik, A. (2009). CALCMIN – An EXCEL™ Visual Basic application for calculating mineral structural formulae from electron microprobe analyses, *Computers and Geosciences* **35**(7), 1540-1551.
- Carmichael, I. S. E. (1967). The iron-titanium oxides of salic volcanic rocks and their associated ferromagnesian silicates, *Contributions to Mineralogy and Petrology* **14**, 36-64.

Cosca, M. & Essene, E. & Bowman, J. (1991). Complete chemical analyses of metamorphic hornblendes: Implications for normalizations, calculated H₂O activities, and thermobarometry, *Contributions to Mineralogy and Petrology* **108**(4), 472–484.

De Bjerg, S. C. & Mogessie, A. & Bjerg, E. (1992). HYPER-FORM – A Hypercard® program for Macintosh® microcomputers to calculate mineral formulae from electron microprobe and wet chemical analysis, *Computers and Geosciences* **18**, 717-754.

Donovan, J. J. & Kremser, D. & Fournelle, J. H. (2007). ProbeForWindows User's Guide and Reference, Enterprise Edition, Probe Software, Inc., Eugene, OR, 355pp.

Droop, G., (1987). A general equation for estimating Fe³⁺ concentrations in ferromagnesian silicates and oxides from microprobe analyses, using stoichiometric criteria, *Mineralogical Magazine* **51**(361), 431–435.

Erlund, E. J. & Cashman, K.V. & Wallace, P. J. & Pioli, L. & Rosi, M., & Johnson, E. & Delgado Granados, H. (2010), *Compositional evolution of magma from Paricutin Volcano, Mexico: the tephra record. Journal of Volcanology and Geothermal Research* **197**(1-4), 167-187.

Esawi, E. K. (2004). AMPH-CLASS: an Excel spreadsheet for the classification and nomenclature of amphiboles based on the 1997 recommendations of the International Mineralogical Association, *Computers and Geosciences* **30**, 753-760.

Franz, G. & Liebscher, A. (2004). Physical and Chemical Properties of the Epidote Minerals- An Introduction, *Reviews in Mineralogy and Geochemistry* **56**, 1-82.

Giaramita, M. & Day, H. (1990). Error propagation in calculations of structural formulas, *American Mineralogist* **75**, 170-182.

Hahn, G. J. & Shapiro, S. S. (1967). Statistical models in engineering, Wiley, New York, pp. 355.

Harangi, S. & Downes, H. & Kosa, L. & Szabo, C. & Thirlwall, M. F. & Mason, P. R. D. & Matthey, D. P. (2001). Almandine garnet in calc-alkaline volcanic rocks of the Northern Pannonian Basin (Eastern-Central Europe): Geochemistry, Petrogenesis and Geodynamic Implications, *Journal of Petrology* **42**, 1813-1843.

Hawthorne, F. C. & Oberti, R. (2007). Amphiboles: Crystal chemistry, *Reviews in Mineralogy and Geochemistry* **67**, 1-54.

Holland, T. & Blundy, J. (1994). Non-ideal interactions in calcic amphiboles and their bearing on amphibole-plagioclase thermometry, *Contributions to Mineralogy and Petrology* **116**, 433-447.

Izbekov, P. E. & Eichelberger, J. C. & Ivanov B.V. (2004). The 1996 eruption of Karymsky volcano, Kamchatka: Historical record of basaltic replenishment of an andesite reservoir, *Journal of Petrology* **45**(11), 2325–2345.

Leake, B. & Woolley, A. & Arps, C. & Birch, W. & Gilbert, C. & Grice, J. & Hawthorne, F. & Kato, A. & Kisch, H. & Krivovichev, V. & Linthout, K. & Laird, J. & Mandarino, J. & Maresch, W. & Nickel, E. & Rock, N. & Schumacher, J. & Smith, D. & Stephenson, N. & Ungaretti, L. & Whittaker, E. & Youzhi, G. (1997). Nomenclature of amphiboles: Report of the Subcommittee on Amphiboles of the International Mineralogical Association's Commission on New Minerals and Mineral Names, *Canadian Mineralogist* **35**, 219–246.

Lepage, L. (2003). ILMAT: An excel worksheet for ilmenite--magnetite geothermometry and geobarometry, *Computers and Geosciences* **29**(5), 673–678.

Niedermeier, D. R. D. & Putnis, A. & Geisler, T. & Golla-Schindler, U. & Putnis, C. V. (2009). The mechanism of cation and oxygen isotope exchange in alkali feldspars under hydrothermal conditions, *Contributions to Mineralogy and Petrology* **157**(1), 65-76.

Putirka, K. D. & Mikaelian, H. & Ryerson, F. & Shaw, H. (2003). New clinopyroxene-liquid thermobarometers for mafic, evolved, and volatile-bearing lava compositions, with applications to lavas from Tibet and the Snake River Plain, Idaho, *American Mineralogist* **88**, 1542-1554.

Rieder, M. & Cavazzini, G. & D'Yakov, Y. & Frank-Kamenetskii, V. A. & Gottardi, G. & Guggenheim, S. & Koval, P. & Muller, G. & Neiva, A. M. R. & Radoslovich, E. E. & Robert, J. L. & Sassi, F. P. & Takeda, H. & Weiss, Z. & Womes, D. R. (1998). Nomenclature of the micas, *Canadian Mineralogist* **36**.

Robinson, P. T. & Erzinger, J. & Emmermann, R. (2002). The composition and origin of igneous and hydrothermal veins in the lower ocean crust—ODP Hole 735B, Southwest Indian Ridge. In Natland, J.H., Dick, H.J.B., Miller, D.J., Von Herzen, R.P. (Eds.), *Proc. ODP, Sci. Results, 176: College Station, TX (Ocean Drilling Program)*, pp. 1–66.

Robinson, P. & Spear, F. S. & Schumacher, J.C. & Laird, J. & Klein, C. & Evans, B.W. & Doolan, B.L. (1982). Phase Relations of Metamorphic Amphiboles: Natural Occurrence and Theory, In: Veblen, D.R., Ribbe, P.H. (Eds), *Reviews in Mineralogy* **9B**, pp. 1-228.

Schumacher, J. C. (2007). Metamorphic Amphiboles: Composition and Coexistence, In: Rosso, J.J. (Ed), *Reviews in Mineralogy & Geochemistry* **67**, pp. 359-416.

Shamberger, P. J. & Hammer, J. E. (2006). Leucocratic and Gabbroic Xenoliths from Hualalai Volcano, Hawaii, *Journal of Petrology* **47**, 1785-1808.

Sturm, R. (2002). PX-NOM – an interactive spreadsheet program for the computation of pyroxene analyses derived from the electron microprobe, *Computers and Geosciences* **20**, 1201-1228.

Tindle, A.G. & Webb, P.C. (1994). PROBE-AMPH-A spreadsheet program to classify microprobe-derived amphibole analyses, *Computers and Geosciences* **20**(7-8), 1201-1228.

Yavuz, F. & Oztas, T. (1997). BIOTERM- A program for evaluating and plotting microprobe analyses of biotite from barren and mineralized magmatic suites, *Computers and Geosciences* **23**, 897-907.

CONCLUSION

This investigation of natural amphibole geochemistry of the 2006 emplaced magmas (Chapter 1) supports the theory that the high-silica andesite represents a shallow stored magma. Further, results demonstrate that the low-silica andesite also represents a shallow stored magma. These magmas resided in the shallow crust, from at least 1986, and remained chemically distinct as a result of the segregated dike structure of the storage system (e.g., Roman et al., 2006). The experiments investigating mineral stability and compositions provide a significant refinement in the range of possible P_{H_2O} - T conditions for the high-silica andesite (Chapter 2). The early (hot) appearance of quartz and biotite means that the natural phase assemblage occurs only in a restricted area of the phase diagram: above 120 MPa and between ~ 860 and 880°C . Plagioclase An contents indicate storage at pressures of 130–150 MPa and temperatures of ~ 820 – 870°C , whereas glass compositions indicate a range in temperatures from ~ 850 to 860°C (at $P_{H_2O} \sim 130$ – 160 MPa).

The results of this experimental study, presented in Chapter 3, highlights the importance of heating in the formation of natural reaction rims on magmatic amphibole. At least some past studies may have attributed heating-induced reaction rim formation to decompression. With further in-depth data collection on natural amphiboles and with further experimental investigations on different volcanic systems, it may be possible to develop quantitative methods to distinguish between amphibole reaction rim forcing mechanisms. On the basis of current data, tentative conclusions regarding the genesis of Augustine Volcano 2006 amphibole reaction rims can be made. Type 1 reaction rims (those $< 50 \mu\text{m}$ thick) are closest to the textures of experimental decompression reaction rims. However, they contain significant clinopyroxene (in contrast to experimental decompression reaction rims). Therefore, while decompression remains the most likely process driving their formation, it is also possible that some or all represent short duration (< 36 hours) heating. Type 2 reaction rims (50 – $80 \mu\text{m}$ thick) are texturally and mineralogically consistent with heating-induced formation over timescales < 48 hours. Type 3 reaction rims ($> 80 \mu\text{m}$ thick) conform to heating-induced mineralogies. However, average reaction rim thicknesses and microlite sizes exceed those of most heating experiments (although total conversion to pseudomorphs has not occurred as

is seen relatively rapidly in heating experiments). These rims also contain lower crystal number densities than any experimental reaction rims. It is possible that these reaction rims are the result of the slow, long-term decomposition of amphiboles stuck along conduit walls, below amphibole barometric stability, but in a sluggish kinetic environment where reactions occur on a scale of months to years, rather than days to weeks.

This study tested the effects of oxidation on reaction rim formation rates through decompression experiments on a crushed dacite from the 1989/90 eruption of Redoubt Volcano. Attempts to investigate decompression-induced reaction rim formation using Augustine Volcano starting materials were unsuccessful due to the unusually highly silicic melt compositions and crystallinity of Augustine andesites at the experimental conditions required. Instead, a small number of single-step decompression experiments utilizing the Redoubt Volcano dacite starting material employed in the Browne and Gardner (2006) study were conducted. However in this study the fO_2 conditions imposed on the system were increased. Browne and Gardner (2006) buffered experiments at an oxygen fugacity of NNO+1. In contrast, all experiments were buffered at RRO (similar to NNO+2), consistent with the higher oxidation state seen at Augustine Volcano. This approach allowed us to investigate the importance of oxidation conditions of reaction rim formation. Consistent with the results of Browne and Gardner (2006), reaction rim growth rates in this study peak at 65 MPa (~35 MPa below amphibole barometric stability). However, in contrast to the results of Browne and Gardner (2006), growth rates are significantly elevated in experiments buffered at RRO. At final pressures of 65 MPa growth rates are 1.5-4x faster at RRO, while at 55 MPa growth rates are approximately 2x faster at RRO. This reflects the sensitivity of amphibole to changes in magmatic conditions and highlights the individuality of different volcanic systems.

These experimental results show that different combinations of disequilibrium magnitude and experimental durations can create apparently indistinguishable reaction rims. These non-unique solutions mean that it is not possible to use simple parameters to estimate timescales of either heating or decompression in natural samples, unless all other variables are accurately known e.g. heating temperatures or decompression pathway. These results show that for heating-induced reaction rims, crystal nucleation (I) and crystal growth rates (G) provide a possible method for the estimation of heating duration.

Unfortunately there is little systematic change in I or G with magnitudes of heating, and as such distinguishing absolute heating temperatures on the basis of amphibole reaction rims remains an elusive task.

i REFERENCES

Browne, B. L. & Gardner, J. E. (2006). The influence of magma ascent path on the texture, mineralogy, and formation of hornblende reaction rims. *Earth and Planetary Science Letters* **246** (3–4), 161–176.

Cervelli, P., Fournier, T., Freymueller, J., and Power, J., Lisowski, M. & Pauk, B. A. (2010). Geodetic Constraints on Magma Movement and Withdrawal during the 2006 Eruption of Augustine Volcano. In: Power, J. A., Coombs, M. L. & Freymueller, J. T. (eds) *The 2006 eruption of Augustine Volcano, Alaska. USGS Professional Paper* **1769**, 427–452.

Johnson, M. & Rutherford, M. (1989). Experimental calibration of the aluminum-in-hornblende geobarometer with application to Long Valley Caldera (California) volcanic rocks. *Geology* **17**, 837–841.

Johnston, D. (1978). Volatiles, magma mixing, and the mechanism of eruptions at Augustine Volcano, Alaska. Ph.D. Thesis, University of Washington.

Larsen, J., Nye, C., Coombs, M., Tilman, M., Izbekov, P. & Cameron, C. (2010). Petrology and geochemistry of the 2006 eruption of Augustine Volcano. In: Power, J. A., Coombs, M. L. & Freymueller, J. T. (eds) *The 2006 eruption of Augustine Volcano, Alaska. USGS Professional Paper* **1769**, 335–382.

Power, J. A., Coombs, M. L. & Freymueller, J. T. (eds) (2010). *The 2006 eruption of Augustine Volcano, Alaska. USGS Professional Paper* **1769**.

Roman, D. C., Cashman, K. V., Gardner, C. A., Wallace, P. J. & Donovan, J. J. (2006). Storage and interaction of compositionally heterogeneous magmas from the 1986 eruption of Augustine Volcano, Alaska. *Bulletin of Volcanology* **68**(3), 240–254.

Rutherford, M. & Hill, P. (1993). Magma ascent rates from amphibole breakdown: An experimental study applied to the 1980–1986 Mount St. Helens Eruptions. *Journal of Geophysical Research* **98**(B11), 19,667–19,685.

Scaillet, B. & Evans, B. (1999). The 15 June 1991 eruption of Mount Pinatubo. I. Phase equilibria and pre-eruption P-T-fO₂-fH₂O conditions of the dacite magma, *Journal of Petrology* **40**(3), 381–411.

Waitt, R. & Begè, J. (2009). Volcanic Processes and Geology of Augustine Volcano, Alaska. *USGS Professional Paper 1762*, 78 p.

Waythomas, C. F., & Waitt, R. B. (1998). Preliminary volcano-hazard assessment for Augustine Volcano, Alaska. *U.S G S. Open-File Report 98-0106*, 39 p., 1 plate.

Webster, J., Mandeville, C., Goldoff, B., Coombs, M., & Tappen, C. (2010). Augustine Volcano- The influence of volatile components in magmas erupted A.D. 2006 to 2,100 years before present. In: Power, J. A., Coombs, M. L. & Freymueller, J. T. (eds) *The 2006 eruption of Augustine Volcano, Alaska. FUSGS Professional Paper 1769*, 385–423.